STARS

Electronic Theses and Dissertations, 2004-2019

2009

Optical Nonlinear Interactions In Dielectric Nano-suspensions

Ramy El-Ganainy
University of Central Florida

STARS Citation

OPTICAL NONLINEAR INTERACTIONS IN DIELECTRIC NANO-SUSPENSIONS

by

RAMY A.H. EL-GANAINY
B.S. Cairo University, 1999
M.S. Cairo University, 2003
M.S. University of Central Florida, 2007

A dissertation submitted in partial fulfillment of the requirements
for the degree of Doctor of Philosophy
in CREOL, The College of Optics and Photonics
at the University of Central Florida
Orlando, Florida

Fall Term
2009

Major Professor: Demetrios Christodoulides

ABSTRACT

This work is divided into two main parts. In the first part (chapters 2-7) we consider the nonlinear response of nano-particle colloidal systems. Starting from the Nernst-Planck and Smoluchowski equations, we demonstrate that in these arrangements the underlying nonlinearities as well as the nonlinear Rayleigh losses depend exponentially on optical intensity. Two different nonlinear regimes are identified depending on the refractive index contrast of the nanoparticles involved and the interesting prospect of self-induced transparency is demonstrated. Soliton stability is systematically analyzed for both 1D and 2D configurations and their propagation dynamics in the presence of Rayleigh losses is examined.

We also investigate the modulation instability of plane waves and the transverse instabilities of soliton stripe beams propagating in nonlinear nano-suspensions. We show that in these systems, the process of modulational instability depends on the boundary conditions. On the other hand, the transverse instability of soliton stripes can exhibit new features as a result of 1D collapse caused by the exponential nonlinearity.

Many-body effects on the systems' nonlinear response are also examined. Mayer cluster expansions are used in order to investigate particle-particle interactions. We show that the optical nonlinearity of these nano-suspensions can range anywhere from exponential to polynomial depending on the initial concentration and the chemistry of the

electrolyte solution. The consequence of these inter-particle interactions on the soliton dynamics and their stability properties are also studied.

The second part deals with linear and nonlinear properties of optical nano-wires and the coupled mode formalism of parity-time ($\mathcal{PT}$) symmetric waveguides. Dispersion properties of AlGaAs nano-wires are studied and it is shown that the group velocity dispersion in such waveguides can be negative, thus enabling temporal solitons. We have also studied power flow in nano-waveguides and we have shown that under certain conditions, optical pulses propagating in such structures will exhibit power circulations. Finally $\mathcal{PT}$ symmetric waveguides were investigated and a suitable coupled mode theory to describe these systems was developed.

To my parents

ACKNOWLEDGEMENT

I would like to express my gratitude to my parents for their tremendously important role in my educational path. They both insisted from the very beginning that we maintain high level of performance in education. This attitude extended to even later periods of my studies during my undergraduate degree. It is due to their hard work, great support, endless patience, unlimited persistence and sacrifice that I am able to obtain one of the highest scientific degrees. To them I am greatly indebted.

I would like also to thank my adviser Professor Demetrios Christodoulides for everything he taught me. When one reads scientists' biographies, we often come across a special teacher-student relationship where the professor is not just a boss, but a mentor as well. This model of relationship has become very rare nowadays. However, to his credit Professor Christodoulides is one of the very few advisors who still maintain a very close fatherly relation with his students. I learned from him a lot about science and equally important about the ethics of scientific conduct. During the course of my work he was like an older brother to me and he patiently supervised and guided me. In all my scientific projects he kept a very strong and close involvement in all the details, from initiating the idea, developing the theory to even performing the numerical simulations. I am very grateful to everything he taught me.

Special thanks go to Professors Boris Zeldovich and George Stegeman. They both treated me like a son and always found the time and patience to answer all my questions, no matter how simple or trivial they might be.

I would like to mention and thank Professor Jim Moharam who helped me to join CREOL in the first place and thus giving me this wonderful opportunity.

Many thanks to my colleagues Dr. Kostas Makris, Georgios Siviloglou, Dr. Mohamed Salem and Dr. Waleed Solaiman. Dr. Makris taught me all the numerical schemes we use in our research in the field of nonlinear guided waves and from Geogios I learned a great deal about experiments.

Finally I am grateful to all the CREOL staff for their great efforts in helping and supporting me.

TABLE OF CONTENTS

LIST OF FIGURES

LIST OF ABBREVIATIONS

1D	One dimensional
2D	Two dimensional
AlGaAs	Aluminum Gallium Arsenide
MI	Modulational instability
CMT	Coupled mode theory
$\mathcal{PT}$	Parity-Time
FWHM	Full width have maximum
DLVO	Derjaguin, Landau, Verwey , Overbeek
DH	Debye-Hückel
BPM	Beam propagation method
VG	Variational Gaussian
CW	Continuous wave

CHAPTER ONE: INTRODUCTION

Light-matter interactions via radiation forces play nowadays a crucial and central role in several areas of physics, chemistry and biology [1]. One such example is the rich interdisciplinary field of optical traps or tweezers first pioneered by Ashkin and colleagues [2,3]. In these early works the optical self-focusing and four-wave mixing response of colloidal artificial nonlinear systems was also explored in a series of experiments [4-7]. In such settings the optical nonlinearity is a direct outcome of the electromagnetic gradient force and can be relatively high depending on the size and index contrast of the nano-particles involved [8,9]. In general, when an optical beam propagates through a colloidal system, the optical gradient force will attract (or repel) the nano-particles towards (or away from) local intensity maxima. This process, in conjunction with that of Brownian motion, always raises the average refractive index at the beam center [6,7]. Interest in this area was lately rekindled in a number of experimental [10-12] and theoretical [13] investigations. Interestingly, in most studies, the optical nonlinearity of such nano-colloidal suspensions was a priori taken to be of the Kerr type. Yet, as demonstrated in two theoretical studies [14,15], this rather simplistic assumption is only valid when the optical beam intensity is well below a threshold intensity set by the thermal energy. This in turn has important implications on nonlinear beam dynamics in such nano-suspension systems. In fact as demonstrated in [14,15], the nonlinearity of nanosuspensions varies exponentially with intensity. This exponential character of

nonlinearity was also recognized in earlier studies using either thermodynamics arguments [6] or by invoking Chandrasekhar equation [16].

In chapters two and three, we review the origin of the exponential nonlinearity and its consequence on beam dynamics [14]. Starting from first principles, we analyze the nonlinear response as well as the nonlinear Rayleigh losses associated with nano-particle suspensions. This is done by directly solving the underlying Nernst-Planck and Smoluchowski equations under equilibrium conditions. We show that in such systems both the optical nonlinearity and Rayleigh losses vary exponentially with optical intensity. Depending on the sign of the particle polarizability, these exponential nonlinearities can be saturable or super-critical with intensity. The soliton solutions corresponding to these two cases are obtained and analyzed in detail. The stability properties of both 1D and 2D self-trapped states are investigated. Our analysis indicates that at low powers, relatively narrow soliton beams, can propagate undistorted over several diffraction lengths in spite of the presence of nonlinear Rayleigh scattering effects. In the case of negative polarizability particles, a "self-induced transparency" effect is predicted. The propagation characteristics of these self-localized beams are also investigated in nanosuspension mixtures with competing polarizabilities that can exhibit a novel nonlinear response.

Optical beam instabilities in nano-colloidal systems are considered in chapter four. More specifically, we study modulational and transverse modulational instabilities. We show that the process of modulational instability (MI) depends on the boundary conditions, i.e. on the overlap between the exciting beam and the colloidal cell.

Depending on the regime, the MI behavior can display either Kerr or non-Kerr characteristics [17]. Transverse modulation instabilities of soliton stripe beams are also investigated and a new instability is identified as a result of the 1D collapse caused by the exponential nonlinearity.

Chapters five and six deal with the theoretical and experimental aspects of many-body effects on the nonlinear response of stabilized colloids. Starting from a "non-ideal gas" equation of state and by taking into account the screened Coulomb interactions among suspended nano-particles, we show that the nonlinear optical behavior of these colloids can range anywhere from exponential to polynomial depending on their filling factor, composition, and chemistry. The thermodynamics of this problem indicate that while the exponential optical nonlinearity is always present, it can be modified by many-body interactions described by Mayer cluster expansions [18]. This in turn has a profound effect on optical beam dynamics. The stability of optical beams in systems with positive polarizabilities is considered in both 1D and 2D configurations. Experimental measurements presented in chapter six are found to be in good agreement with the theoretical model proposed here. In order to check the validity of our results, numerical schemes based on beam propagation methods were used to predict the nonlinear response of our system. To check the accuracy of such techniques, we use the conservation of power and Hamiltonian. However for the system described in chapters five and six, it is impossible to compute the Hamiltonian. In chapter seven we show how to overcome this obstacle by introducing the concept of the shifted Hamiltonian.

Chapters eight and nine deal with linear and nonlinear properties of optical nano-waveguides. In particular we demonstrate that optical solitons can exist in dispersion-inverted highly-nonlinear *AlGaAs* nanowires. This is accomplished by strongly reversing the dispersion of these nano-structures from normal to anomalous over a broad frequency range. These self-localized waves are possible at very low power levels and can form in millimeter long nanowire structures. The intensity and spectral evolution of solitons propagating in such *AlGaAs* nanowaveguides is investigated in the presence of loss, multiphoton absorption and higher-order dispersion.

In chapter nine we show that energy circulation within a pulse is possible when it propagates in a high-contrast dielectric nanowire. This process is accomplished through electromagnetic "wormhole" regions, in which the Poynting vector associated with the guided mode is negative with respect to the direction of propagation. For demonstration purposes this mechanism is elucidated in *AlGaAs* and silicon nanowaveguides. The effect of dispersion on the power circulation is also considered.

Finally, in chapter ten, we investigate the coupled mode theory (CMT) of parity-time ($\mathcal{PT}$) symmetric waveguide coupler. For this type of structures, it was found that the conventional coupled mode theory fails. Here, starting from the Lagrangian formalism of the problem, we derive the correct CMT. Our results were checked using numerical simulations and excellent agreement with theory is demonstrated.

CHAPTER TWO: OPTICAL NONLINEARITY IN NANO-SUSPENSIONS

In this chapter we analyze the interaction between the electromagnetic field of a laser beam and the nanoparticles involved in a colloidal suspension. To do so we invoke the particle current continuity equation [19],

$$\frac{\partial \rho}{\partial t} + \nabla \cdot \vec{J} = 0 \; , \qquad\qquad (2.1)$$

where ρ represents the particle concentration and $\vec{J}$ is the particle current density. In these systems, the mechanisms contributing to the particle current density are described by the Nernst-Planck equation [19]:

$$\vec{J} = \rho \vec{v} - D\nabla\rho , \qquad\qquad (2.2)$$

where D is the diffusion coefficient and $\vec{v}$ is the particle convective velocity which is related to the external force $\vec{F}$ acting on the nanoparticles through the relation $\vec{v} = \mu\vec{F}$ where μ represents the particle's mobility. The first term on the right hand side of Eq. (2.2) gives the drift current due to the external force while the second one describes the diffusion current due to Brownian motion. In Eqs (2.1)-(2.2) we assume a highly diluted mixture and we neglect any particle-particle interactions. Combining Eqs. (2.1) and (2.2) one obtains the Smoluchowski equation, i.e.,

$$\frac{\partial \rho}{\partial t} + \nabla \cdot \left(\rho \vec{v} - D\nabla\rho\right) = 0 \; . \qquad\qquad (2.3)$$

In order to solve Eqs. (2.1-2.3) we assume steady state conditions, i.e. $\partial / \partial t = 0$. In addition, under equilibrium the current density is zero, $\vec{J} = 0$, i.e. drift is balanced by diffusion. In the case where the particle size is small compared to the wavelength (Rayleigh regime), the average optical gradient force on this nanoparticle can be obtained within the dipole approximation [2,8,9],

$$\vec{F} = \frac{\alpha}{4} \nabla I \quad . \tag{2.4}$$

In Eq. (2.4), α represents the particle polarizability and the quantity $I = \vec{E} \cdot \vec{E}^*$ is associated with the light intensity through the peak spatial field amplitude $\vec{E}$. In the dipole approximation, the polarizability α of a spherical particle having a refractive index n_p is given by [20]:

$$\alpha = 3V_p \, \varepsilon_0 n_b^2 \left(\frac{m^2 - 1}{m^2 + 2} \right) \quad , \tag{2.5}$$

where $V_p = 4\pi a^3 / 3$ is the volume of the particle, ε_0 is the free space permittivity, n_b is the refractive index of the background medium and the dimensionless parameter $m = n_p / n_b$ represents the ratio of the particle's refractive index n_p to n_b. It is important to note that α can be positive or negative depending on whether the refractive index of the particle is higher ($m > 1$) or lower ($m < 1$) than that of the background.

6

In the absence of any illumination (I=0), $\vec{F} = \vec{v} = 0$, the particle density obeys Laplace's equation $\nabla^2 \rho = 0$ under steady state conditions. Moreover, at the container boundaries, the normal component of the diffusion current $\nabla \rho$ is zero. In this case, this Neumann boundary value problem dictates that the particle density is everywhere constant. This uniform distribution is also the one that leads to maximum entropy (in the absence of external constraints).

If on the other hand, light forces are present, substitution of Eq. (2.4) into Eq. (2.2) (under the condition $\vec{J} = 0$) leads to $(\alpha\mu/4)\rho\nabla I - D\nabla\rho = 0$. This last partial differential equation can be directly integrated and gives $\rho = \rho_0 \exp(\frac{\alpha\mu}{4D}I)$. From Einstein's relation $\mu/D = 1/k_B T$ we finally obtain:

$$\rho = \rho_0 \exp\left(\frac{\alpha}{4k_B T}I\right) \quad , \tag{2.6}$$

where $k_B T$ is the thermal energy and ρ_0 stands for the unperturbed uniform particle density (in the absence of light-when the container is large). Given the fact that $\frac{\alpha}{4}I$ is associated with the optical potential energy, this last result is another manifestation of the Boltzmann distribution in statistical physics [1]. Similarly the volume filling factor ($f = \rho V_p$) in nano-suspension systems follows a similar rule, that is $f(I) = f(0)\exp(\alpha I/4k_B T)$. Moreover it is important to emphasize that this exponential law is only applicable in the case of relatively low concentrations (or filling factors) since

the diffusion equation itself ignores particle-particle interactions. As we will see, in most typical cases Rayleigh scattering losses naturally provide an upper bound on particle concentration.

From Eqs. (2.5) and (2.6) we notice that the particle concentration will increase in the regions where the intensity is high, whenever the refractive index of the particles n_p is higher than that of the background n_b ($\alpha > 0$). The converse is true in the other regime ($\alpha < 0$), i.e. the particles will escape from the high intensity regions when their refractive index is lower than that of the surrounding medium. As a result the refractive index is locally perturbed due to this intensity dependent change in the particle concentration. To calculate this local index change we use the Maxwell-Garnett formula given by [21,22]:

$$n_{eff}^2 = n_b^2 \frac{n_p^2 + 2n_b^2 + 2f\left(n_p^2 - n_b^2\right)}{n_p^2 + 2n_b^2 - f\left(n_p^2 - n_b^2\right)} \quad . \tag{2.7}$$

In Eq.(2.7) n_{eff} is the effective refractive index of the medium and f is the volume filling factor given by the ratio of the volume of the particles to the total volume. If we expand the right hand side of Eq. (2.7) and by assuming a relatively small index contrast (i.e. $|m - 1|$ being small) we get:

$$n_{eff}^2 = n_b^2\left(1 + 2f\frac{n_p - n_b}{n_b}\right) \quad . \tag{2.8}$$

In this same limit, Eq.(2.8) reduces to $n_{eff} = (1 - f)n_b + fn_p$. This result could have been intuitively anticipated based on fractional composition arguments. The change in the

refractive index is then given by $\Delta n = n_{eff} - n_b = (n_p - n_b)f$ where the particle volume filling factor is defined as: $f = (\Delta N_p / \Delta V)V_p = \rho V_p$. This together with Eq. (2.6) provides the optical nonlinearity of such nanoparticle suspensions [14,15]:

$$\Delta n_{NL} = n_{eff}(I) - n_{eff}(I=0) = (n_p - n_b)V_p \rho_0 \left(e^{\frac{\alpha}{4k_B T}I} - 1 \right) \quad . \qquad (2.9)$$

In addition to these nonlinear index changes, it is important to incorporate scattering losses in the dynamical evolution equations. If the particle size is smaller than the free-space wavelength λ_0, the scattering cross section can be determined in the Rayleigh regime [23], that is:

$$\sigma = \frac{128\,\pi^5 a^2 n_b^4}{3}\left(\frac{a}{\lambda_0}\right)^4\left(\frac{m^2-1}{m^2+2}\right)^2 \quad , \qquad (2.10)$$

where again a is the particle radius.

We now develop the beam evolution equation in nano-particle suspensions. Starting from the Helmholtz equation $\nabla^2 E + k_0^2 n_{eff}^2 E = 0$, and by assuming a slowly varying field envelope $\varphi(x,y,z)$, that is , $E(x,y,z) = \varphi(x,y,z)\exp(ik_0 n_b z)$, we find that:

$$i\frac{\partial \varphi}{\partial z} + \frac{1}{2k_0 n_b}\nabla_\perp^2 \varphi + k_0(n_p - n_b)f\varphi + i\gamma\varphi = 0 \quad , \qquad (2.11)$$

9

where γ in the last term represents the loss coefficient and $k_0 = 2\pi / \lambda_0$. If we now keep only the loss term in the last equation, we find that $|\varphi|^2 = |\varphi_0|^2 \exp(-2\gamma z)$. Given that $|\varphi|^2 = |\varphi_0|^2 \exp(-\alpha_l z)$ where the loss coefficient is given by $\alpha_l = \sigma\rho$ we finally obtain $2\gamma = \sigma\rho = \sigma\rho_0 \exp(\alpha I / 4k_B T)$. This final expression for the loss coefficient is important since it demonstrates that the scattering losses are actually nonlinear, i.e. they depend on the beam intensity. As will be shown later, these nonlinear Rayleigh losses will play a crucial role in the beam propagation dynamics. From these latter results, Eq. (2.11) takes the form:

$$i \frac{\partial \varphi}{\partial z} + \frac{1}{2k_0 n_b} \nabla_\perp^2 \varphi + k_0 \left(n_p - n_b\right) V_p \rho_0 \; e^{\frac{\alpha}{4k_B T}|\varphi|^2} \varphi + \frac{i}{2}\sigma\rho_0 e^{\frac{\alpha}{4k_B T}|\varphi|^2} \varphi = 0 \; . \quad (2.12)$$

Note that equation (2.12) is general and is applicable in both cases irrespective of whether the polarizability α is positive or negative. If we first consider the case of positive polarizability and by introducing the following normalizations,

$$\xi = z / 2k_0 n_b w^2, X = x / w \;, \; Y = y / w, \; w^{-2} = 2k_0^2 n_b \left|n_p - n_b\right| V_p \rho_0, \varphi = \left(4k_B T / |\alpha|\right)^{1/2} U \;,$$

Eq.(2.12) takes the form:

$$i \frac{\partial U}{\partial \xi} + U_{XX} + U_{YY} + e^{|U|^2} U + i\delta \, e^{|U|^2} U = 0 \quad , \quad (\text{ for } n_p > n_b) \quad . \quad (2.13)$$

10

In Eq.(2.13) U is the normalized field amplitude, w is a characteristic beam width, and the normalized loss δ is given by $\delta = \sigma / \left(2k_0 |n_p - n_b| V_p \right)$. In the same manner, if the polarizability is negative, we obtain

$$ i\frac{\partial u}{\partial \xi} + u_{XX} + u_{YY} - e^{-|u|^2} u + i\delta e^{-|u|^2} u = 0 \quad , \qquad (\text{ for } n_p < n_b) \qquad (2.14) $$

where here we used the symbol u instead of U. If now introduce the transformation $u = Ue^{-i\xi}$ in equation (2.14) we obtain:

$$ i\frac{\partial U}{\partial \xi} + U_{XX} + U_{YY} + \left(1 - e^{-|U|^2} \right) U + i\delta e^{-|U|^2} U = 0 \quad , \qquad (\text{ for } n_p < n_b) . \qquad (2.15) $$

Equations (2.13) and (2.15) are normalized evolution equations describing wave propagation in these two different cases.

Note that in both situations the nonlinearity is of the self-focusing type. In the first case, described by Eq. (2.13), the nonlinearity is monotonically exponential. On the other hand, in the second regime (Eq.(2.15)), the nonlinearity is exponentially saturable. Even though at first sight it might be unclear how both systems lead to a self-focusing nonlinearity, this can be clarified using the following physical arguments. In the case where the particles have a higher refractive index than the background, the polarizability α of each particle is positive and thus the particles are attracted toward the high intensity region, i.e. to the center of the beam, thus elevating the effective refractive index of the system (Fig. 2.1(a)). This will of course increase the nonlinear scattering losses as

well. On the other hand, particles having a lower refractive index than that of the background and hence a negative polarizability will be repelled away from the center of the beam, again raising the refractive index at the center (Fig. 2.1(b)). In this latter case however, the nonlinear losses decrease at the beam center (due to the reduction in the particle concentration), thus increasing the transparency of the system. As it will be shown, this difference in the character of the exponential optical nonlinearity will have a profound effect on the beam dynamics of spatial solitons.
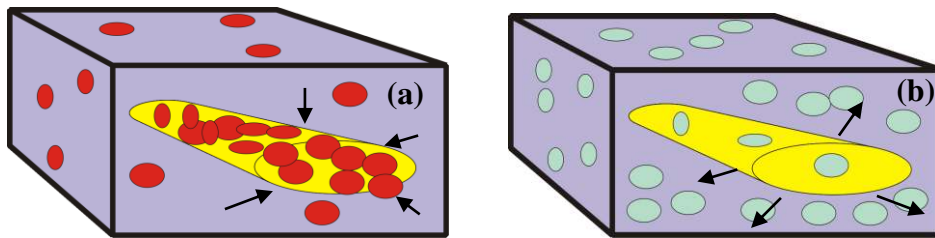
Figure 2.1.1 A high intensity beam (a) attracting nanoparticles with positive polarizabilities and (b) repelling nanoparticles with negative polarizabilities.

CHAPTER THREE: SOLITON DYNAMICS AND STABILITY PROPERTIES

In this chapter we investigate the dynamics and stability properties of the soliton solutions possible in exponentially nonlinear nano-suspensions. To do so, we solve Eqs. (2.13) and (2.15) in both one and two dimensional configurations in the absence of any nonlinear Rayleigh losses ($\delta = 0$).

3.1. 1D soliton solutions

We first consider the 1D case. Here we seek 1D stationary solutions of the form $U(X, \xi) = g(X) \exp(i\kappa\xi)$ where κ represents the soliton eigenvalue. Substituting this latter expression into Eqs. (2.13) and (2.15) gives:

$$g_{XX} - \kappa\, g + e^{g^2} g = 0 \quad , \tag{3.1-a}$$

$$g_{XX} - \kappa\, g + \left(1 - e^{-g^2}\right) g = 0 \tag{3.1-b}$$

Equations (3.1) can be readily integrated once, thus leading to:

$$g_X^2 - \kappa g^2 + e^{g^2} = C_1 \tag{3.2-a}$$

$$g_X^2 + (1 - \kappa) g^2 + e^{-g^2} = C_2 \tag{3.2-b}$$

Since asymptotically, these solutions satisfy $g|_{X \to \infty} = 0$ and $g_X|_{X \to \infty} = 0$, we set $C_1 = C_2 = 1$. By rearranging Eqs.(3.2) we directly obtain:

$$\int_{g_0}^{g} \frac{dg'}{\sqrt{1 + \kappa g'^2 - \exp(g'^2)}} = \pm \int_0^X dX' \qquad (3.3\text{-a})$$

$$\int_{g_0}^{g} \frac{dg'}{\sqrt{1 + (\kappa - 1)g'^2 - \exp(-g'^2)}} = \pm \int_0^X dX' \qquad . \qquad (3.3\text{-b})$$

As Eqs. (3.3) imply, these soliton solutions are symmetric with respect to the origin $X = 0$. Using the boundary conditions at the beam center, namely that $g(0) = g_0$ and $g_X(0) = 0$ we can now numerically integrate Eqs. (3.3).

We will first discuss the 1D soliton solutions associated with exponential nonlinearities, i.e., Eq. (3.3-a). Figure 3.1(a) shows the existence curve of these solutions, e.g. their normalized intensity FWHM as a function of their peak intensities. The inset in Fig. 3.1(a) shows the intensity profile of such a solution at $\kappa = 3$. As one can see, the beam width monotonically decreases as the soliton peak intensity increases. The stability properties of this class of solutions can be systematically examined using the power-eigenvalue ($P - \kappa$) diagram where $P = \int |U|^2 dX$. Following Vakhitov and Kolokolov [24], this solution is stable whenever the slope of the curve is positive (for $\kappa < 2.49$) and is unstable for higher eigenvalues where the slope is negative as shown in Fig. 3.1(b).

The existence of two different regions of stability is by itself an interesting result given that we are dealing with a 1D system [25]. In reality, above this threshold

14

($\kappa = 2.49$) these 1D solutions tend to catastrophically collapse into a singularity. This behavior can be qualitatively explained based on the Taylor series expansion $e^{|U|^2} = 1 + |U|^2 + (1/2)|U|^4 + \ldots$. As a result, at lower intensities the nonlinearity is of the Kerr-type and the corresponding solutions are stable.
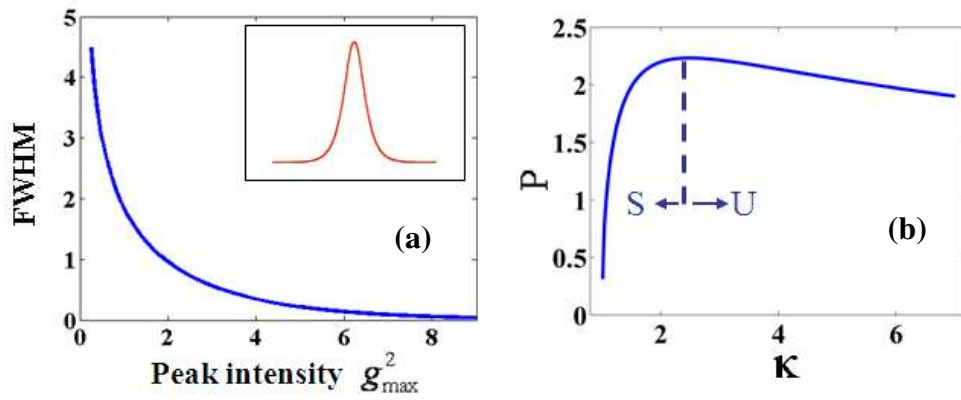
Figure 3.1 Normalized soliton FWHM width as a function of their normalized peak intensities in exponential nonlinear nanosuspentions. The inset represents the intensity profile of such a solution. (b) The corresponding $P - \kappa$ diagram with S being the stable and U the unstable branch.

However, at higher intensities, the degree of nonlinearity is above the supercritical value (i.e. $|U|^4$) necessary for 1D systems to exhibit collapse [25]. Of course in reality nonlinear Rayleigh scattering and/or saturation effects in the particle concentration may prevent such a collapse from occurring. The dynamics of these solutions are then studied by directly solving Eq. (2.13) and by including nonlinear Rayleigh scattering losses. To

illustrate our results we consider the propagation of a soliton beam in nano-suspensions when the wavelength is $0.532\,\mu m$. The nano-suspensions involve polystyrene nano-particles (refractive index $n_p = 1.56$) of radius 50 nm suspended in water ($n_b = 1.33$) at a concentration of $7 \times 10^{11}\,cm^{-3}$ (or $f = 3.5 \times 10^{-4}$). Under linear conditions, a 10 micron beam (FWHM in width) expands considerably because of diffraction (3 times) and loses 13% of its power because of scattering losses. Conversely, in the nonlinear regime, this same beam can propagate up to 4 diffraction lengths (2 mm) without any appreciable distortion-limited only by the nonlinear losses (20%), as clearly shown in Fig. 3.2.
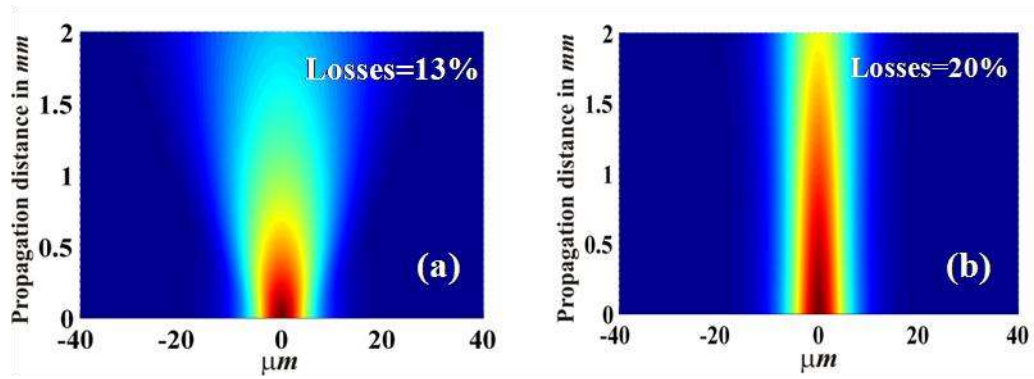
Figure 3.2 Linear propagation of an optical beam in water-polystyrene nanosuspension. (b) Nonlinear soliton effects in this same system.

On the other hand, the situation for the saturable nonlinearity (described by Eqs. (2.15) and (3.3-b)) is quite different. Figure 3.3(a) shows the soliton existence curve for this latter system. These results indicate that the intensity FWHM width of these solutions tend to initially contract with peak intensity and eventually expand −a characteristic behavior of solitons in saturable systems [26,27]. The inset in Fig. 3.3(a) shows the

intensity profile of such a solution at $\kappa = 0.95$. The power-eigenvalue $P - \kappa$ diagram in this regime is shown in Fig. 3.3(b). This graph indicates that in the saturable case (of negative polarizabilities) the 1D soliton solutions are always stable since $dP/d\kappa > 0$.
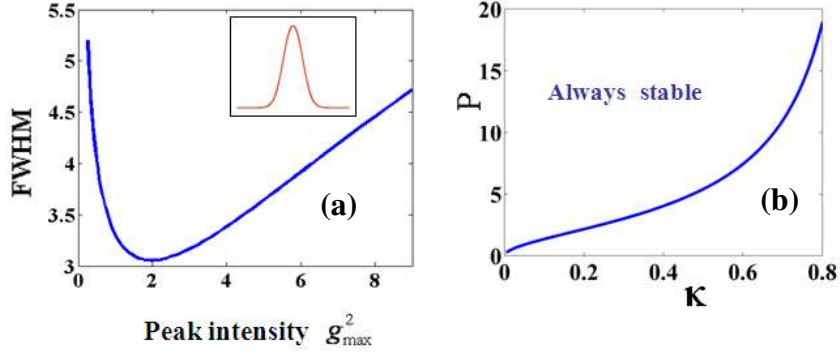
Figure 3.3 (a) Normalized soliton intensity FWHM width as a function of their peak intensity in exponentially saturable nanosuspentions. The inset depicts such a solution (b) Corresponding $P - \kappa$ diagram indicating stability.

Figure 3.4 depicts the propagation of a 10 micron beam (FWHM in width) in a suspension involving 50 nm air nano-bubbles ($n_p = 1$) floating in water ($n_b = 1.33$). Again the wavelength is taken to be $0.532\,\mu m$. The nano-bubble concentration is assumed to be $2 \times 10^{12}\ cm^{-3}$ or $f = 10^{-3}$. Under linear or low power conditions, the beam diffracts considerably (more than 10 times) and loses almost all its energy (97%) as clearly indicated in Fig. 3.4(a).

This considerable loss is a direct outcome of Rayleigh scattering at these concentration numbers. At power levels sufficient to sustain a soliton however, the beam expels the nano-spheres from the center, thus giving rise to *self-induced transparency* and

self-trapping effects. In other words, at high powers the beam can effectively reduce the "haze" while at the same time can establish its own waveguide structure In this case the overall losses drop from 97% to 20%.
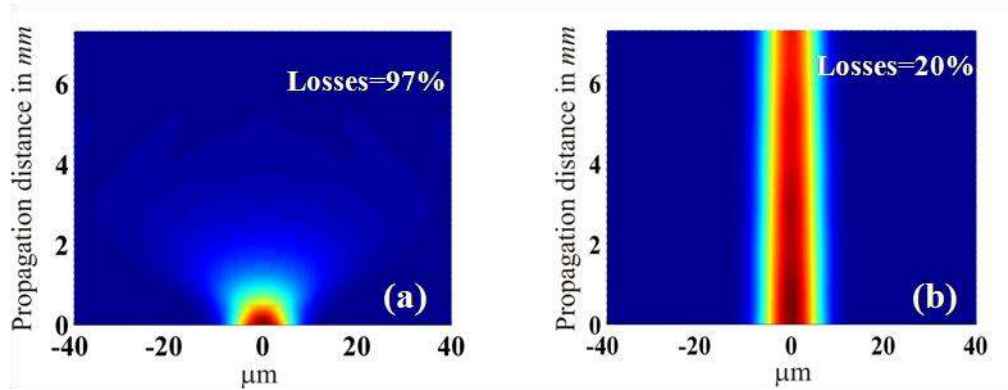
Figure 3.4 Linear propagation of a 10 μm beam in water-air nanobubble suspenstions where 97% of losses are expected. (b) Nonlinear soliton self-trapping and self-induced transparency effects.

A direct simulation of this beam (based on Eq. (2.15)) shows that the soliton (10 micron FWHM) can propagate up to 12 diffraction lengths (Fig. 3.4(b)), i.e. approximately 4 times more than in the first case. This behavior is understood by recalling that the nonlinear losses are exponentially growing in the first case whereas are exponentially decaying in the second one.

3.2. 2D soliton solutions

Two-dimensional soliton solutions in these systems are obtained by directly solving the 2D version of Eqs.(2.13) and(2.15). To do so we seek stationary solutions in cylindrical

coordinates having the form $U(r,\xi) = g(r)\exp(i\kappa\xi)$ and we keep in mind the boundary

conditions $g = 0$ at $r \to \infty$ and $dg/dr = 0$ at $r = 0$.

We begin by considering first nanoparticles with positive polarizabilities. In this

regime, the normalized $(P - \kappa)$ diagram associated with these solutions is shown in Fig.

3.5(a). The monotonically decreasing behavior of this latter curve clearly indicates that

the 2D soliton solutions in exponentially nonlinear nanosuspensions are always unstable

and tend to catastrophically collapse. Again as in the 1D case, collapse will be prevented

because of nonlinear Rayleigh scattering and/or saturation effects in the particle

concentration. In addition, the intensity profiles of this class of waves exhibit a cusp-like

shape as a result of the exponential nonlinearity, as shown in Fig. 3.5(b). As an example

we study the propagation of a 10 micron width (FWHM) 2D beam in water containing

polystyrene nanospheres. All the physical parameters are the same as those used in the

corresponding 1D system except for the volume filling factor which taken here to be

$f = 10^{-4}$. At low power levels the beam expands because of diffraction (2 times) and

loses 2% of its power as a result of Rayleigh scattering, as shown in Fig. 3.5(c). On the

other hand, at 5W (at soliton power), this same beam can propagate up to $1mm$ (3.5

diffraction lengths) without any appreciable expansion and in spite of the nonlinear

Rayleigh losses (5%) as accounted in Eq.(2.13), as demonstrated in Fig. 3.5(d). We note

that in our simulations this beam would have otherwise undergone a collapse had not

been for Rayleigh scattering. This collapse behavior is illustrated in Fig. 3.5(e) in the

absence of nonlinear losses and by neglecting saturation effects in the particle density.
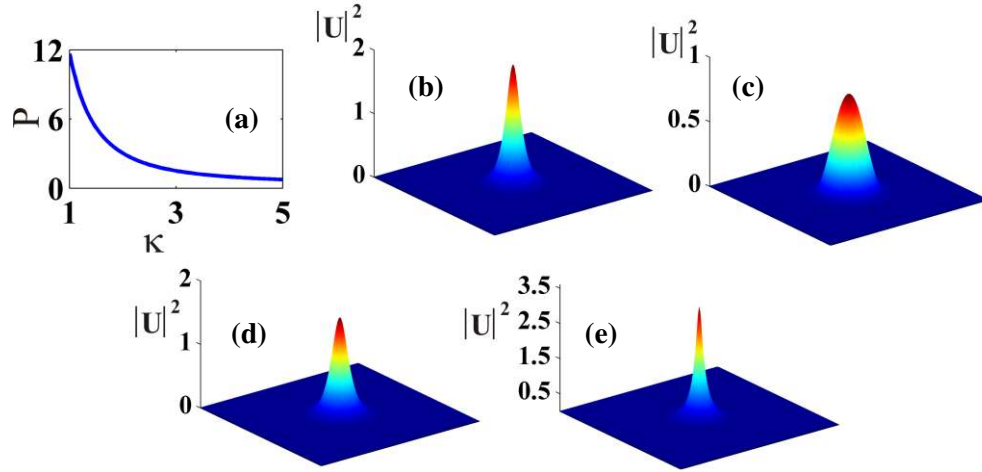
Figure 3.5 (a) $P - \kappa$ stability diagram of 2D solitons in nanosuspentions with positive polarizabilities. (b) Soliton intensity profile at $\kappa = 1.7$. (c) Beam diffraction at low power levels shown in scale. (d) Propagation dynamics of a 2D 10 μm soliton beam after 1 mm in the presence of Rayleigh losses. (e) Catastrophic collapse in the absence of nonlinear losses.

We now consider 2D soliton solutions in nanosuspensions with negative polarizabilities exhibiting saturable exponential nonlinearities similar to those encountered in plasma science [28,29]. This is done by considering Eq. (2.15) in the absence of losses. The ($P - \kappa$) stability diagram associated with these solutions is shown in Fig. 3.6(a) and indicates that these self-trapped states are always stable since $dP/d\kappa > 0$.

To illustrate our results we consider air nano-bubble suspensions in water. Again all the physical parameters used here are the same as those used in the corresponding 1D example and $f = 10^{-3}$. Fig. 3.6(b) shows the intensity profile of a 10 μm beam (FWHM)

that is possible in this system at a power level of 2.8 Watts. At very low intensities, after

3.5 *mm* of propagation, the beam linearly diffracts (7 times) and loses 80% of its power

because of substantial Rayleigh scattering, Fig. 3.6(c).

$\times 10^3$
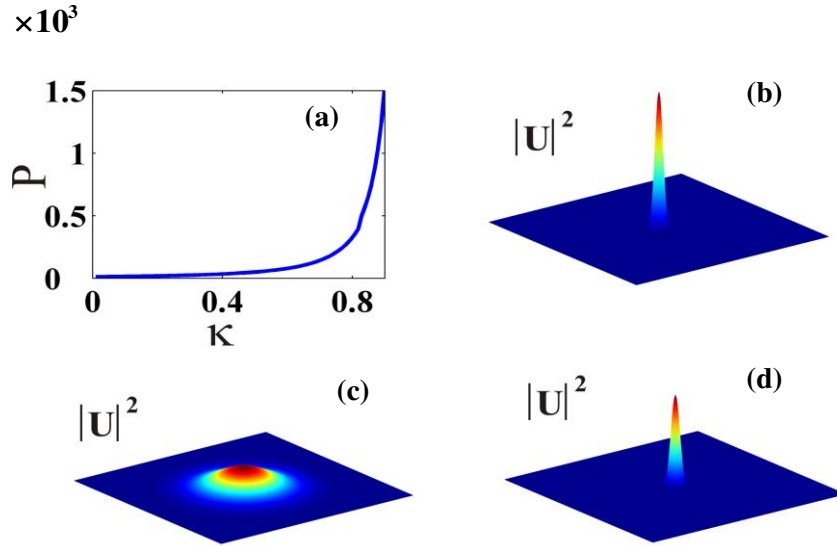
Figure 3.6 (a) $P - \kappa$ stability diagram of 2D solitons in nano-suspensions with negative

polarizabilities. (b) Soliton intensity profile at $\kappa = 0.5$. (c) Expansion and loss effects

during linear propagation of a 2D 10 μm beam after 3.5 *mm* (d) Self-trapping and self-

induced transparency effects at 6 W of beam power in this same system.

On the other hand, when the beam input power is 6 W, the beam self-traps and at

the same time increases the transparency of the system by optically expelling the

nanoparticles from its center. In this latter case, the beam expands only by 10% and loses

a small fraction of energy (20%) after 3.5 *mm* of propagation as shown in Fig. 3.6(d). As

in the 1D case, this self-induced transparency effect is again a result of the specific nature

of the optical gradient force.

3.3. Engineering nonlinearities in nano-suspension systems

So far we have considered nano-suspensions involving only one type or species of nano-particles. In this section we study the effect of mixing two or more types of nano-particles in the same suspension. In this case the Nernst-Planck equation takes the form:

$$\vec{J} = \sum_j \vec{J}_j = \sum_j \left(\rho_j \vec{v}_j - D_j \nabla \rho_j \right) \quad , \tag{3.4}$$

where the subscript j runs over all different kinds of nano-particles. In the case of diluted suspensions particle-particle interactions can be neglected. As a result each current component $\vec{J}_j$ vanishes independently and the statistical distribution for each type of nano-particles is represented by a Boltzmann distribution, i.e.

$$\rho_j = \rho_{j0} \exp\left(\frac{\alpha_j}{4 k_B T} I \right) \quad . \tag{3.5}$$

Following an analysis similar to that of chapter 2, we find that the beam evolution equation in such a system is given by:

$$i \frac{\partial U}{\partial \xi} + U_{XX} + U_{YY} + \sum_{j=1,2,3,\dots} \left[\frac{\left(n_{pj}^+ - n_b \right) V_j^+ \rho_{jo}^+}{\left(n_{p1}^+ - n_b \right) V_1^+ \rho_{1o}^+} e^{\frac{\alpha_j^+}{\alpha_1^+}|U|^2} U + \frac{\left(n_b - n_{pj}^- \right) V_j^- \rho_{jo}^-}{\left(n_{p1}^+ - n_b \right) V_1^+ \rho_{1o}^+} \left(1 - e^{-\frac{|\alpha_j^-|}{\alpha_1^+}|U|^2} \right) U \right]$$

$$+ \sum_{j=1,2,3,\dots} i \left(\frac{\delta_j^+}{\delta_1^+} e^{\frac{\alpha_j^+}{\alpha_1^+}|U|^2} + \frac{\delta_j^-}{\delta_1^+} e^{-\frac{|\alpha_j^-|}{\alpha_1^+}|U|^2} \right) U = 0 \quad . \tag{3.6}$$

In Eq. (3.6), we have incorporated nonlinear contributions from either type of particles, i.e. from those with positive or negative polarizabilities (the +/- superscript denotes particles with positive/negative polarizabilities). The last term in Eq.(3.6) represents Rayleigh losses due to these two different kinds of nano-particles. For each family, the equation implicitly assumes different values for their respective polarizabilities and densities. Note that in Eq.(3.6) the coefficient of each term is a function of the nano-particle properties (refractive index, radius) and their concentrations. Thus by controlling these parameters one could design an otherwise physically nonexistent nonlinear response. For example if we consider a mixture of only two different types of particles having equal but opposite polarizabilities and we choose the particle concentrations so as the nonlinear coefficients in both terms of Eq.(3.6) are equal to unity, then the nonlinear evolution equation (neglecting the loss terms) can take the form:

$$i\frac{\partial U}{\partial \xi} + U_{XX} + U_{YY} + 2\sinh\left(|U|^2\right)U = 0 \qquad . \qquad\qquad (3.7)$$

This suggests that systems with artificial nonlinearities (such as that of Eq.(3.7) with hyperbolic-sine nonlinearity) can be for example synthesized at will through appropriate inclusion of nanoparticles.

CHAPTER FOUR: MODULATIONAL AND TRANSVERSE MODULATIONAL INSTABILITIES

Optical beam instabilities in nano-colloidal systems are the subject of this chapter. In particular, we focus our attention on modulational and transverse modulational instabilities. We show that the process of modulational instability (MI) depends on the boundary conditions, i.e. on the relative size of the exciting beam with respect to that of the colloidal cell. Depending on the regime, the MI behavior can display either Kerr or non-Kerr characteristics. Transverse modulation instabilities of soliton stripe beams are also investigated and a new instability is identified as a result of the 1D collapse caused by the exponential nonlinearity. In both cases, linear stability analysis is carried out in the absence of any nonlinear Rayleigh losses. This analysis is then compared against beam propagation simulations that also incorporate Rayleigh losses.

4.1. Modulational instability

Modulational instability is a process during which small perturbations superimposed on top of a plane wave propagating in a nonlinear medium can grow and eventually cause the plane wave to break into several small filaments. To study this phenomenon and determine the conditions under which this effect will occur, we apply linear stability analysis and assume sinusoidal perturbations of certain spatial frequencies. The growth rate of the perturbations as a function of their spatial frequencies is then obtained.

We start our analysis by writing the evolution equation for an optical beam propagating in a nano-particle colloidal system in the absence of nonlinear Rayleigh losses:

$$i\frac{\partial \varphi}{\partial z} + \frac{1}{2k_0 n_b}\nabla_{\perp}^2 \varphi + k_0\left(n_p - n_b\right)V_p \rho_0 \, \exp\left(\frac{\alpha}{4k_B T}\left(|\varphi|^2 - |\varphi_0|^2\right)\right)\varphi = 0 \quad . \quad (4.1)$$

This equation is exactly the same as Eq.(2.12) except that the loss term is omitted and φ_0 represents a possible infinite light background or a plane wave component (if it exists) upon which the beam rests. This last term arises as an integration constant in the solution of the Nernst-Planck equation and guarantees that the particle density is constant under plane-wave illumination, as one may expect from the gradient nature of the optical force [8,9]. In normalized units, Eq. (4.1) takes the form [17]:

$$i\frac{\partial u}{\partial \xi} + u_{XX} + u_{YY} + a\exp\left[a\left(|u|^2 - b|u_o|^2\right)\right] u = 0 \qquad (4.2)$$

where again $\varphi = \left(4k_B T/|\alpha|\right)^{1/2} u$, $\xi = z/2k_0 n_b w^2$, $X = x/w$, $Y = y/w$, and the spatial scale w is given by $w^{-2} = 2k_0^2 n_b |n_p - n_b| V_p \rho_0$. Equation (4.2) was written in a general form so as to account for different scenarios. The case $a = +1$ corresponds to a system with an index contrast m greater than unity $\left(m = n_p/n_b > 1\right)$ while $a = -1$ is used for $m < 1$. The constant b is either 1 or 0 depending on whether the input is a plane wave (or rests on a plane wave) that covers the entire cell or a quasi plane-wave broad beam that covers only a small portion of the cell, respectively. In other words, even though the nonlinearity is local, the boundary conditions manifest themselves in a non-local way.

Here we consider the process of modulation instability. To do so we write the plane wave solution of Eq.(4.2) as : $u = u_o \exp(i\mu_p \xi)$ where $\mu_p = a \exp\left(a(1-b)u_o^2\right)$. By introducing a small perturbation $\varepsilon(X,\xi)$ in this solution $u = \left(u_o + \varepsilon(X,\xi)\right)\exp(i\mu_p \xi)$ and by substituting this latter form back in Eq.(4.2), then to first order in ε we get:

$$i\varepsilon_\xi + \varepsilon_{XX} + u_o^2\left(\varepsilon + \varepsilon^*\right)\exp\left(a(1-b)u_o^2\right) = 0 \qquad . \qquad (4.3)$$

Assuming a solution of the form: $\varepsilon = A\cos(\beta\xi - KX) + iB\sin(\beta\xi - KX)$, and by eliminating the arbitrary constants A,B we obtain:

$$\beta^2 = K^2\left[K^2 - 2u_o^2 \exp\left(a(1-b)u_o^2\right)\right] \qquad . \qquad (4.4)$$

From this last relation we see that under plane wave excitation conditions ($b=1$) the MI of this system exhibits a Kerr response [30,31] regardless of the refractive index contrast. On the other hand, for the more realistic case of a quasi-plane wave input, when the beam is wide enough to avoid appreciable diffraction but does not cover the entire cell ($b=0$), the situation is different. In this latter case, when the particle polarizability is positive $(m>1)$, Eq.(4.4) becomes $\beta^2 = K^2\left(K^2 - 2u_o^2 e^{u_o^2}\right)$. Here, as in the case of Kerr nonlinearities, the maximum gain happens to be at the peak intensity of the beam ($u_{o\max}$) and the spatial frequency at which this maximum gain is attained occurs at $K^2 = u_o^2 \exp(u_o^2)$. Fig.4.1(a) shows the gain curve for a system of polystyrene nano-particles ($n_p = 1.56$) of radius (r=50 nm) suspended in water when the particle concentration $7 \times 10^{17}\ m^{-3}$. For this set of parameters, the power density of the incident

plane wave is 1 MW/cm^2. Conversely, when the particle polarizability is negative $(m<1)$, the modulation instability exhibits entirely different characteristics as the dispersion relation takes the form $\beta^2 = K^2\left(K^2 - 2u_o^2 e^{-u_o^2}\right)$. In this case, in contrast to the previous one, the maximum gain does not monotonically increase with the peak intensity u_o. In fact the maximum intensity occurs when $u_o = 1$ and for a spatial frequency $K = 1/e$. The gain curve in Fig.4.1(b) was obtained for air nano-bubbles ($n_p = 1$) and radius of 50 nm suspended in water at a concentration of $2 \times 10^{18}\ m^{-3}$ (the power density is 0.7 MW/cm^2). In all the examples considered in this study the wavelength is taken to be $\lambda_0 = 0.532 \mu m$.
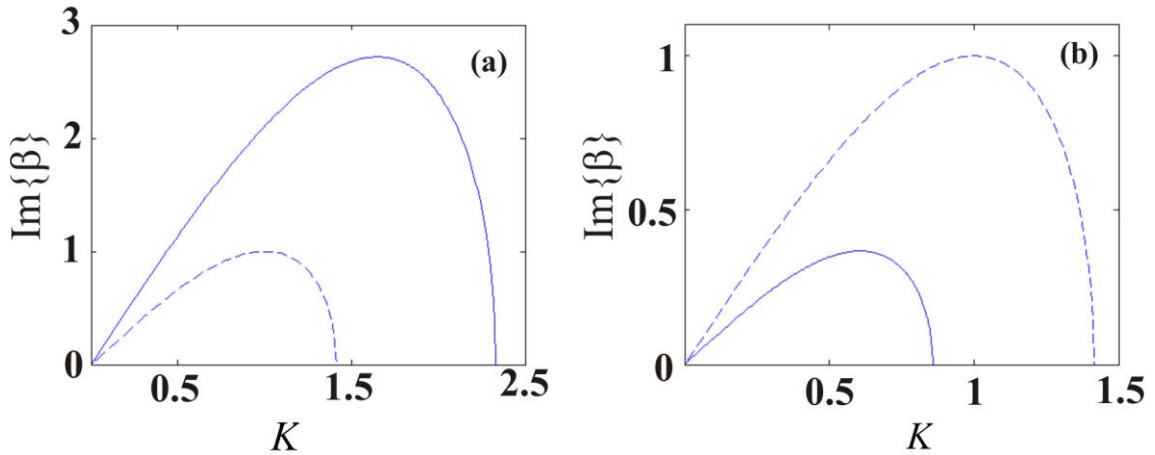
Figure 4.1 MI gain versus perturbation wavenumber for (a) an exponentially nonlinear ($n_p/n_b > 1$) and (b) an exponentially saturable nonlinear nanosuspension system ($n_p/n_b < 1$) for the parameters given in the text. The solid/dotted curves depict the MI gain when $b = 0/b = 1$ for $u_o = 1$.

4.2. Transverse modulational instability

Next we study transverse modulational instabilities. This process is responsible for breaking up a soliton solution into several filaments. In other words, here we are concerned with the effect of small perturbations superimposed on nonlinear localized eigenmodes instead of plane waves. As in the case of MI, we use linear stability analysis and determine the perturbation growth rate for each spatial frequency.

To do so, we consider the transverse modulation instability of soliton stripes (along y) [32]. In this case we assume a solution of the form $u = \left(u_s(X) + \varepsilon(X,Y,\xi)\right)\exp(i\kappa\xi)$ where $u_s(X)$ is a 1D soliton solution of Eq.(4.2), $\varepsilon(X,Y,\xi)$ is a small perturbation and κ is the soliton eigenvalue. Substituting this form in Eq.(4.2) and by retaining only first-order terms in ε we get:

$$i\varepsilon_\xi - \kappa\varepsilon + \varepsilon_{XX} + \varepsilon_{YY} + a\exp(au_s^2)\varepsilon + u_s^2\exp(au_s^2)\left(\varepsilon + \varepsilon^*\right) = 0 \quad . \qquad (4.5)$$

If we in turn assume

$$\varepsilon(X,Y,Z) = \left(V(X) + W(X)\right)\exp\left[i(\beta\xi + qY)\right] + \left(V^*(X) - W^*(X)\right)\exp\left[-i\left(\beta^*\xi + qY\right)\right]$$

$$(4.6)$$

then from Eq.(4.5) we obtain the following linear coupled eigenvalue equations:

$$V_{XX} + [a\exp(au_s^2) + 2u_s^2\exp(au_s^2) - \kappa - q^2]V = \beta W \qquad (4.7\text{-a})$$

$$W_{XX} + [a\exp(au_s^2) - \kappa - q^2]W = \beta V \qquad . \qquad (4.7\text{-b})$$

For any specific power level (corresponding to a certain soliton solution u_s), the above generalized eigenvalue problem can be solved for each transverse spatial frequency q.

The solution $u_s(X)$ is stable against transverse modulation perturbations when β is real and it becomes unstable in the complex β domain.

We first consider the case when the particle's refractive index is higher than that of the background, i.e. when $a = 1$. In this case, as discussed in chapter 3, the soliton solution has two regimes of stability with respect to longitudinal perturbations (along x) of the form $\varepsilon(X,\xi)$ (Vakhitov-Kolokolov criterion) [14]. The transverse instability $\beta - q$ gain curve corresponding to a 1D soliton that belongs to the stable region [14] ($\kappa < 2.49$), is shown in Fig.4.2(a) where again polystyrene spheres of radius r=50 nm are assumed to be suspended in water at a concentration of $7 \times 10^{17}\ m^{-3}$. This gain curve was obtained for a soliton solution of Eq.(4.2) at a power density of 1.3 kW/cm and at $\kappa = 1.7$. From Fig. 4.2(a) one can see that the solution is marginally stable at q=0, unstable for long wavelength perturbations and becomes stable for q>1.9. This behavior qualitatively resembles that encountered in nonlinear Kerr systems [32]. Contrary to this latter case, in the longitudinally unstable region ($\kappa > 2.49$), the transverse instability displays new features due to the competition between longitudinal and transverse instabilities. Fig.4.2(b) shows the gain curve for a soliton stripe at power density of 1.33 kW/cm and for $\kappa = 3$, i.e. when it belongs to the unstable branch of the power-eigenvalue diagram discussed before in chapter 3 (see ref. [14]).
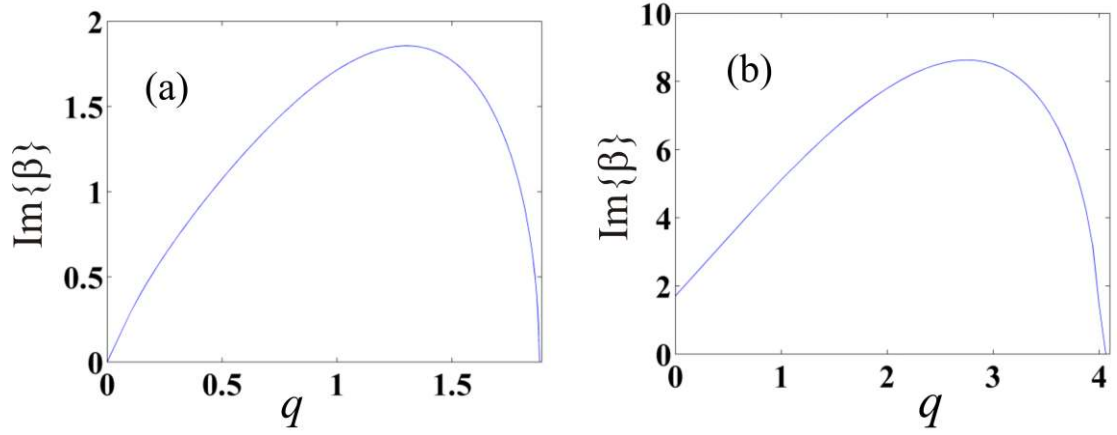
Figure 4.2 Transverse modulational instability gain of a stripe soliton versus perturbation wavenumber q for an exponentially nonlinear colloidal system when the 1D soliton solution belongs to (a) the stable ($\kappa = 1.7$) and (b) the unstable ($\kappa = 3$) branch.

Note that in this case the soliton stripe beam is unstable even at $q=0$, a unique feature of this exponential system. Qualitatively, this behavior can be explained as follows. When $q=0$, the transverse perturbation $\varepsilon(X,Y,\xi)$ described in Eq.(4.6) effectively reduces to the longitudinal perturbation $\varepsilon(X,\xi)$ which in this specific case is known to be unstable, thus giving rise to a complex eigenvalue solution to the generalized eigenvalue problem of Eq.(4.7). Figures 4.3(a-c), depict the propagation dynamics of the stripe soliton corresponding to Fig. 4.2(a). As clearly seen, transverse instability and filamentation persist even when the Rayleigh losses are included in the simulations. Figures 4.3(d-f) show what will happen to the stripe beam corresponding to Fig. 4.2(b) (unstable 1D soliton). In this case, in spite of the scattering losses, the beam quickly disintegrates into collapsing filaments as a result of the synergy of the longitudinal and transverse instabilities.
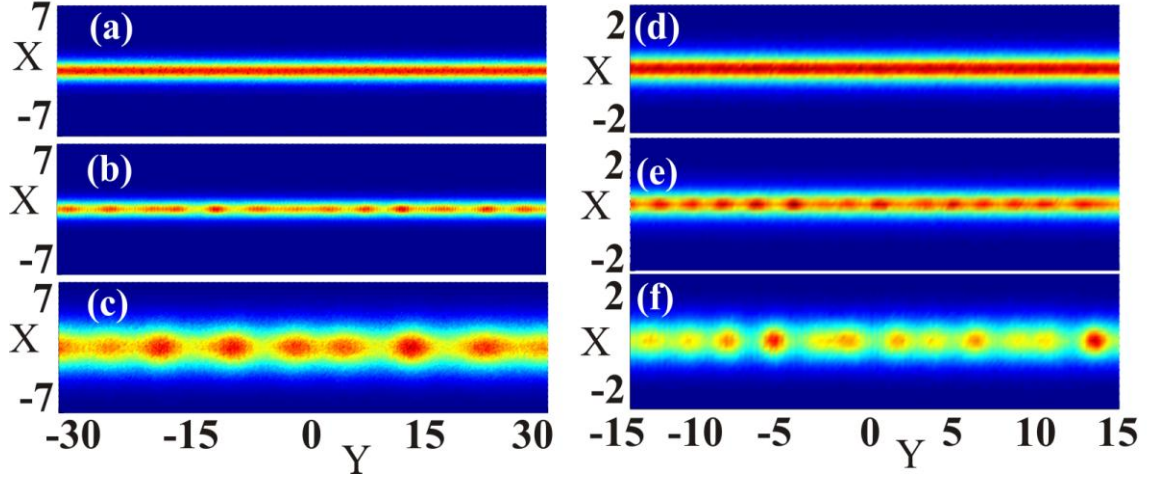
Figure 4.3 (a-c) and (d-f): Propagation dynamics of the stripe soliton beams associated with Figs. 4.2(a) and 4.2(b), respectively. (a),(d): input profiles. Output intensity in (b) a lossless system at $z = 1.9\,nm$, (c) in a lossy system (45% of losses at the output) at 6 mm. (e) depicts the output beam in the absence of losses (after 3 *mm*) while (d) shows the effect of losses (16% after 0.8 *mm* of propagation).

On the other hand, when the nano-particles have a negative polarizability, (nano-particles suspended in a higher refractive index host medium), the 1D soliton solution is always stable and one would expect soliton stripes to be marginally stable at *q=0*, in a way similar to that shown in Fig. 4.2(a). In fact this prediction is in perfect agreement with linear stability analysis as depicted in Fig. 4.4(a) where the normalized gain curve corresponds to the "nano-bubble" suspensions considered in Fig. 4.1(b). The $\beta - q$ diagram in Fig. 4.4(a) was obtained at a power density of 2.8 kW/*cm* when $\kappa = 0.75$. Figs. 4.4(b-d) show propagation dynamics of a stripe soliton beam (that corresponds to Fig. 4.4(a)). In the absence of losses this beam becomes transversely

unstable (Fig.4.4(c)) starting from the $u = 1$ regions where the MI gain is maximum. In Figs. 4.4(b),(c) these regions are located at the two edges of the finite stripe. Fig.4.4(d) shows the output beam when the nonlinear Rayleigh losses are included, In this case the filamentations process affects the entire beam more quickly because of self induced transparency effects [14]. In all previous simulations, in order to keep the simulation window finite, we use very wide super-Gaussian soliton beams in the y direction as opposed to ideal soliton stripes. This explains the high frequency dispersive waves that appear in Fig.4.4 (d) that eventually decay with propagation.
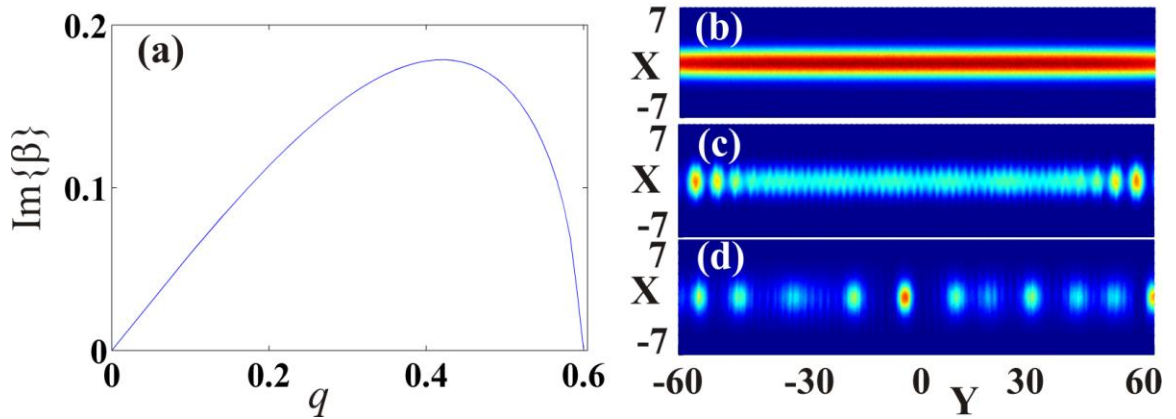
Figure 4.4 (a) Transverse modulational instability gain of a stripe soliton versus perturbation wavenumber for a saturable exponentially nonlinear colloidal dispersion when $\kappa = 0.75$. Corresponding propagation dynamics in this same system after $z = 7$ mm for (b) an input soliton stripe beam, when (c) losses are neglected, and (d) nonlinear Rayleigh losses are included.

CHAPTER FIVE: MANY-BODY INTERACTIONS AND NON-IDEAL "GAS" OF COLLOIDAL NANO-PARTICLES

5.1. Introduction

So far we have neglected any particle-particle interactions in our analysis. In other words we assumed that each particle responds to an external force without being affected by other particles. This approximation corresponds to an ideal "gas" model and hence the particle distribution follows Boltzmann statistics. In this case, the nonlinear response was shown to depend exponentially on the incident optical beam intensity which in turn renders the soliton solutions very unstable, i.e. they undergo a severe collapse as discussed in chapter three. Of course in some cases the nonlinear Rayleigh losses can be strong enough to prevent any collapse. However, in cases where Rayleigh losses can be neglected (when the light beam wavelength is much larger than the particle size) one would expect this model to be valid only at relatively low filling factors. The question naturally arises as to how the system would behave if the particle concentration becomes relatively high. This can happen either because of high initial filling factors or at high levels of optical gradient force. As we will see, in both cases, due to many-particle interactions the nonlinearity is no longer exponential. This situation can be easily understood be keeping in mind that particles can not penetrate each other (due to hard sphere interactions), thus posing an upper limit on the particle packing factor as shown schematically in Fig. 5.1(a). In real colloidal systems, even more complicated types of interactions are involved. For example, in the process of preparing colloidal suspensions, it is very important to stabilize the nano-colloids against flocculation, i.e. introduce

repulsive forces that are capable of overcoming the attractive van der Waals dispersive forces or otherwise the particles will aggregate and eventually sedimentation will occur. This repulsive force can be steric or electrostatic [33,34]. Even though our analysis is general enough to account for any type of inter-particle forces, we here focus our attention on electrostatic interactions- given that it is one of the main techniques typically used to stabilize nano-particle suspensions and in addition the interaction potential is in this case described in closed form.

Starting from a "non-ideal gas" equation of state [18] and by taking into account the screened Coulomb interactions among suspended nano-particles [33-35], we show that the nonlinear optical behavior of these colloids can range anywhere from exponential to polynomial depending on their filling density, composition, and chemistry. The thermodynamics of this problem indicate that while the exponential optical nonlinearity is always present, it can be modified by many-body interactions described by Mayer cluster expansions [18]. This in turn has a profound effect on optical beam dynamics. The stability of optical beams in systems with positive polarizabilities is considered in both 1D and 2D configurations.

5.2. Analysis

Within the context of Gouy-Chapman double layer theory (Fig. 5.1(b)) the electrostatic interaction between two identical suspended nano-particles is described by a Yukawa-like potential [33-35]. The extension of this formalism, the so-called

Derjaguin, Landau, Verwey , Overbeek (DLVO) theory, is also known to account for attractive (London-van der Waals) dispersion forces.
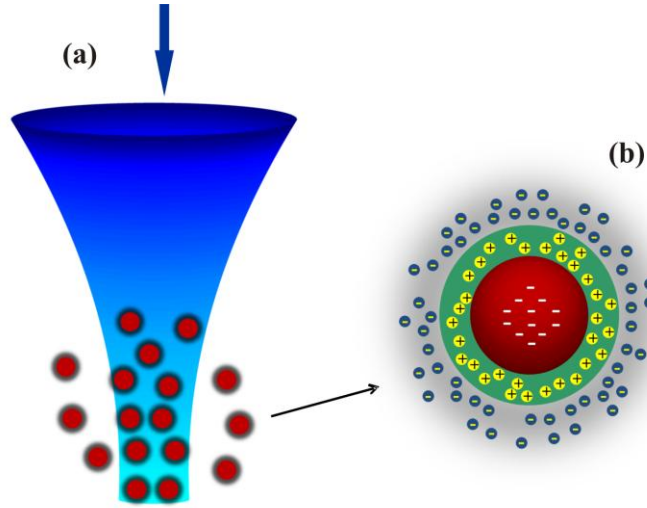
Figure 5.1 (a) Self-focusing of an optical beam in a colloidal nano-suspension. (b) A charged nano-sphere screened by a Gouy-Chapman double-layer.

In this regard, the interaction potential between two identical nano-particles is given by [34,35]:

$$U(r) = \frac{e^2 Q^2}{4\pi\varepsilon_o\varepsilon_r}\left(\frac{e^{\kappa_D a}}{1+\kappa_D a}\right)^2 \frac{e^{-\kappa_D r}}{r} + W(r) \qquad . \quad (5.1)$$

where e is the magnitude of the electron charge, Q is the number of charges per sphere, ε_0 is the free space permittivity and ε_r is the liquid relative permittivity. In Eq.(5.1) a is the particle radius, r is the center to center distance between any two spheres, and $W(r)$ represents the van der Waals attractive potential. The Debye-Hückel screening

length $l_D = 1/\kappa_D$ associated with the electrolyte solution is given by

$$\kappa_D^2 = (e^2/\varepsilon_0\varepsilon_r k_B T)\sum_{i=1}^{M} z_i^2 n_{i\infty}\,.$$ Here k_B is Boltzmann constant, T is the absolute

temperature, z_i is the ionic valency and $n_{i\infty}$ is the ionic number concentration at the

neutral state. In this work we consider only binary electrolytes with $M = 2$. Note that in

aqueous solutions, $n_{i\infty}$ is a direct function of the pH value and as such is an additional

degree of freedom in controlling the optical nonlinear response of the system. For all

practical purposes this interaction energy can be treated as a perturbation on an otherwise

"ideal" gas. Using the total Hamiltonian $H = \sum_{i=1}^{N}(\vec{p}_i \cdot \vec{p}_i)/(2m_p) + \sum_{i<j} U(\vec{r}_i - \vec{r}_j)$ in the grand

canonical partition function of the system Ξ and by considering the thermodynamic limit

where $p_o V = k_B T \ln(\Xi)$, one obtains the equation of state of such non-ideal gas of

colloidal particles [18]. In the above discussion, $U(\vec{r}_i - \vec{r}_j)$ is the interaction potential

between any two particles, p_o is the "osmotic" pressure and V is the total volume.

Under these conditions, the system can be effectively described through a virial

expansion, i.e.,

$$\frac{p_o}{k_B T} = \rho + B_2(T)\rho^2 + B_3(T)\rho^3 + \dots \quad . \quad (5.2)$$

In Eq.(5.2), ρ is the particle density, and B_2 and B_3 are the second and third virial

coefficients, respectively. The second virial coefficient $B_2(T) = -2\pi \int_0^\infty (e^{-U(r)/k_B T} - 1) r^2 dr$,

represents two-body interactions, while the third virial coefficient $B_3(T)$ arises from

three-body effects and is given by:

$B_3(T) = -1/(3V) \int f_u(\vec{r}_1 - \vec{r}_2) f_u(\vec{r}_1 - \vec{r}_3) f_u(\vec{r}_2 - \vec{r}_3) d\vec{r}_1 d\vec{r}_2 d\vec{r}_3,$ where

$f_u(r) = \exp(-U(r)/k_B T) - 1$. Equation (5.2) represents an equation of state for a non-

ideal gas of colloidal nanoparticles and can be also written in a more compact form

$p_o / k_B T = \rho Z(\rho)$ where $Z(\rho) = 1 + B_2(T)\rho + B_3(T)\rho^2 + ...$ is   the   so   called

compressibility factor [33].

From thermodynamical considerations, a generalized form of Fick's law can be

written as $\vec{J} = -D\nabla[\rho Z(\rho)]$ where $\vec{J}$ is the particle current density and D is the

diffusion coefficient. By superimposing the external optical gradient force acting on a

nano-particle we then obtain:

$$\vec{J} = \rho \mu_b \frac{\alpha}{4} \nabla I - D\nabla[\rho Z(\rho)]. \tag{5.3}$$

In Eq.(5.3), μ_b is the particle's mobility, α is its electric polarizability and I is the

optical field intensity. For Rayleigh nanoparticles, the electric polarizability is given by

$\alpha = 3V_p \varepsilon_0 n_b^2 \left(\dfrac{m^2 - 1}{m^2 + 2} \right)$ where $V_p = 4\pi a^3 / 3$ is the particle's volume, ε_0 is the free space

permittivity, and the dimensionless parameter $m = n_p / n_b$ represents the ratio of the particle's refractive index n_p to that of the host medium n_b [20]. Under equilibrium conditions ($\vec{J} = 0$), Eq.(5.3) can be integrated and to third order in the virial expansion we find [36]:

$$\frac{\alpha}{4k_B T}(I - I_0) = \ln\left(f / f_0\right) + \frac{2B_2 f_0}{V_p}\left(\frac{f}{f_0} - 1\right) + \frac{3B_3 f_0^2}{2V_p^2}\left(\left(\frac{f}{f_0}\right)^2 - 1\right) . \tag{5.4}$$

In Eq.(5.4), I_0 is an integration constant and can represent in general a flat background intensity at infinity-here taken to be zero. In addition $f = V_p \rho$ is the local volume filling factor while f_0 stands for the filling factor at infinity where the beam intensity is assumed to vanish ($I_0 = 0$). In deriving Eq.(5.4), Einstein's relation $D / \mu_b = k_B T$ was used. Note that in the absence of any particle-particle interactions ($B_{2,3} = 0$), the nonlinear response of Eq.(5.4) (e.g. the logarithmic term) reduces to the previously considered ideal-gas Boltzmann distribution of Eq.(2.6)[14]. We remark that Eq. (5.4) is a generic result in which the details of the inter-particle interactions are contained in the specific values of $B_{2,3}$. In particular, our conclusions below regarding the appearance of a super-Kerr nonlinear response are theoretically founded on Eq. (5.4) as opposed to the specific model of screened Coulomb interactions treated here. It is in this sense that our analysis can serve as a theoretical foundation for a super-Kerr nonlinear response.

Using Eq.(5.4) in conjunction with Eq.(2.11) and by introducing the same normalizations as before, i.e. $,\xi = z / z_0 , z_0^{-1} = k_0 |n_p - n_b| f_0,$ $X = x / w$, $Y = y / w$, $w^2 = z_0 / (2 k_0 n_b) , \phi = (4 k_B T / |\alpha|)^{1/2} \varphi$, we obtain:

$$i \frac{\partial \varphi}{\partial \xi} + \varphi_{XX} + \varphi_{YY} + \operatorname{sgn}(\alpha) \gamma \varphi + i \frac{\sigma}{2 k_0 |n_p - n_b| V_p} \gamma \varphi = 0 \quad , \qquad (5.5\text{-a})$$

$$\operatorname{sgn}(\alpha) |\varphi|^2 = \ln(\gamma) + \frac{2 B_2 f_0}{V_p} (\gamma - 1) + \frac{3 B_3 f_0^2}{2 V_p^2} (\gamma^2 - 1) . \qquad (5.5\text{-b})$$

In Eq. (5.5), $\gamma = f / f_0$ is a filling factor ratio, $\operatorname{sgn}(\alpha) = +1$ when $\alpha > 0$ or $n_p > n_b$ and $\operatorname{sgn}(\alpha) = -1$ for negative polarizabilities, e.g. $n_p < n_b$. We note that at low densities $(f_0 \to 0)$ the nonlinear response of the system given by Eq.(5.5-b) reduces to the Boltzmann exponential distribution of an ideal gas [14]. The two coupled equations (5.5-a) and (5.5-b) describe nonlinear optical dynamics in a non-ideal gas of interacting nano-colloidal particles. This nonlinear system can be solved numerically in both 1D and 2D geometries in order to extract information as to the propagation and stability properties of optical beams in such colloidal suspensions [36].

5.3. Results

To appreciate the effects arising from Coulomb screening, we have evaluated the first two virial coefficients based on a linearized Gouy-Chapman double-layer theory or a Debye-Hückel model (DH) [34]. For simplicity we have also ignored the van der Waals component in the interaction potential. For comparison purposes, we plot both the

nonlinear behavior calculated from DH theory and that obtained from the ideal Boltzmann model for a specific set of parameters. In this example we assumed an aqueous solution of polystyrene nanoparticles ($a = 50nm$) at a pH=6, and a filling factor $f_0 = 10^{-3}$. The average charge per particle was taken here to be $Q = 20$. Under these conditions, $B_2 / V_p \approx 300$ and $B_3 / V_p^2 \approx 7 \times 10^3$. For this case, Fig. 5.2 (a) depicts the nonlinear response of this non-ideal gas of interacting particles as a function of the normalized intensity $\left(|\alpha|/4k_B T\right) I$ -as obtained from Eq. (5.4). As shown in chapter three, the nonlinear index change is always proportional to the filling factor f [14].
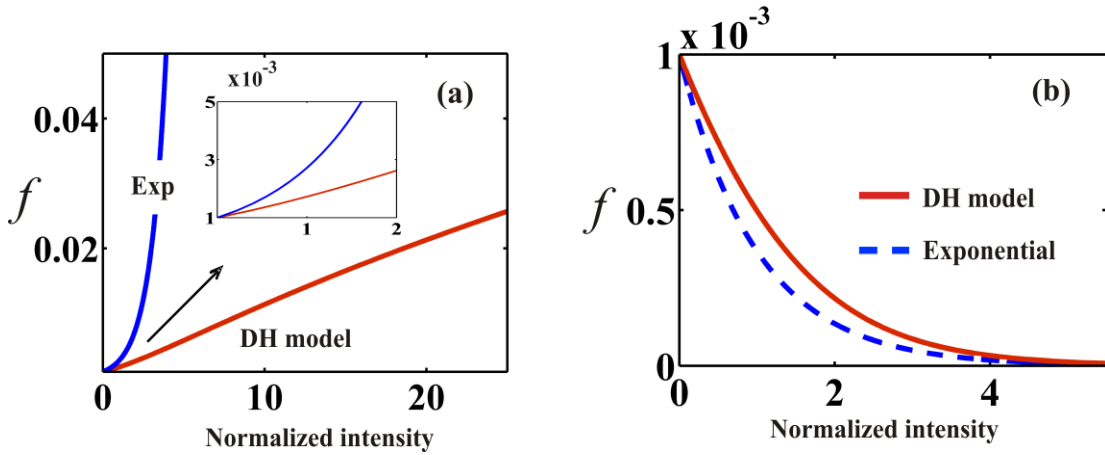
Figure 5.2 Volume filling factor or nonlinearity versus normalized intensity as obtained from the Debye-Hückel theory (DH) and the Boltzmann exponential model (a) positive polarizabilities (b) negative polarizabilities. The system parameters are given in the text. The inset in (a) provides an expanded view at low filling factors.

As Fig. 5.2(a) indicates, in this range of parameters, the DH curve quickly deviates from the Boltzmann distribution even at very low filling factors, slightly

exceeding f_0-as shown in the inset of Fig.5.2(a). This behavior is in contrast to that expected from the Carnahan-Starling hard-sphere model where significant deviations from the exponential model only occur at much higher packing factors- exceeding 5% [37,38]. In fact, the competition between the Boltzmann distribution and repulsive interactions leads to an optical response that can range anywhere from exponential to polynomial depending on their filling density, composition, and chemistry. Interestingly, even though at high filling densities the exponential distribution can be overshadowed by the higher virial terms, the Kerr coefficient (to lowest order in intensity I) is largely affected by the Boltzmann term, e.g. $\Delta n(I) = (n_p - n_b)f_0[1 + (2B_2 f_0 / V_p) + ...]^{-1}(\alpha I / 4k_B T)$. On the other hand however, for negative polarizabilities, the exponential term *dominates* the saturable self-focusing optical nonlinearity of this colloidal system, as clearly shown in Fig. 5.2(b). In this regime, the deviation between the Boltzmann and DH curves is small since the nano-particles are in this case expelled away from the center of the beam, thus reducing many-particle interaction effects.

We next investigate how many-body interactions may affect the nonlinear dynamics of optical beams propagating in such colloidal systems. A feature that is directly related to the nonlinear response itself is beam stability. To explore optical beam stability in these media, we first consider self-trapped solutions or optical solitons of the form $\varphi = G(X,Y)\exp(i\kappa\xi)$ and plot their power-eigenvalue diagrams where the normalized power is given by $P = \int |G|^2 dxdy$. Figures 5.3(a) and 5.3(b) depict this

behavior for both 1D and 2D configurations respectively-obtained for the same parameters used for Figs. 5.2. From the Vakhitov-Kolokolov criterion [24] one can directly infer that for these specific parameters one-dimensional optical self-trapped channels are stable while their 2D counterparts are unstable. This behavior is consistent with the super-Kerr character of the nonlinear optical response mentioned above. Clearly, this stability behavior can be greatly altered depending on the parameters of the colloidal system itself.
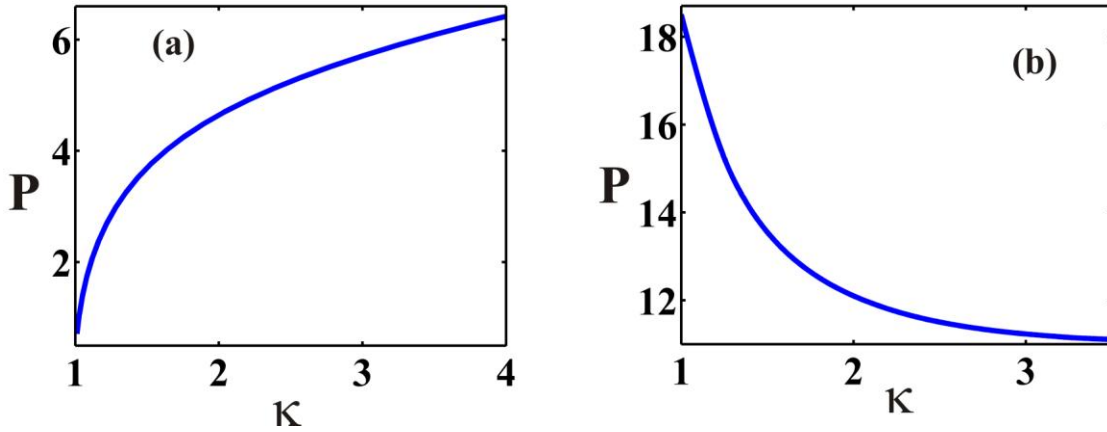
Figure 5.3 Power-eigenvalue diagrams for (a) one-dimensional stripe solitons (b) 2D solitons. The parameters used are identical to those of Fig. 5.2(a).

For example, 1D solitons can be destabilized if the strength of the interaction is reduced. This can be accomplished either by reducing the initial filling factor (dilute gas) or by altering the chemistry of the solution-thus enhancing screening effects. In that case the nonlinear response will approach the Boltzmann distribution-rendering even 1D stripe solitons unstable. On the other hand, for 2D self-trapped beams, the presence of inter-particle interactions tends to slow-down the self-focusing collapse that would have been

otherwise severe in a purely exponential model. We note that for negative polarizabilities the self-focusing nonlinearity is saturable and hence all soliton solutions are stable [14]. The signature of many-body effects on beam propagation can be used to optically extract valuable information concerning the nature of the interaction potential by estimating the virial coefficients. Figure 5.4, shows beam propagation of a 2D optical self-trapped beam in this same system (corresponding to Fig.5.2(a)) at a wavelength of $\lambda = 0.532\,\mu m$. Figure 5.4(a) depicts the dynamics of a Gaussian beam of $FWHM = 7\,\mu m$ at a power level of 1 Watt over a distance of $1mm$ of propagation (3.5 diffraction lengths) when nonlinear Rayleigh losses are taken into account. In this environment the beam undergoes expansion since the power is not enough to cause self-trapping. Figure 5.4(b) on the other hand depicts the intensity evolution of this beam in this same system when the charge per particle is reduced to one half ($Q = 10$).
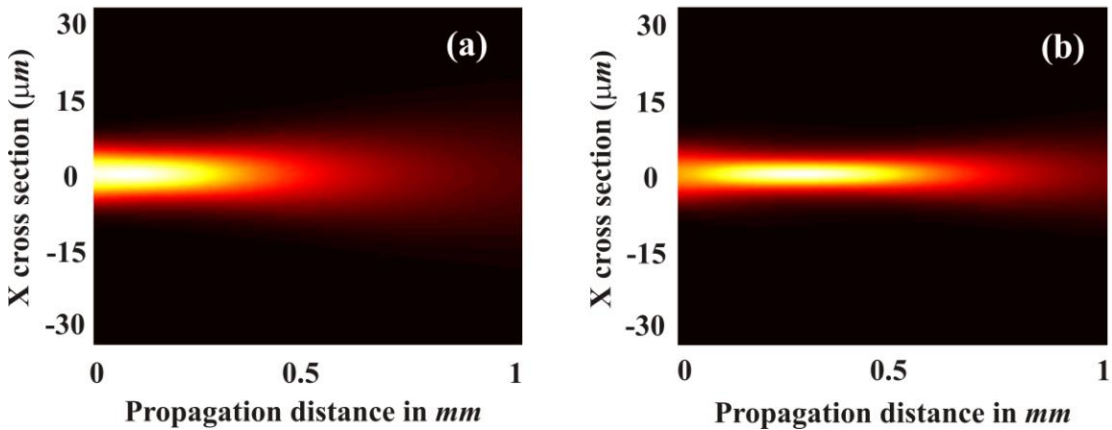
Figure 5.4 Propagation dynamics of a $7\,\mu m$ FWHM Gaussian beam at a power level of 1 W (a) for the same system parameters used in Fig. 5.2 (b) when the charge per particle is reduced to $Q = 10$.

In this case, the optical wave is initially compressed because of reduced inter-particle interactions and forms a self-trapped state before nonlinear losses take over. Note that in the absence of nonlinear Rayleigh losses, the beam would have collapsed after a small propagation distance because of the super critical nature of the optical nonlinearity in 2D. Our simulations indicate that the nonlinear beam dynamics, e.g. the output spot size versus input power, is sensitive to the inter-particle interactions and can therefore be used as a probe of these processes.

In summary, we have examined the effect of many-body interactions on the optical nonlinearity of colloidal nano-suspensions. By considering the screened Coulomb repulsions between nano-particles we found that the nonlinear optical behavior of these colloids can range from polynomial to exponential depending on their composition and chemistry. The dynamical behavior of optical beams propagating in such non-ideal gas environments of interacting particles was considered and characterized.

CHAPTER SIX: EXPERIMENTAL STUDY OF NONLINEAR OPTICAL RESPONSE OF COLLOIDAL SUSPENSIONS

In the previous chapters different models were proposed to describe the nature of the nonlinear optical interaction of a light beam propagating in colloidal nano-particles [4,14,36]. In particular, based on the strength of the interaction between the nano-spheres, it was shown that the nonlinear optical response can be either exponential or polynomial [36]. It would be certainly of interest to test these predictions against measurements. In this chapter we present the experimental results aiming at probing [39] the nonlinear optical response of aqueous nano-colloidal suspensions. The goal is to provide a test of previous theoretical approaches so far proposed for this nonlinearity; namely the exponential model [14], artificial Kerr medium [4-6], and the non-ideal gas model [36]. As we will see, the best agreement with experiment [39] is obtained using the non-ideal gas model for the colloidal suspension which in turn can be used to infer values for the second virial coefficient (see chapter 5) of the medium and the associated nonlinear coefficients.

6.1. Experiment

The experimental setup used to probe the nonlinear optical response of nano-suspensions is shown in Fig.6.1. Two oppositely directed and aligned identical single-mode optical fibers are inserted into the colloidal suspension and separated by a distance D, shown in the inset of Fig.6.1. In this scheme, a well defined optical beam (with variable input power) is launched directly into the colloidal suspension from the input

single-mode fiber to the left. The collecting fiber to the right is used to measure the power coupled into the same single-mode beam profile after propagating a distance D. The fiber mode profile was well characterized by a Gaussian field of spot size w_0, and the distance D was typically a few times the Rayleigh range of the initial Gaussian beam. We note that our experimental setup is reminiscent of the classic Z-scan technique used for measuring Kerr nonlinearities with the collecting fiber playing the role of the aperture in the Z-scan method [41]. In our case, however, it is the input power that is scanned. The key advantage of this technique is to gain direct access to the nonlinear suspension within the aqueous medium. In addition, this approach eliminates any spherical aberration due to beam propagation through the glass and water interfaces present for cuvette-type geometries, and by reducing the sample chamber (from a cuvette) it is possible to greatly reduce thermal convection flows within the sample.
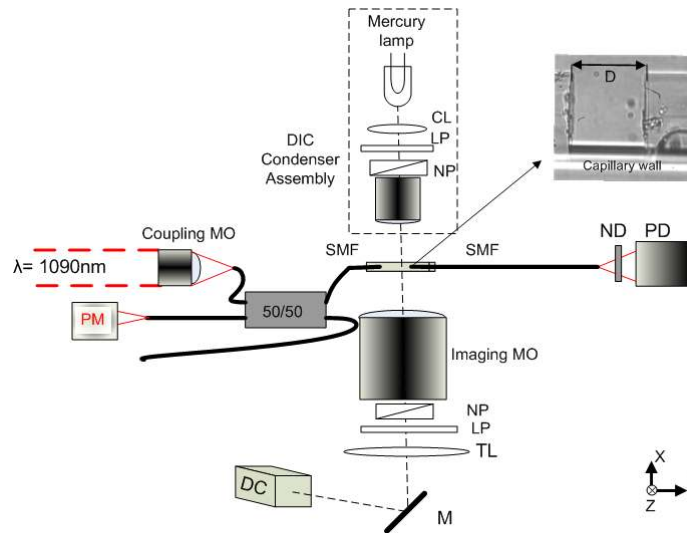
Figure 6.1 The experimental setup.

Here we treat the colloidal suspension as a self-focusing Kerr medium with a critical power P_{crK} for self-focusing or self-trapping. For input powers much less than P_{crK}, linear diffraction takes place and as a result the power at the collecting fiber P_{coll} will be a fraction of the input power. The ratio P_{coll}/P_{crK} is determined from beam spreading and wavefront curvature that accumulate over the distance D. However, as the input power is increased towards the critical power, nonlinear effects starts to come into play, reducing beam diffraction and hence increasing the fraction of power at the collecting fiber. For the special case when the input power equals the P_{crK}, the input beam should propagate with unchanging beam profile between the fibers leading to, in principle, perfect power coupling. In reality, due to nonlinear Rayleigh losses, this scenario will be altered depending on the strength of the losses. Increasing the input power beyond P_{crK} is expected to lead to beam self-focusing between the fibers before losses and diffraction takes over, resulting in a deduction of the power coupled into the collecting fiber. Thus for a Kerr medium the critical power for self-focusing can be estimated experimentally by looking for a peak or rollover in the plot of the measured power P_{coll} at the collecting fiber versus input power P_{in}.

6.2. Experimental details and results

We now turn to a more detailed description of the experimental setup in Fig.6.1. A linearly polarized laser (10 W, 1090 nm, SPI laser) is coupled into a 50/50 fiber splitter (FC1064-50-FC- 2x2 SM Coupler) using a three positioning fiber coupling stage

(MDE122, Elliot scientific) with a microscope objective and coupling objective (10X, 0.25NA, Comar). The beam profile of the single-mode fibers is well characterized as a Gaussian with spot size w_0=3.4 μm at the wavelength $\lambda = 1.09 \mu m$ (this wavelength was chosen so as to reduce Rayleigh scattering losses). One end of the fiber splitter is directed onto a power meter, PM (Melles Griot) to monitor the power fluctuations in the laser and fiber coupling stage ($<2\%$). The other end of the splitter is coupled, via FC connector, into a single ended cleaved single mode fiber, SMF (1060XP, Thorlabs, mode field diameter to $6.8 \mu m$). The cleaved end of the fiber is then inserted into a capillary of inner diameter of $200 \mu m$ (Invitrocom) as shown in the inset. The sample is mounted onto an X-Y translations stage (H117, Prior Scientific) within an inverted microscope platform (TE2000E, Nikon). A microscope objective (imaging MO) (20X, NA DIC 0.50 NA, Nikon) is used to image the sample onto a high speed digital camera (DC) (A622f Basler) via a tube lens (TL). A condenser assembly to support differential interference contrast (DIC) illumination is used (LP − linear polarizer, NP −_Nomarski prism). The same polarization optics is placed in the imaging path so as to pick up the small phase difference within the sample. The DIC illumination technique has previously been used to visualize single nanoparticles [42].

The cleaved end of a second identical single mode fiber (1060XP, Thorlabs, mode field diameter) is inserted into the other end of the capillary and brought to a known distance away from the input face of fiber. Once the two fibers are aligned, the whole chamber is subsequently sealed with epoxy to reduce fluctuations. The output of the second fiber illuminates an Indium gallium arsenide (InGaAs) photodetector, PD (PDA10CS-EC,

Thorlabs), which in turn measures the coupled power. A set of calibrated neutral density filter is used so as to prevent over exposure onto the PD. A custom Labview program is used to remotely control the input power and capture the coupled power at the PD using a data acquisition device (National instruments NI USB-6009). The nanoparticles used here are polystyrene plain spheres of diameter $2a = 0.099 \mu m$ (10% coefficient of variation), a being the radius (PS02N/6391, Bangs Lab). The spheres are treated with a sulfate groups: 0.1% SDS (sodium dodecyl sulfate) and 0.05% sodium azide anti-microbial agent. The initial concentration is 1.921×10^{14} particles/cm^3. For each dilution step, heavy water (D_2O - having low absorption at $\lambda = 1.09 \mu m$) is used as the diluting agent so as to reduce thermal convection flow.For the coupling power measurements, two samples have been prepared with colloidal densities of $\rho_0 = 1.921 \times 10^{13}$ and $\rho_0 = 1.921 \times 10^{12}$ particles/cm^3. The collecting fiber is placed at a distance $D = 110 \pm 10 \mu m$ away from the input fiber. For each run, a total of 200 data points were taken and averaged over a 1 second acquisition time. At lower input powers ($< 400 mW$), the collected power varies linearly with the input power (the difference in the power plots is due to slight misalignment in z).

Figure 6.2 shows the experimental results for the power measured at the collecting fiber (P_{coll}) versus input power (P_{in}) for the two concentrations mentioned above. In the first case of lower density suspensions (dash-dot line) the input power remains well below the critical power (5 W) and the collected power varies linearly with the input power. For the higher density colloids (solid line) the collected power scales linearly for lower input

powers, rises above the low concentration linear plot for higher powers, and finally there

is a peak in the plot of P_{coll} versus P_{in} akin to that discussed above for the case of a Kerr

medium, the rollover occurring at $P_{roll} \approx 0.5$ W. Due to the thin capillary walls, we are

also able to observe the alignment of the nanoparticles under DIC illumination for the

concentration of 1.921×10^{13} particles/cm^3. In the inset of Fig. 6.2, we show two

brightfield images for input powers of 0 W and 0.514 where for the latter case we can see

a fine track in the refractive index from the DIC illumination upon the sample, this

corresponding to the formation a fine channel of increased nanoparticle density.

We have also performed standard Z-scan measurement [41] to obtain the value of the

nonlinear Kerr coefficient n_2 for the sample concentration of $\rho_0 = 1.921 \times 10^{13}$ cm^{-3}. In

order to satisfy the Z-scan requirements (sample thickness larger than beam's Rayleigh

length), we increased the input beam spot size to $15 \, \mu m$ (measured in air). The beam was

directed into a sealed sample cell of $100 \, \mu m$ thickness that is scanned in $10 \, \mu m$ steps

using a motorized stage (T-LS Series, Zaber Technologies). The transmitted power is

collected and measured after passing through a 3 mm aperture. The measured nonlinear

coefficient was approximately $n_2 = 2 \times 10^{-9} cm^2 / W$. We comment that the nonlinear

coefficient is comparable with previous measured values, and the scattering loss

(measured at lower power) in the sample at wavelength of $1.09 \, \mu m$ is $3.91 cm^{-1}$ which is

much lower than that reported in the visible [6].
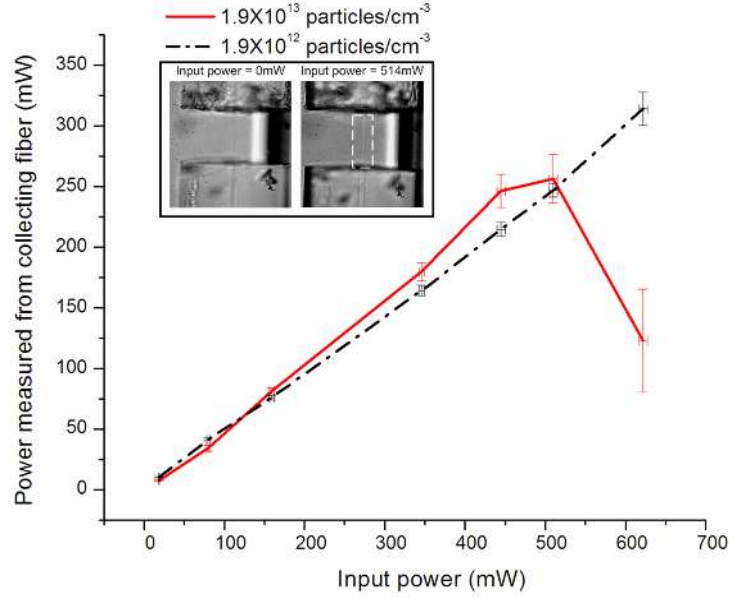
Figure 6.2 Plot of power measured at collecting fiber with a photodetector versus the input power for the two concentrations indicated. Insets show the DIC image of two position when input power is 0 *mW* and 514 *mW*.

6.3. Field propagation equation

In order to understand the results presented in Fig.6.2 we use the theoretical models derived in chapters five where the beam evolution equation for the optical field envelop can be described as

$$\frac{\partial \varphi}{\partial z} = \frac{i}{2k_0 n_b}\left(\frac{\partial^2}{\partial x^2} + \frac{\partial^2}{\partial y^2}\right)\varphi + \sigma\rho_0\left(i\Omega - \frac{1}{2}\right)r\varphi \ , \qquad (6.1)$$

Where as before the Rayleight scattering cross section is given by:

$$\sigma = \frac{128\pi^5 a^2 n_b^4}{3} \left(\frac{a}{\lambda_0}\right)^4 \left(\frac{m^2-1}{m^2+2}\right)^2 \quad , \quad (6.2)$$

In Eq.(6.1), the factor $r = f / f_0$ with $r = 1$ for zero optical intensity and and $\Omega = k_0 (n_p - n_b) V_p / \sigma$ is a dimensionless constant that reflects the strength of the self-focusing nonlinearity to the nonlinear Rayleigh scattering losses.

Note that, as shown in previous chapters, different models for the nonlinear optical response colloidal suspensions correspond to different choices for the factor r. For comparison with the experiment the following parameters are used:

$\lambda = 1.09 \, \mu m, n_p = 1.57, n_b = 1.33, \rho_0 = 1.9 \times 10^{13} \, cm^{-3}, a = 50 \, nm, \ f_0 = 0.01$, and $D = 110 \, \mu m$,

corresponding to polystyrene spheres in water. In this wavelength region, the Rayleigh scattering losses due to the colloidal particles is expected to be very small, and we have verified this in numerical simulations with and without the losses.

We shall employ Eq. (6.1) for propagation between the input and collecting fibers along with the initial Gaussian field representing the field launched by the input fiber at z=0

$$\varphi(x, y, 0) = \sqrt{\frac{2 P_{in}}{\pi w_0^2}} e^{-(x^2+y^2)/w_0^2} \quad , \quad (6.3)$$

with input spot size w_0 and input power P_{in}. Once the propagated field $\varphi(x, y, D)$ is calculated we can calculate the power at the collecting fiber via the overlap integral

$$P_{coll} = \left| \sqrt{\frac{2}{\pi w_0^2}} \int dx dy\, e^{-(x^2+y^2)/w_0^2} \varphi(x, y, D) \right|^2 \quad , \quad (6.4)$$

which is the modulus squared of the propagated field projected onto the collecting fiber mode. For comparison with the experiment we shall use the spot size $w_0 = 3.4\,\mu m$.

6.4. Medium equations

From Eq. (6.1) the nonlinear change in the refractive-index Δn of the colloidal medium is related to the ratio r via the relation $k_o \Delta n = \sigma \rho_0 \Omega r$, leading to the expansion

$$\Delta n(I) = \left(\frac{\sigma \rho_0 \Omega}{k_0}\right) r(I) = (n_p - n_b)V_p \rho_0 \left(1 + r'I + \frac{r''}{2}I^2 + ...\right)$$
$$= \Delta n(0) + n_2 I + n_4 I^2 + ... \quad , \tag{6.5}$$

where $r' = (dr/dI)|_{I=0}$. In general the ratio r must be determined from the equation of state of the soft condensed matter system exposed to the laser field (see chapter 5). In order to verify the theoretical model presented in our previous studies [36] we treat the colloidal suspension as a non-ideal "Van der Waals" gas to allow for compressibility of the colloidal suspension, and by keeping the second and third virial coefficients B_2 and B_3, the relation between the optical intensity I and the ratio r can be written as

$$\frac{\alpha I}{4k_B T} = \ln(r) + 2\left(\frac{B_2}{V_p}\right)f_0(r-1) + \frac{3}{2}\left(\frac{B_3}{V_p^2}\right)f_0^2(r^2-1) \quad , \tag{6.6}$$

where the particle polarizability is given by $\alpha = 3V_p \varepsilon_0 n_b^2 (m^2 - 1)/(m^2 + 2)$. Equation (6.4) is valid when the virial expansion converges

$$\frac{p}{k_B T} = \rho + B_2 \rho^2 + B_3 \rho^3 + ... \approx \rho\left(1 + B_2 \rho + B_3 \rho^2\right) \quad , (6.7)$$

with p and ρ the osmotic pressure and density of the colloidal suspensions, which is valid if $(B_2/V_p)f_{max} < 1$, and $(B_3/V_p^2)f_{max}^2 < 1$. The values of the virial coefficients depend on the details and the nature of interaction between nano-spheres. Hard sphere interactions was proposed as a mechanism that accounts for the nonlinear optical behaviors of nano-suspensions [37,38] but it was shown that simulations resulting from these types of interactions are in complete disagreement with experimental results and that one has to take into consideration even more complicated inter-body forces such as double layer [33,34] or steric potentials. We would like to emphasize that our treatment though limited to the second and third virial coefficients allows, in principle, for the inclusion of arbitrary inter-particle interaction potentials.

In the limit of an "ideal gas" in which particle-particle interactions are neglected, $(B_2/V_p)f_{max} \to 0, (B_3/V_p^2)f_{max}^2 \to 0$, Eq.(6.6) yields $r(I) = \exp(I/I_c)$, where $I_c = 4k_B T/\alpha$, giving the limit of the exponential model for the nonlinearity

$$\Delta n(I) = (n_p - n_b)V_p \rho_0 e^{I/I_c} \approx n_{2K} I_c + n_{2K} I, \quad (6.8)$$

54

where we identify the nonlinear coefficient $n_{2K} = (n_p - n_b)V_p \rho_0 / I_c$ in the limit of an *artificial Kerr medium.* In contrast, combining Eqs. (6.5) and (6.6) for the non-ideal gas case with B_2 and B_3 non-zero yields

$$n_2 = \left(\frac{n_{2K}}{1 + 2(B_2/V_p)f_0 + 3(B_3/V_p^2)f_0^2} \right),$$

$$n_4 = \frac{n_{2K}}{2I_c} \left(\frac{1 - 3(B_3/V_p^2)f_0^2}{\left[1 + 2(B_2/V_p)f_0 + 3(B_3/V_p^2)f_0^2 \right]^3} \right) . \tag{6.9}$$

From the above formulae, it is evident that the effects of the many-body interactions is to soften the effective Kerr nonlinear optical response with respect to the exponential model since $n_2 < n_{2K}$, but that higher-order nonlinearities are also present yielding a super-Kerr nonlinear response (n_4 term).

In addition to the parameter values mentioned above, and in order to facilitate comparison with the experiment we shall set $B_3 = 0$ and vary the scaled second virial coefficient (B_2/V_p) which we expect to be dominant. Figure 6.3 shows the variation of the scaled nonlinear index change $[\Delta n(I)/n_{2K}I_c - 1]$ versus scaled intensity (I/I_c) for $B_2/V_p = 25$ as described by Eq.(6.6) (solid line) along with that obtained from the exponential model in Eq. (6.8). Evidently, a considerable softening of the exponential model is clearly indicated by the fact that the index change increases far less rapidly with

intensity for the non-ideal gas. Inclusion of the virial coefficients is therefore an important factor in understanding how the exponential model can give way to the notion of an artificial Kerr medium or a super-Kerr nonlinear response.
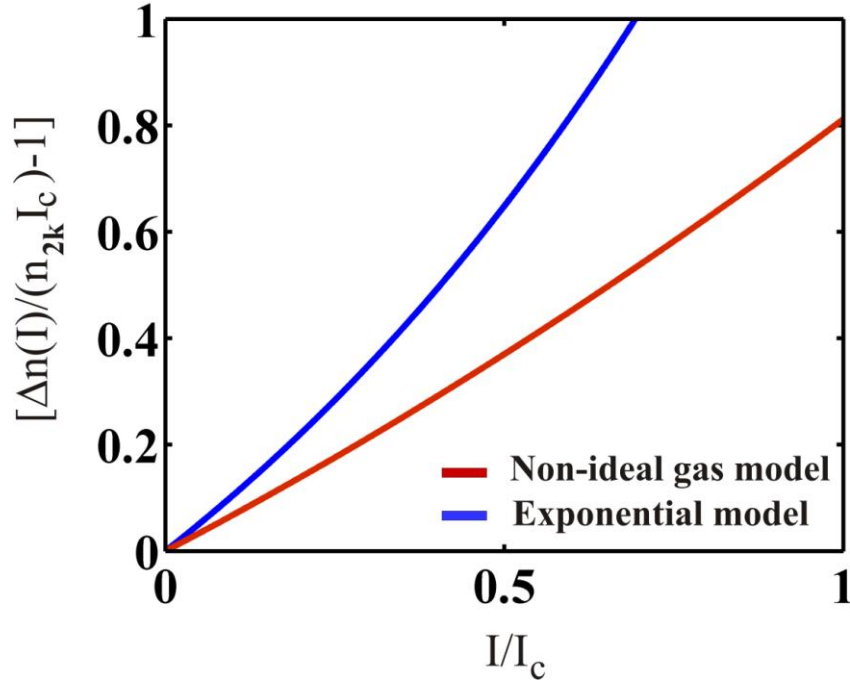
Figure 6.3 The variation of the scaled nonlinear index change $[\Delta n(I)/n_{2K}I_c - 1]$ versus scaled intensity (I/I_c) for $B_2/V_p = 25$ using both the non-ideal gas model in Eq. (6.6) (red line) and the exponential model in Eq. (6.8) (blue line).

6.5. Numerical results

In order to analyze the experimental results in Fig. 6.2 we use both numerical and semi-analytical techniques. More specifically we employ Beam Propagation Method (BPM) simulations based on Eqs. (6.1)-(6.4), and also a variational Gaussian (VG) model based on the non-ideal gas model in Eq. (6.9) using n_2 and n_4. Although the BPM

results are ultimately more accurate we concentrate on the VG model as it offers some

insights into the underlying physics and it is important as a check on the purely numerical

BPM results. In all cases we checked that the same trends occur in both the BPM and

VG results. First we describe our VG model and then we turn to our numerical results.

Throughout our numerical study the parameters used are those previously quoted unless

otherwise stated.

To analyze propagation of the initial Gaussian beam (6.3) according to Eq. (6.1) we use

the variational approach of Anderson and Bonnedal [43]. In particular, we use the results

for n_2 and n_4 for the non-ideal gas in Eq. (6.1) by replacing $\sigma \rho_0 \Omega r = k_0 n_2 I + k_0 n_4 I^2$,

and we set the Rayleigh scattering losses to zero. In the variational approach a suitable

Lagrangian is introduced that yields the paraxial wave equation (6.1) when the Euler-

Lagrange equations are evaluated. Although this makes an exact solution no easier it

permits an approximation based on a prescribed trial function, which we choose here as a

Gaussian

$$\varphi(x, y, z) = \sqrt{\frac{2P_{in}}{\pi w^2(D)}} e^{i\vartheta_T(z)} e^{(-(x^2+y^2)/w^2(z)+ik(x^2+y^2)/2R(z))} , \quad (6.10)$$

where $\vartheta_T(z)$ is the on-axis phase of the field, $w(z)$ is the Gaussian spot size of the

propagating field, and $R(z)$ is the radius of curvature of the field. Here we solve the

problem under the initial conditions $w(z) = w_0$ and $1/R(z) = 0$ since the initial Gaussian

is collimated. By evaluating the Euler-Lagrange equations we find the equations of

motion for the Gaussian beam spot size and radius of curvature [43,44]

$$\frac{d^2 w}{dz^2} = \frac{4}{k^2 w^3} \left(1 - \frac{P_{in}}{P_{cr}} - \frac{8w_0^2}{9w^2} \left(\frac{n_4 I_{cr}}{n_2} \right) \left(\frac{P_{in}}{P_{cr}} \right)^2 \right), \quad \frac{1}{R(z)} = \frac{1}{w}\frac{dw}{dz}, \quad (6.11)$$

where the critical power for self-focusing due to the Kerr effect alone (n_2) for a Gaussian

beam is given by:

$$P_{cr} = \frac{1.8962\lambda^2}{4\pi n_b n_2}, \quad (6.12)$$

and $I_{cr} = 2P_{cr}/\pi w_0^2$. These equations can be solved to find the Gaussian spot size and

radius of curvature at the collecting fiber, and the measured power calculated using

$$P_{coll} = \left| \sqrt{\frac{4P_{in}}{\pi^2 w_0^2 w^2(D)}} \int dxdy e^{-(x^2+y^2)/w_0^2} e^{-(x^2+y^2)/w^2(D)+ik(x^2+y^2)/2R(D)} \right|^2$$

$$= \frac{4P_{in}\left(w_0^2/w^2(D) \right)}{\left| 1 + \left(\frac{w_0^2}{w^2(D)} \right) - \frac{ikw_0^2}{2R(D)} \right|^2},$$

$$(6.13)$$

Physically, Eq. (6.13) is the modulus squared of the propagated Gaussian field projected

onto the collecting fiber mode. Note that both the propagated beam spot size $w(D)$ and

the beam curvature $R(D)$ affect the power measured at the collecting fiber.

Equation (6.11) is solved numerically for a given set of parameters and under the initial

condition $w(0) = w_0, dw(0)/dz = 0$ for an incident collimated beam ($1/R(z) = 0$). The

collimated power is then obtained using Eq. (6.13). One can gain physical insight into the self-focusing dynamics by recognizing that Eq. (6.11) is analogous to Newton's equation for a unit mass particle moving in one dimension with w playing the role of the particle coordinate, z the role of time, and the right-hand-side being the force. Self-focusing contraction of the beam occurs when the force is negative meaning that the particle is attracted to the origin ($w=0$). Note that for an artificial Kerr medium ($n_2 > 0, n_4 = 0$) the force is negative and self-focusing collapse occurs only when $P_{in} > P_{cr}$. On the other hand, when the non-ideal gas model with both $n_2, n_4 > 0$ is considered, the force can be negative even for $P_{in} < P_{cr}$ (depending on the magnitude of the higher-order terms), thus leading self-focusing collapse phenomena even for input powers lower than the critical one, i.e. $P_{in} < P_{cr}$. This result shows clearly that artificial Kerr nonlinear coefficient alone will not be sufficient to account for the beam dynamics experimentally observed in interacting nano-colloidal system.

Numerical simulations based on Eq. (6.1) and the exponential nonlinearity (Eq. (6.6) with all virial coefficients equal zero) were also carried out. It was found that under no conditions can one fit the model to the experimentally obtained data. This is because the exponential nonlinearity includes arbitrarily high orders of self-focusing nonlinearity, hence once self-focusing collapse starts it is immediately super-critical [40], leaving no room for the relatively smooth rollover seen in Fig. 6.2. In fact the exponential nonlinear model predict that the plot of the collected versus the input power is initially linear with the input, then it increases very sharply with increasing input power, and finally drops abruptly to zero above a given power level. (This plot is not included due to lack of

59

numerical accuracy after the collapse takes place).   We conclude that the pure exponential model is therefore not a good representation of the nonlinear optical response of the experiment under investigation.

We next consider the numerical results treating the colloidal suspension as an artificial Kerr medium. In other words, we truncate the exponential nonlinearity to the first nonlinear term as shown in Eq. (6.8). For the same system parameters as before, we find that $n_{2K} = 2.3 \times 10^{-9} \, cm^2 / W$. From Eq. (6.11) one can calculate the critical power by setting $n_2 = n_{2K}$. By doing so we find that $P_{crK} = 0.6W$ (We remark that the critical power for the lower concentration example in Fig. 6.2 calculated in this manner is 5 W). Figure 6.4 depicts the results of these simulations with both collected and input powers being normalized to P_{crK} . The dashed line is obtained using the VG model and the solid line is obtained using the BPM with good overall agreement between the models. In this case, we see that the rollover occurs at an input power $P_{roll} = 0.6W$ for both models, in agreement with the experimental value of 0.5 W. Indeed, fine tuning of the numerical parameters can easily reduce the difference in the rollover powers between the experiment and models. However, as was discussed in the previous chapter, the artificial Kerr model contradicts the Boltzmann statistics and the natural question arising here is whether the one can explain the experimental data starting from first principles and by taking into account many-body effects?
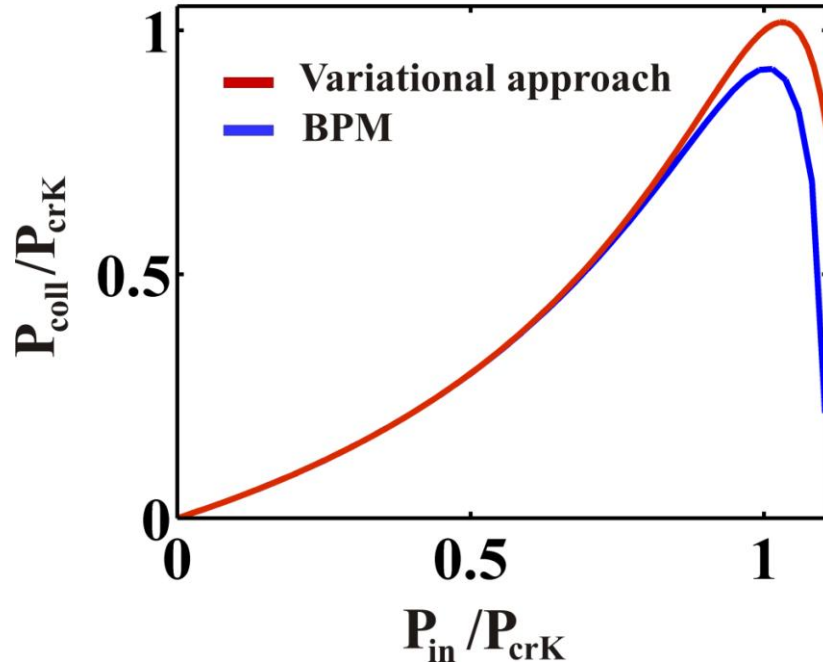
Figure 6.4 shows simulation results for the power collected by the output fiber versus the input power using the artificial Kerr medium model, both powers being normalized to the critical power for self-focusing P_{crK}. The red line is obtained using the VG model and the blue line is obtained using the BPM.

Finally we present VG results based on the non-ideal gas model with values for the nonlinear coefficients n_2 and n_4 based on Eq. (6.9) for the previous quoted parameter values and varying values of the second virial coefficient (B_2/V_p) (here we assume $B_3 = 0$). It is evident from Eq. (6.9) that increasing (B_2/V_p) past zero will reduce the Kerr nonlinear coefficient n_2 below the value n_{2K} for an artificial Kerr medium, and this will cause the critical power P_{cr} in Eq. (6.12) to be even greater than that for the artificial Kerr medium P_{crK}=0.6 W. This would seem to be a step backwards in terms of

61

improving the agreement with the experiment. However, this is not the case since this argument ignores the presence of the next order nonlinearity that is proportional to n_4.

Figure 6.5 shows the results expected from the VG model for $B_2/V_p = 10$ (blue line $P_{roll} = 0.4\ W$), $B_2/V_p = 20$ (red line $P_{roll} = 0.5\ W$), and $B_2/V_p = 30$ (green line $P_{roll} = 0.6\ W$). By using BPM we find that $P_{roll} = 0.4, 0.51, 0.62\ W$ for $B_2/V_p = 15, 25, 35$ respectively.
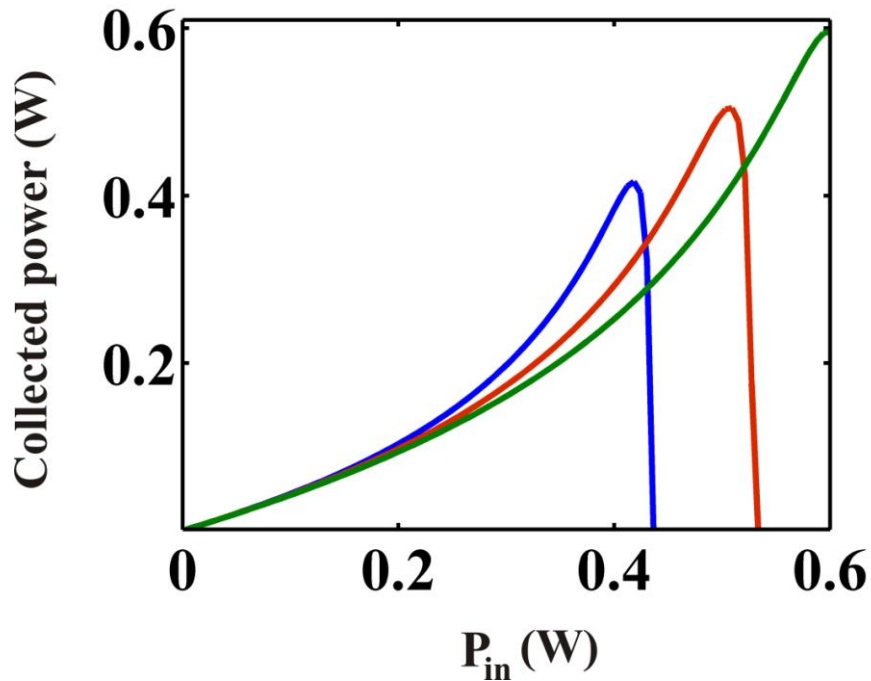
Figure 6.5 The power measured by the collecting fiber versus the input power using the non-ideal gas model and the VG. The blue line is for $B_2/V_p = 10$, the red line for $B_2/V_p = 20$, and the green line for $B_2/V_p = 30$.

The best fit to experimental data is obtained for $B_2/V_p = 20$ (solid line) where the rollover power is $0.5\,W$. In this case values for the nonlinear coefficients are given by $n_2 = 1.66 \times 10^{-9}\,cm^2/W$, $n_4 = 4.2 \times 10^{-16}\,cm^4/W^2$. This value for n_2 is in reasonable agreement with the previously quoted value $n_2 = 2 \times 10^{-9}\,cm^2/W$ measured by the Z-scan method.

It is worth noting that Junio et $al.$[12] have previously commented on the necessity of incorporating higher-order nonlinear effects to account for dipole-dipole interactions between the spheres. We would like to emphasize that in general the virial expansion can account for this type of interactions (as well as any other interactions), as long as the nature and form of interaction is known. As mentioned earlier, the non-ideal gas model expresses the compressibility of the colloidal suspension via the virial coefficients, and their inclusion softens the nonlinear optical response from the exponential nonlinearity model (see Fig.6.3). In this way the exponential model can be tamed to produce an artificial Kerr medium, but we also see the necessity of including the higher-order nonlinearity proportional to n_4 thus yielding a super-Kerr nonlinear response. A comparison with the hard sphere gas model of Matuszewski et al. [37,38] shows that for this type of interactions the value of the normalized second virial coefficient $B_2/V_p = 4$ which is too small to explain our experiment.

We finish by noting that we have used the rollover power as the fit parameter between theory and experiment, but it must be noted that there is some discrepancy between the functional form of the experimental and theoretical plots of the variation of collected

power versus input power in Figs. (6.2) and (6.4). In particular, the theoretical plots vary far more abruptly past the rollover point in comparison to the experiment. However, the shot-to-shot variations in the experimental collected power, reflected in the vertical error bars, are also greater past the rollover. The abrupt drop off past the rollover in the theory is most certainly a consequence of super-critical collapse due to the n_4 nonlinearity [40] which translates into the sensitivity to small variations in the input power in the experiment beyond the rollover making detailed comparison of theory and experiment more difficult past the rollover point.

In summary, we have introduced an optical fiber-based diagnostic experiment that can be used to probe the nonlinear optical response of a colloidal suspension and provide a test of the theoretical approaches that have been proposed. The exponential nonlinearity model was found to have the least correlation with our experiment, followed by the artificial Kerr medium approach. Including the effects of compressibility via the second virial coefficient in the non-ideal gas model was found to yield good agreement with the experiment, and in turn can be used to infer values for B_2/V_p, and the nonlinear coefficients.

CHAPTER SEVEN: SHIFTED HAMILTONIAN FORMALISM FOR THE NONLINEAR OPTICAL RESPONSE OF SOFT MATTER

7.1. Introduction

Conservation laws play an important role in classical mechanics [45] as well as nonlinear dynamics [46,47]. The existence of these conserved quantities arises from both external and internal symmetries of a system [45,48]. In nonlinear dynamics, the classification and behavior of the system depend on these constants of motion [46]. A system with a number of conserved quantities equal to (or greater than) the number of degrees of freedom is said to be integrable. Otherwise it is labeled as non-integrable. While the former behaves regularly, the latter exhibits chaotic behavior [46]. These quantities also find applications in modeling nonlinear equations. In the absence of analytical solutions it is very important to devise methods to check the validity and accuracy of numerical simulations carried out to predict the nonlinear response under certain initial conditions. In the context of nonlinear guided waves, the most commonly used conserved quantities are the power and the Hamiltonian. While the power can be conserved for many different physical realizations, the expression for the Hamiltonian, on the other hand, is unique to each nonlinear differential equation, and hence provides a means of checking numerical results. In some cases, as we will see later, it is impossible to either derive a closed form solution for the Hamiltonian or to obtain its value numerically, rendering this quantity useless for all practical purposes. Here we focus our attention on nonlinear Schrodinger-like equations [49] that play important role in optics

[50] as well as other fields such as plasma physics [29] and Bose-Einstein condensates [51]. By introducing a finite shift on the Hamiltonian density, we show that a numerical value of the new shifted Hamiltonian can be obtained and used to check the validity of the numerical analysis. Before we go into the details of our analysis, it might be first useful to describe briefly the Lagrangian and Hamiltonian formalisms of nonlinear field equations and to establish the conservation of the Hamiltonian.

7.2. Lagrangian and Hamiltonian formalism

In nonlinear dynamics as well as in classical mechanics, the system's evolution can be described using several different formalisms. The most common of these is to write a differential equation that directly represents the time (space) evolution of the field quantities. Equivalently, the same system can be described through its Lagrangian or the Hamiltonian. In this section we briefly introduce the latter two in the context of nonlinear-like Schrodinger equations [49]. Consider the optical beam evolution equation:

$$i\frac{\partial \varphi}{\partial z} + \frac{\partial^2 \varphi}{\partial x^2} + \frac{\partial^2 \varphi}{\partial y^2} + \gamma\left(|\varphi|^2\right)\varphi = 0 \qquad (7.1)$$

To develop the Lagrangian equivalence of Eq.(7.1), we start by assuming the Lagrangian density $\mathcal{L} = \mathcal{L}\left(\varphi, \varphi^*, \varphi_z, \varphi_z^*, \varphi_x, \varphi_x^*, \varphi_y, \varphi_y^*\right)$, where here $\varphi_z = \partial\varphi/\partial z$ and the same is also true for other indices x, y. In the above definition, each of the terms appearing in the argument of $\mathcal{L}$ is treated as an independent variable. Using calculus of variations, one

can show that the action, defined as $S = \int\limits_{z1}^{z2} \int\limits_{-\infty}^{\infty} \int\limits_{-\infty}^{\infty} \mathcal{L}\, dx\, dy\, dz$ is maximum/minimum when

the Lagrangian density satisfies the Euler-Lagrange equations:

$$\frac{\partial \mathcal{L}}{\partial \varphi^*} - \frac{1}{\partial z}\frac{\partial \mathcal{L}}{\partial \varphi_z^*} - \frac{1}{\partial x}\frac{\partial \mathcal{L}}{\partial \varphi_x^*} - \frac{1}{\partial y}\frac{\partial \mathcal{L}}{\partial \varphi_y^*} = 0 \qquad (7.2.a)$$

$$\frac{\partial \mathcal{L}}{\partial \varphi} - \frac{1}{\partial z}\frac{\partial \mathcal{L}}{\partial \varphi_z} - \frac{1}{\partial x}\frac{\partial \mathcal{L}}{\partial \varphi_x} - \frac{1}{\partial y}\frac{\partial \mathcal{L}}{\partial \varphi_y} = 0 \qquad (7.2.b)$$

A Lagrangian density associated with Eq.(7.1) will reduce the Euler-Lagrange equations to the beam evolution equation (Eq. (7.1)). It is clear that each different evolution equation has its unique Lagrangian density. For example, for Eq.(7.1), we find that:

$$\mathcal{L} = \frac{i}{2}\left(\varphi\varphi_z^* - \varphi^*\varphi_z\right) + |\varphi_x|^2 + |\varphi_y|^2 - G\left(|\varphi|^2\right) \qquad (7.3)$$

Where $G(I) = \int \gamma(I)\, dI$ with $I = |\varphi|^2$. Note that G in the last expression is an indefinite integral of γ and it has to be obtained analytically. This can be done easily in the case of Kerr nonlinearity and the cases of exponential and saturable nonlinearities introduced in chapters two. However for the general situation of optical beam propagation in a colloidal system of interacting nano-particles, we find that performing this integral analytically is impossible for the simple reason that the exact form of the nonlinear optical response is not known. Instead the filling factor ratio f is expressed as an implicit function of the nonlinear coefficient; hence the nonlinear response can be obtained only numerically for each value of f. It is important to note here that direct substitution of Eq.(7.3) in Eq.(7.2) yields the nonlinear propagation equation, Eq.(7.1).

The Hamiltonian density corresponding to Eq.(7.1) can be obtained directly through its Lagrangian density as

$$\mathcal{H} = \varphi_z^* \frac{\partial \mathcal{L}}{\partial \varphi_z^*} + \varphi_z \frac{\partial \mathcal{L}}{\partial \varphi_z} - \mathcal{L} = G\left(|\varphi|^2\right) - |\varphi_x|^2 - |\varphi_y|^2. \tag{7.4}$$

By defining the canonical variable $\eta = \varphi^*$ along with the associated canonical momentum $\pi = -i\varphi$ it is straight forward to show that $\partial\pi/\partial z = \delta\mathcal{H}/\delta\eta$ leads directly to Eq.(7.1). In the previous formula δ is the variational derivative. It is important to emphasize that the total Hamiltonian $H = \int \mathcal{H}\, dx\, dy$ of the system is conserved, i.e. $dH/dz = 0$. This result can be easily derived by substituting dH/dz in Eq.(7.1) and using integration by parts. As mentioned before, conserved quantities are associated with symmetry properties of the systems. For this specific case, the conservation of the Hamiltonian is a direct outcome of the invariance of the Lagrangian with respect to z. In other words there is symmetry with respect to the propagation direction (The form of the evolution equation does not depend on the propagation distance).

7.3. Shifted Hamiltonian

Here we start again with the normalized nonlinear Schrodinger equation:

$$i\frac{\partial\varphi}{\partial z} + \nabla_\perp^2 \varphi + \gamma\left(I\right)\varphi = 0 \tag{7.5}$$

Where $I = |\varphi|^2$ is the normalized intensity and $\gamma(I)$ represents the nonlinearity. For example, in the case of Kerr nonlinearity $\gamma(I) = I$. As explained before, the

corresponding Hamiltonian density in 2D takes the form $\mathcal{H} = G(I) - |\varphi_x|^2 - |\varphi_y|^2$, with

$G(I) = \int \gamma(I) dI$. As we mentioned before, this integral is indefinite and can be obtained

only analytically if the form of $\gamma(I)$ is explicitly known. Under Kerr nonlinear

conditions, the integration takes the form $G(I) = I^2/2$. In the case of optical beam

propagation in ideal nano-suspensions where $\gamma(I) = \exp(I)$ we find that $G(I) = \exp(I)$.

However, when the many-body effects are taken into consideration, the nonlinearity can

not be expressed as an explicit function of the intensity. In this latter case, the evolution

equation takes the form:

$$i\frac{\partial \varphi}{\partial z} + \nabla_\perp^2 \varphi + \gamma(I)\varphi = 0 \qquad (7.6.a)$$

$$I = \ln(\gamma) + A_1(\gamma - 1) + A_2(\gamma^2 - 1) \qquad (7.6.b)$$

In Eq.(7.6.b) A_1 and A_2 are constants that depend on the system parameters. It is clear,

from Eq.(7.6.b), that γ can not be solved and written as an explicit function of I and thus

it is not possible to obtain the function $G(I) = \int \gamma(I) dI$. As a result the Hamiltonian

density and hence the total Hamiltonian can not be calculated. Consequently the

conservation of the Hamiltonian can not be used anymore in order to check the accuracy

of the numerical simulation. In order to overcome this obstacle we introduce a shifted

Hamiltonian density of the form:

$$\mathcal{H}' = G(I) - G(0) - |\varphi_x|^2 - |\varphi_y|^2 \ . \qquad (7.7)$$

Where in Eq. (7.7) $G(0)$ is a constant representing the value of $G(I)$ at $I=0$. This is

equivalent to $G(I) = \int_0^I \gamma(I') dI'$. Note that the addition of this constant will cause the

total Hamiltonian to diverge, i.e. $H' = \int_{-\infty}^{\infty} \int_{-\infty}^{\infty} \mathcal{H}' dx dy = \infty$. However in modeling

nonlinear beam propagations, for localized initial conditions, the field decays fast and for

all practical purposes the simulation window is always kept finite. Under these conditions

the numerical value of the shifted Hamiltonian will be shifted by a constant C

above/below the actual value of the Hamiltonian, namely $H' = \int_{y_0}^{y_f} \int_{x_0}^{x_f} \mathcal{H}' dx dy \approx H + C$,

where C is a constant and $C = G(0)W$ with W being the area (or width) of the

simulation window. Note that $dH'/dz \approx dH/dz + dC/dz = dH/dz = 0$. This last formula

is an expression of the conservation of the shifted Hamiltonian and can be used to check

the accuracy of the numerical integration of the optical beam evolution. First we examine

the 1D situation and we and show how to calculate the shifted Hamiltonian in one

dimension. Before we proceed, we stress that the simulation domain is always chosen

such that the field values practically vanish at the boundaries. Assume that at any step,

the field takes the form $\varphi = \varphi(x)$, it follows that the intensity can be also written as

$I = |\varphi(x)|^2 = K(x)$ and hence $\gamma(I) = \gamma(I(x)) = \gamma(K(x)) = h(x)$, where $K(x)$ and

$h(x)$ are two functions of the transverse coordinate x. Note that these two functions are

readily obtained at each point z along the propagation direction by directly integrating of

the evolution equation under the given initial conditions (using beam propagation

techniques for example). Next we define the integral $J_i = \int_{I_0}^{I_i} \gamma(I) dI$ where I_0 is the

intensity at point x_0, the most left boundary point of the numerical window where the

value of I_0 is always zero during the evolution of the initial data. On the other hand, I_i

represents the intensity at an intermediate point x_i along the transverse direction. Note that

$dI = (\partial K / \partial x) dx$ and thus the integration can be written as $J_i = \int_{x_0}^{x_i} h(x)(\partial K(x)/\partial x) dx$.

From the numerical values of both functions $K(x)$ and $h(x)$, J_i can be calculated and its

numerical value can be easily obtained for any point x_i. But this same integration yields

$J_i = \int_{I_0}^{I_i} \gamma(I) dI = G(I_i) - G(I_0) = G(I_i) - G(0)$, since I_0 is zero at the boundaries. This

leads to the result:

$$G(I_i) - G(0) = \int_{x_0}^{x_i} h(x)(\partial K(x)/\partial x) dx \qquad . \ (7.8)$$

The shifted Hamiltonian density is then obtained by substituting Eq.(7.8) into Eq.(7.7).

Since the value of $|\varphi_x|^2$ can be also computed numerically, it immediately follows that

the numerical value of the shifted Hamiltonian density can be calculated at any point x_i.

It is now straightforward to carry out the integration $H' = \int_{x_0}^{x_f} \mathcal{H}' dx$ to find the numerical

value of the total shifted Hamiltonian. These steps can be repeated at each propagation

distance z and the conservation of H' can be checked.

This result can be generalized to 2D geometries where now $I = K(x, y)$ and $\gamma(I) = \gamma(I(x, y)) = \gamma(K(x, y)) = h(x, y)$. As before, we define the integral

$J_{ij} = \int_{I_{00}}^{I_{ij}} \gamma(I) dI$ where I_{ij} is the intensity at point (x_i, y_j). In this case we have

$dI = (\partial K / \partial x) dx + (\partial K / \partial y) dy$ and the integration becomes a line integral on a contour Γ,

i.e. $J_{ij} = \int_{\Gamma} h(x, y) \left[(\partial K(x, y) / \partial x) dx + (\partial K(x, y) / \partial y) dy \right]$. Since J_{ij} depends only on the

values of the intensity at the boundaries $0(I_{00}$ and $I_{ij})$, it directly follows that that integration

in the last equation is contour independent and one is in fact free to choose the contour

that facilitates the numerical calculation. The most straight forward choice is the one

shown in Fig.7.1 where the integration is first performed along x with y being constant

and then along y with x kept constant. By doing so, J_{ij} can be expressed as:

$$J_{ij} = \int_{x_0}^{x_i} h(x, y_0)\left(\partial K(x, y_0) / \partial x\right) dx + \int_{y_0}^{y_f} h(x_i, y)\left(\partial K(x_i, y) / \partial y\right) dy \qquad (7.9)$$

Finally, similar to the 1D situation, we find that:

$$G(I_{ij}) - G(0) == \int_{x_0}^{x_i} h(x, y_0)\left(\partial K(x, y_0) / \partial x\right) dx + \int_{y_0}^{y_f} h(x_i, y)\left(\partial K(x_i, y) / \partial y\right) dy \qquad (7.10)$$

The shifted Hamiltonian density is then found through Eq. (7.7) and the total shifted

Hamiltonian is found using $H' = \int_{y_0}^{y_f} \int_{x_0}^{x_f} \mathcal{H}' dx \, dy$.

In order to verify these results, a numerical integration was performed for Eqs.(7.6.a) and (7.6.b) for the same parameters as in chapter 5. In both one and two dimensions the shifted Hamiltonian was conserved up to the fourth digit.
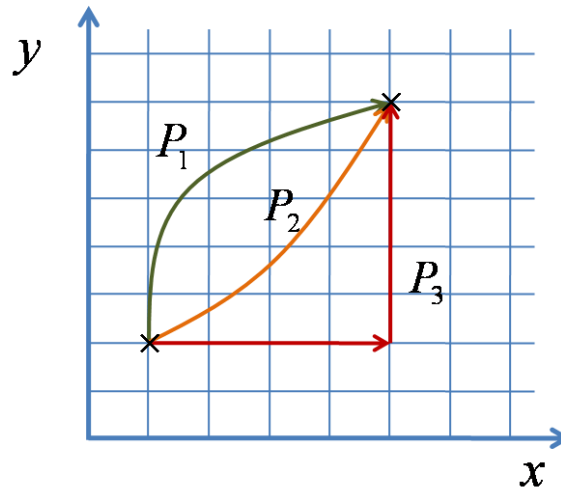
Figure 7.1 Different possible paths of integration with P_3 being the preferred one for numerical calculations

In conclusion, we have introduced the concept of shifted Hamiltonian density. We showed that it is a constant of motion and that it has a finite numerical value for finite modeling domain. A systematic method was described to obtain the value of the Shifted Hamiltonian in both 1D and 2D geometries. While the problem reduces to simple integral in the 1D case, it was shown that in the 2D situation, the final result can be expressed as a contour integral. The simplest possible contour was identified and the results were verified numerically.

CHAPTER EIGHT: SOLITONS IN DISPERSION-INVERTED *AlGaAs* NANOWIRES

8.1. Introduction

The interaction of light with matter on a nanometer scale opens up new opportunities which may have far reaching implications in telecommunications, computation, biophotonics, and sensing technologies [52]. Lately, single-mode sub-wavelength waveguides or nanowires have been realized in several material systems [53-62]. Such optical nanowire structures are capable of providing superior light confinement and are thus ideal for nonlinear optics applications [63]. Clearly, of interest will be to fabricate such nanowires using high contrast, highly nonlinear materials, such as *AlGaAs*-known to exhibit a nonlinearity that is three orders of magnitude higher than that of silica glass [64,65]. Apart from being highly nonlinear, *AlGaAs* nanowires are also highly promising in terms of applications since they can be integrated with other optoelectronic components on the same wafer and thus can serve as information conduits among miniaturized devices. Quite recently, enhanced spectral broadening or SPM has been observed for the first time in *700μm* long *AlGaAs* nanowires [66]. An important question associated with this particular system is whether optical solitons are possible in *AlGaAs* nanowaveguides. This is of relevance since solitons can be used to either overcome dispersion effects or to achieve pulse compression in such nanostructures. We note that so far, optical solitons have only been observed in multi-layer *AlGaAs* structures in which the dispersion can be engineered [67,68]. Yet, in primitive weakly guiding *AlGaAs* waveguides

such solutions are not possible since this material system exhibits appreciable normal dispersion in the spectral region of interest [69], i.e. for $1.1\mu m < \lambda < 1.7\mu m$. Here we theoretically demonstrate, that, because of high contrast, the dispersion of an air-clad *AlGaAs* nanowire can become strongly anomalous (becomes inverted), thus overcoming material dispersion limitations. This in turn may allow optical soliton formation in millimeter long structures. These solitons are possible at very low power levels (at ~5 W) in spite of the fact that the *AlGaAs* nanowires can exhibit anomalous dispersion that is a thousand times higher than that of silica glass. The intensity and spectral evolution of these solitons is investigated in *AlGaAs* nanowaveguides in the presence of loss, multi-photon absorption, and higher-order dispersive and nonlinear effects.

8.2. *AlGaAs* nanowire dispersion properties

To analyze the dispersion properties of *AlGaAs* nanowires, let us consider for example an $Al_{0.2}Ga_{0.8}As$ nanorod of core radius a as shown in Fig.8.1(a). This particular composition ($Al_{0.2}Ga_{0.8}As$) is deliberately chosen since in the neighborhood of $\lambda = 1.55\mu m$ it is known to exhibit relatively low two-photon absorption [70]. In addition, we assume that the nanowire is air-cladded. We note that even though completely air-clad structures are rather difficult to develop these days, it is yet possible to fabricate waveguides that are mostly surrounded by air, with characteristics very similar to the one analyzed here. At this wavelength the refractive index of $Al_{0.2}Ga_{0.8}As$ is approximately 3.27, and the nanorod is operated at or close to the single-mode regime. In general, the nanowire dispersion relation is given by [71]:

$$\left[\frac{J'_m(u)}{uJ_m(u)}+\frac{K'_m(w)}{wK_m(w)}\right]\left[\frac{J'_m(u)}{uJ_m(u)}+\left(\frac{n_{clad}}{n_{core}}\right)^2\frac{K'_m(w)}{wK_m(w)}\right]=m^2\left(\frac{1}{u^2}+\frac{1}{w^2}\right)\left(\frac{1}{u^2}+\left(\frac{n_{clad}}{n_{core}}\right)^2\frac{1}{w^2}\right) \qquad . (8.1)$$

In Eq.(8.1) $J_m(u)$ is a Bessel function of the first kind and of order m and similarly $K_m(w)$ is a modified Bessel function, and primes represent derivatives with respect to the argument. $u=ak_o\sqrt{n_{core}^2-n_{eff}^2}$, $w=ak_o\sqrt{n_{eff}^2-n_{clad}^2}$ where $k_0=2\pi/\lambda$ is the free space wavevector and n_{eff} is the effective refractive index of the mode [71]. n_{core} is the core index and $n_{clad}=1$ since the exterior medium is air. The wavelength dependence of the refractive index is accounted by using the Sellmeier expansion of $Al_xGa_{1-x}As$, i.e [69]:

$$n_{core}^2(x,T,\lambda)=A(x,T)+\frac{C_o(x)}{E_o^2(x,T)-1/\lambda^2}+\frac{C_1(x)}{E_1^2(x,T)-1/\lambda^2} \qquad . (8.2)$$

In general, the constants A, C_0, C_1, E_0 and E_1 depend on the Al composition (x), the temperature T, and the free space wavelength λ. Here all calculations were carried out at room temperature.

The dispersion properties of the fundamental mode HE_{11} of such a nano-structure are obtained by numerically solving Eq. (8.1) for $m=1$, with the core index evaluated at each frequency step from Eq. (8.2). The dispersion coefficient $\beta''=d^2\beta/d\omega^2$ of an $Al_{0.2}Ga_{0.8}As$ nanowire is shown in Fig.8.1(b) in units of ps^2/m for different core radii. In this same figure, the bulk $Al_{0.2}Ga_{0.8}As$ dispersion is also included for comparison.
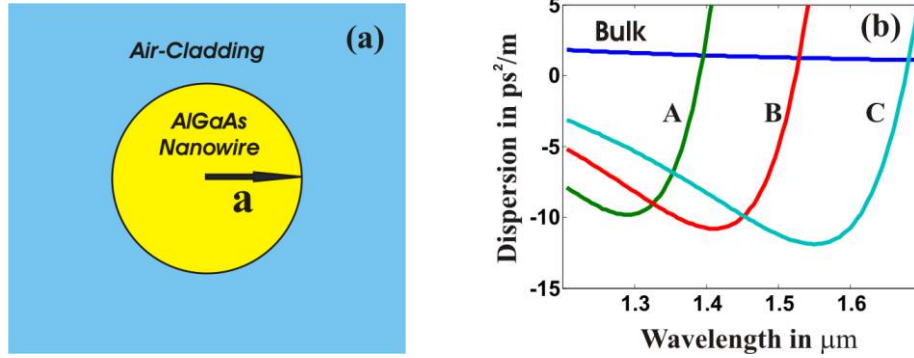
Figure 8.1 (a) a nanowire structure; (b) group velocity dispersion $\beta^{"}$ of an $Al_{0.2}Ga_{0.8}As$ nanowire when its radius is (A) 160, (B) 175 and (C) 193 *nm*. Bulk dispersion of $Al_{0.2}Ga_{0.8}As$ is also shown.

It is important to note that because of the strong index contrast of the *AlGaAs* nanowaveguide and the resulting field confinement, the waveguide dispersion dominates and as a result the dispersion can become inverted and strongly anomalous [55,72]. In fact for $a=193nm$, the dispersion of such a nanorod can reach very high values, as high as $-12ps^2/m$, which is 10^3 times higher than that of a standard silica fiber at 1.55 μm.

Parenthetically, we would like to point out that these same structures can also lead to very high normal dispersion. Figure 8.2(a) depicts the total dispersion of an $Al_{0.2}Ga_{0.8}As$ nanorod when its radius is $a=160nm$. As one can see, the anomalous dispersion of this structure (also shown in Fig.8.1(b) for $\lambda \leq 1.4\mu m$) is followed by a region of strong normal dispersion especially at 1.55 μm. In fact around 1.55 μm the dispersion is approximately $\beta^{"}=80ps^2/m$. Thus the dispersion of a $2cm$ long *AlGaAs* nanorod will be sufficient to cancel that arising from a $1.25km$ long anomalously dispersive fiber with group velocity dispersion $D=1ps/km.nm$. In addition Fig.8.2(b) shows the group index

77

$n_g = c/\upsilon_g$ and the effective index n_{eff} of an $Al_{0.2}Ga_{0.8}As$ nanowire of radius $a = 175nm$ as a function of wavelength. Note that the group index in this case can be as high as $n_g \approx 5.52$ around 1.55 μm, which indicates "slow" light transport (because of waveguide dispersion) in spite of the fact that bulk index is 3.27 and $n_{eff} = 1.56$.
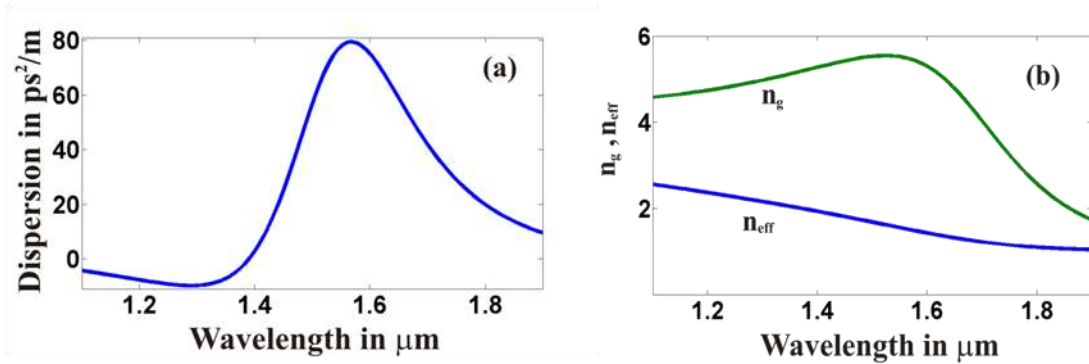
Figure 8.2 (a) group velocity dispersion β'' when $a = 160nm$, (b) group and effective refractive indices of an $Al_{0.2}Ga_{0.8}As$ nanowire when $a = 175nm$.

For the subsequent discussion, we chose two operating points based on the designs (C) and (B) shown in Fig.8.1(b). In particular the design (C) is used at 1.55 μm where the third-order dispersion is very small whereas design (B) is used at 1.5 μm where cubic dispersive effects become appreciable. The nanowire of case (C) is single-moded for $\lambda \geq 1.57\mu m$ whereas that of (B) is monomode for $\lambda \geq 1.42\mu m$.

8.3. Soliton effects in AlGaAs nanowires

Nonlinear pulse propagation in such nanowire structures is modeled using the evolution equation [73]:

$$i\frac{\partial\varphi}{\partial z}+i\alpha\varphi+\sum_{m=2}^{\infty}\frac{i^m\beta^{(m)}}{m!}\frac{\partial^m\varphi}{\partial T^m}+\frac{\omega_o n_2}{2c}\left[|\varphi|^2\varphi+\frac{i}{\omega_o}\frac{\partial\left(|\varphi|^2\varphi\right)}{\partial T}\right]+i\alpha_2|\varphi|^2\varphi+i\alpha_3|\varphi|^4\varphi=0 \qquad . \quad (8.3)$$

In Eq.(8.3), φ represents the pulse envelope, $T=t-z/\upsilon_g$, α is the linear loss coefficient, $\beta^{(m)}=\partial^m\beta/\partial\omega^m$ is the mth order dispersion coefficient evaluated at the carrier angular frequency $\omega_0=2\pi c/\lambda$, $n_2=(\hat{n}_2 n)/(2\eta_o)$ where $\hat{n}_2=1.3\times10^{-13}cm^2/W$ is the nonlinear Kerr coefficient and n is the linear refractive index of *AlGaAs* (η_o is the free space wave impedance). $\alpha_2=6.5\times10^{-15}m/V^2$ and $\alpha_3=5.63\times10^{-31}m^3/V^4$ are the two-photon and three-photon absorption coefficients respectively at $\lambda\approx1.55\mu m$ [70]. In all cases, the dispersion curve is incorporated in Eq.(8.3) using a dispersion Taylor series over a broad spectral range (greatly exceeding the pulse spectrum). Here the linear loss for the field is taken to be $\alpha=.25cm^{-1}$.

Figure 8.3(a) shows the intensity evolution of a $200fs$ (FWHM) hyperbolic secant optical pulse when is launched into a $5mm$ long $Al_{0.2}Ga_{0.8}As$ nanowire of core radius $a=193nm$ (corresponding to curve (C) of Fig.8.1(b)) at $1.55\mu m$. For this design, the quadratic dispersion ($\beta''=-12ps^2/m$) dominates the propagation process (the higher-order dispersion terms are negligible) and the dispersion length is $\approx1.5mm$, i.e., is very small. The pulse peak power in this case is approximately $5.5W$ (with a 75% confinement factor), corresponding to the fundamental soliton in this nanowire structure.

As Fig.8.3(a) clearly indicates, this soliton can be sustained over approximately 3-4 dispersion lengths, i.e. up to a distance that is ultimately determined by the linear loss of

the system. Fig.8.3(b) on the other hand depicts soliton compression under similar conditions when the input power of the pulse is 8 W.
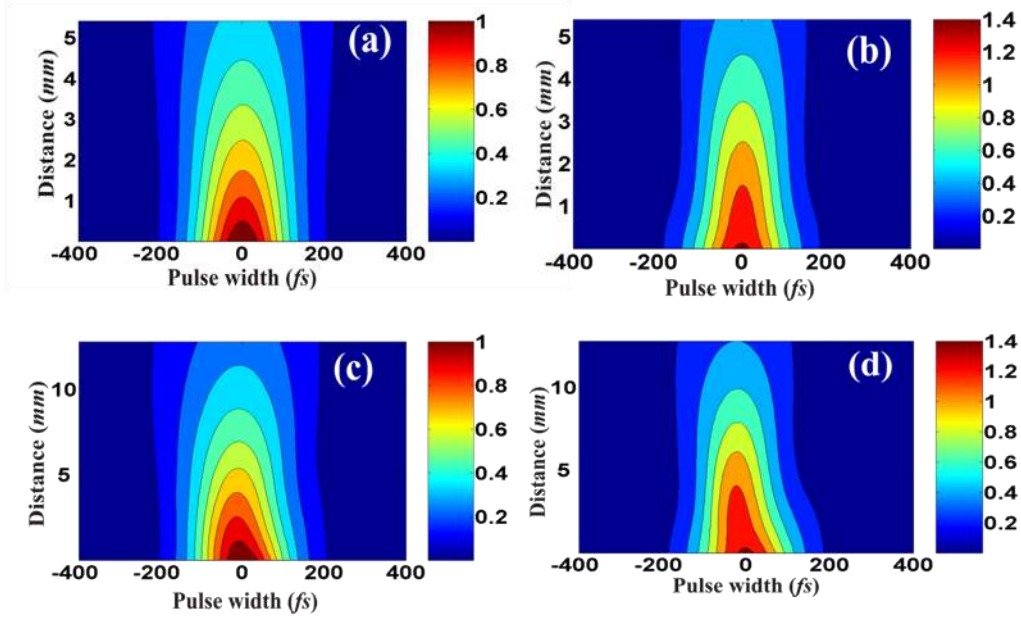
Figure 8.3 Intensity evolution of a *200 fs* soliton propagating in a 193 *nm* (radius) *AlGaAs* nanowire when the peak power is (a) 5.5 and (b) 8 *W*. Similarly, (c) and (d) depict soliton propagation and compression in a nanowire of radius 175 *nm* when the peak power is 2 and 2.8 *W* respectively.

For this power level, at 2 dispersion lengths, the FWHM pulsewidth becomes $175 fs$. Figures 8.3(c) and (d) demonstrate similar results when an *AlGaAs* nanowire corresponding to curve (B) of Fig.8.1(b), is used at $1.5 \mu m$. Even in this case, in spite of appreciable third-order dispersion effects and multi-photon absorption, a $200 fs$ soliton forms at $2 W$, as shown in Fig.8.3(c). Soliton compression is also shown for this case in Fig.8.3(d) when the input power is $2.8 W$. It is important to note that in all cases

ultrashort solitons in these nanowires can form within millimeters and at very low power levels.
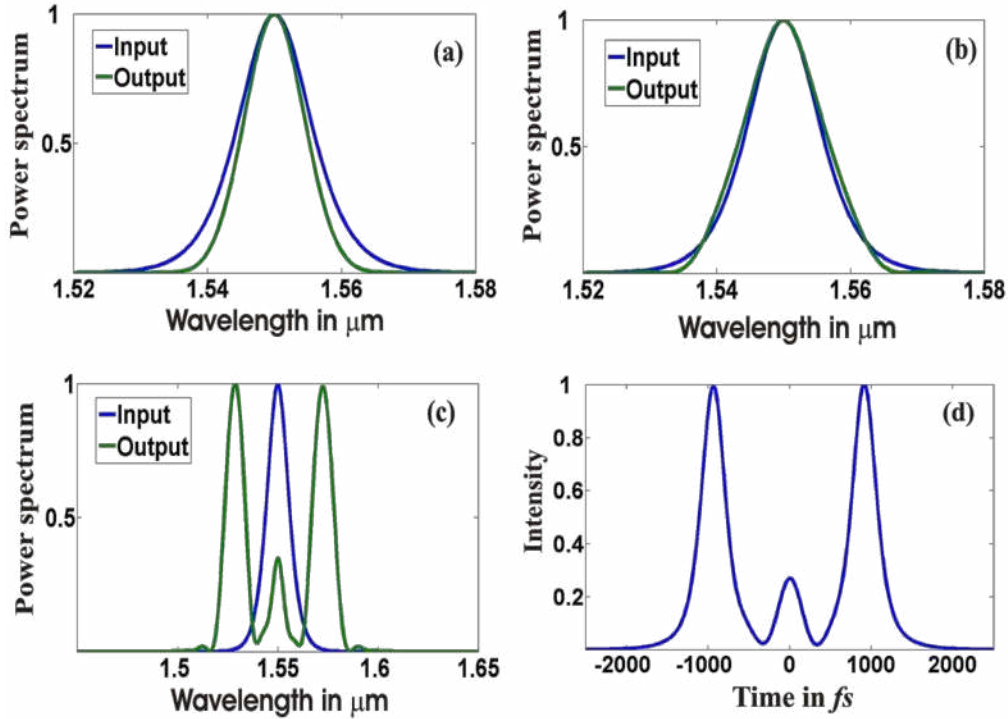
Figure 8.4 (a) Input and output soliton power spectra corresponding to the case shown in (a) Fig.8.3 (a) ; (b) Fig.8.3 (b) ; (c) and (d) spectral generation and intensity profile for an $N = 3$ soliton (50 W peak power) at $L \approx 5mm$.

Figure 8.4 depicts the power spectra that may result in an $Al_{0.2}Ga_{0.8}As$ nanowaveguide of radius $a = 193nm$ when is excited at $1.55\mu m$ with a *200fs* FWHM optical pulse. When the input peak power is enough to establish an optical soliton (*5.5 W*) the power spectrum remains essentially invariant during propagation as shown in Fig. 8.4(a). At a higher power (8*W*) the pulse undergoes compressions and thus its spectrum broadens (Fig. 8.4(b)). Figures 8.4(c) and (d) on the other hand depict the

expected spectra and intensity profile of a higher order soliton at $L \approx 5\,mm$. In this latter case, the peak power is 50 W and thus corresponds to an $N = 3$ higher order soliton solution. The splitting behavior observed in Fig. 8.4(d) is attributed to multi-photon absorption.

In conclusion we have shown that optical solitons can exist in dispersion-inverted highly-nonlinear $AlGaAs$ nanowires. These soliton waves are possible at very low power levels in spite of strong dispersion and can form in millimeter long nanowire structures. The intensity and spectral evolution of solitons propagating in such $AlGaAs$ nanowaveguides was investigated in the presence of loss, multiphoton absorption and higher-order dispersion.

CHAPTER NINE: POWER CIRCULATION VIA NEGATIVE ENERGY-FLUX WORMHOLES IN OPTICAL NANOWAVEGUIDES

9.1. Introduction

Controlling the flow of light on a nanometer scale may have important implications in both science and technology [52]. Progress in the area of nano-photonics is expected to impact communication and computing technologies as well as bio-photonics. In the last few years we have witnessed rapid advances in the fields of near-field microscopy and spectroscopy and sub-wavelength imaging [74]. The fabrication of high contrast dielectric nanowaveguides is yet another important development in this area. Because of their strong index contrast, these sub-wavelength waveguides or nanowires can exhibit considerably altered dispersion characteristics and enhanced nonlinearity [53-56]. When implemented with semiconductor materials such as *GaAs* or *AlGaAs*, these nano-waveguides show promise for efficient second harmonic generation and self-phase modulation at very low optical powers [66,75,76].

In the last few decades or so, the electromagnetic problem associated with wave propagation in cylindrical dielectric waveguides has been intensely investigated in a number of studies [77-79]. Given the history of this topic, at a first glance it may seem that all is known regarding the guiding behavior of these structures. An unusual effect associated with the electromagnetic properties of the fundamental HE_{11} mode in high-contrast dielectric rods was theoretically found by Gillespie in 1960 [80]. This effect, which has so far received little if any attention, arises from the fact that in such high-

contrast structures there can be two regions (close to the core-cladding boundary) where the Poynting vector is negative with respect to the direction of propagation. We emphasize that in all cases (for lossless fibers), the phase velocity and group velocity vectors of the HE_{11} mode are parallel, i.e. the negative power never exceeds the positive power and thus no backward waves are associated with the presence of these regions [80]. An important facet of this intriguing effect that still remains unresolved arises when one examines the energy balance equation of the HE_{11} mode during pulse propagation, e.g. by considering [81]

$$\oiint_A \vec{S} \cdot d\vec{a} = -\frac{\partial W}{\partial t} \qquad (9.1)$$

over a virtual volume V (surrounded by a surface A) that is totally embedded in one of these regions. In Eq.(9.1), $\vec{S}$ is the energy flux or Poynting vector, and W is the total electromagnetic energy in the volume V. More specifically, if a pulse first excites the front face of the virtual surface enclosing this volume (where the energy flux is negative), then how is the escaping energy balanced in this region? To address this issue we will investigate the behavior of this system in the time domain.

Here we show, that in high-contrast dielectric optical nanowires, power circulation is possible during pulse propagation via negative energy-flux wormholes. This phenomenon is in fact universal since it occurs in a variety of waveguide geometries as long as the waveguide index-contrast exceeds a critical value. For demonstration purposes this mechanism is examined in circular *AlGaAs* and silicon nanowaveguides. We theoretically demonstrate that under pulse conditions these wormholes are constantly

exchanging energy with their surroundings and at "infinity" (with respect to the pulse center) they become strongly warped-in a way similar to that expected in negative-index waveguides. For completeness dispersion effects are also accounted in our analysis and pertinent examples are provided. Methods to detect the presence of these negative energy-flux regions or wormholes are also suggested.

9.2. Analysis

To demonstrate our results we consider wave propagation in a cylindrical optical nanowire of core radius a. This dielectric rod is surrounded by air/vacuum and its refractive index is taken here to be n. The vacuum wavelength of the optical wave exciting this nano-waveguide is λ_0. In this case, the electromagnetic field associated with fundamental HE_{11} mode of this cylindrical structure is given by [71]

$$\vec{E} = \vec{e}(r,\theta)\exp[i(\omega t - \beta z)] \qquad (9.2a)$$

$$\vec{H} = \vec{h}(r,\theta)\exp[i(\omega t - \beta z)] \qquad (9.2b)$$

where its propagation constant β can be obtained from the first root of the corresponding eigenvalue equation. In this study, without any loss of generality, the fields of Eq.(9.2) were judiciously chosen so as the transverse electric field of the of the fundamental mode is primarily x-polarized (HE_{11}^x) [71]. As usual the transverse components ($e_r, e_\theta, h_r, h_\theta$) of the hybrid HE_{11} field can be directly derived from the longitudinal vectors. Here, the longitudinal electric fields are taken to be: $e_z = AJ_1(ur/a)\cos(\theta)$, $e_z = BK_1(wr/a)\cos(\theta)$ in the core and cladding regions respectively. Similarly, the

magnetic fields are given by: $h_z = CJ_1(ur/a)\sin(\theta)$ and $h_z = DK_1(wr/a)\sin(\theta)$, where *A,B,C,D, u*, and *w,* are all frequency dependent quantities [71]. The time-averaged Poynting vector can then be obtained from $\vec{S} = (1/2)\mathrm{Re}(\vec{E} \times \vec{H}^*)$ which under continuous-wave (CW) conditions has only a $\hat{z}$-component, i.e., is parallel to the direction of propagation.

As an example, Fig. 9.1(a) shows the distribution of the Poynting vector S_z (of the HE_{11}^x mode) over the entire transverse plane (core and cladding regions) of an $Al_{0.2}Ga_{0.8}As$ nanowire when its radius is $a = 170nm$. The $Al_{0.2}Ga_{0.8}As$ refractive index is $n = 3.25$ and the operating wavelength was assumed to be $\lambda_0 = 1.5\mu m$. Figure 9.1(b) clearly shows that in this case the intensity distribution in this nanowaveguide is elliptical-like (with an aspect ratio of 80 %).
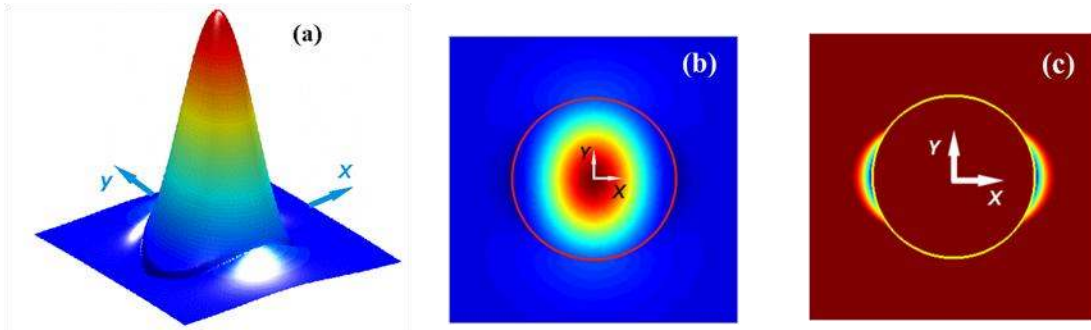
Figure 9.1 (a) Distribution of the HE_{11}^x Poynting vector S_z associated with an $Al_{0.2}Ga_{0.8}As$ nanowire of core radius $a = 170nm$. (b) Top view shows the ellipticity of the S_z distribution. (c) Negative S_z regions with the positive part removed for illustration purposes.

More importantly, at the core-air interface (around the x-axis or $\theta = 0$) there are two regions or wormholes where the energy flux density or Poynting vector becomes negative. What is quite interesting, is that, this effect results and coexists with the process of total internal reflection (TIR) which is responsible for the existence of the guided mode. These two areas have a crescent-like shape as shown in Fig. 9.1(c).

In general, these negative S_z features arise from the severe disruption of the electromagnetic field lines at the core-cladding interface and are only possible in high-index-contrast structures. It is worth noting that this effect does not occur for TE and TM modes since in these cases one can directly show that S_z is everywhere positive.
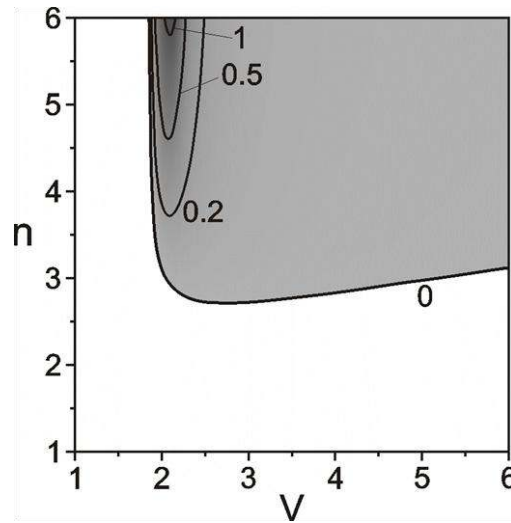
Figure 9.2 Iso-contour lines $\left| S^-_{z-max} / S^+_{z-max} \right|$ associated with the HE_{11} mode in an air-clad nanowire, as a function of index contrast and the V number.

Figure 9.2 shows the contour lines of $\left|S^{-}_{z-\max} / S^{+}_{z-\max}\right|$ associated with the HE_{11} mode in such a nanowire structure, as a function of index contrast and the *V*-number, where $V = (2\pi a / \lambda_0)\sqrt{n^2 - 1}$ [71].

As this latter figure indicates, these wormholes start to appear only when the core index exceeds the critical value of $n \geq 2.71$. Thus these effects can take place in low-loss high-index materials such as for example *GaAs, AlGaAs*, or *Si*. For the $Al_{0.2}Ga_{0.8}As$ nanorod assumed here, these regions exist in the range $1.97 \leq V \leq 6.88$ (i.e. in both the single-and multi-mode regime) and its maximum $\left|S^{-}_{z-\max} / S^{+}_{z-\max}\right|$ ratio is around *10%* at *V=2.2*. Figure 9.2 also indicates that these effects can become considerably more pronounced at higher index contrasts. This may be more relevant in the microwave region where materials with very high refractive indices of $n \approx 8 - 10$ are known to exist [82].

We emphasize that these negative energy flux regions occur in a universal fashion, e.g. they are not uniquely associated with cylindrical waveguides. Figure 9.3 depicts the electric field distributions as well as the negative Poynting vector regions as obtained using finite element methods for three different waveguide geometries when $\lambda_0 = 1.55\mu m$. In all cases the structures are air-clad and are assumed to be made out of silicon (refractive index of Si is $n = 3.5$).

Note that these wormhole domains are always enhanced around edges and regions of high geometrical curvature. Thus these effects are a byproduct of high-index contrast and geometrical effects, around which the electromagnetic field lines are severely distorted.
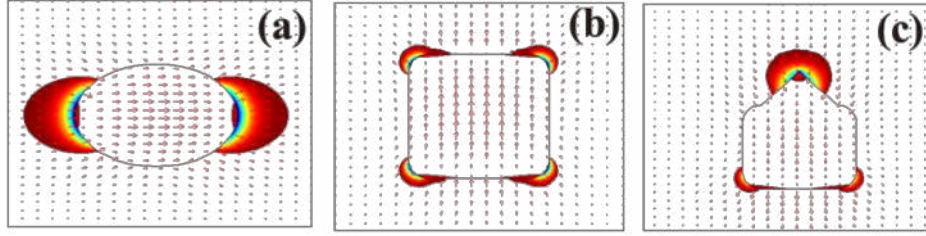
Figure 9.3 Electric field and negative Poynting vector distributions in an (a) elliptical waveguide with aspect ratio $400 \times 350 nm^2$ (b) square waveguide $350 \times 350 nm^2$ and (c) "pyramid" waveguide of approximate dimensions $300 \times 350 nm^2$

9.3. Results and discussion

Even though the CW analysis indicates that such negative energy flux regions are possible in high-index optical material systems the question remains how these wormholes get established in the first place and how is their presence consistent with the energy considerations of Eq.(9.1). To address these issues we will examine this problem in the time domain. To do so we express both the electric and magnetic field vectors through a Fourier superposition, i.e.,

$$\begin{Bmatrix} \vec{E} \\ \vec{H} \end{Bmatrix} = \frac{e^{i(\omega_0 t - \beta_0 z)}}{2\pi} \int_{-\infty}^{\infty} d\Omega \Phi_0(\Omega) \, e^{i(\Omega T - F(\Omega)z)} \begin{Bmatrix} \vec{e}(\vec{r}_\perp, \omega_0 + \Omega) \\ \vec{h}(\vec{r}_\perp, \omega_0 + \Omega) \end{Bmatrix} \quad (9.3)$$

where ω_0 is the carrier angular frequency of the wavepacket and β_0 is the corresponding propagation constant of the HE_{11} mode. $T = t - z/\upsilon_g$ is a time coordinate frame moving at the group velocity υ_g of the pulse, $\Phi_0(\Omega)$ is the pulse envelope frequency spectrum, Ω is a frequency deviation from ω_0, and the dispersion function is defined as

$F(\Omega) = \beta(\omega_0 + \Omega) - \beta_0 - (\Omega/\upsilon_g)$. By employing a first-order Taylor series expansion of the vector fields around ω_0, i.e., $\vec{e}(\vec{r}_\perp, \omega_0 + \Omega) = \vec{e}_0(\vec{r}_\perp) + \vec{e}_1(\vec{r}_\perp)\Omega$ where $\vec{e}_1(\vec{r}_\perp) = d\vec{e}/d\omega$ evaluated at ω_0, and similarly for the magnetic field $\vec{h}$, Eq. (9.3) takes the form

$$\begin{bmatrix} \vec{E} \\ \vec{H} \end{bmatrix} = \begin{bmatrix} \vec{e}_0 & -i\vec{e}_1 \\ \vec{h}_0 & -i\vec{h}_1 \end{bmatrix} \begin{bmatrix} \phi \\ \partial\phi/\partial T \end{bmatrix} \exp[i(\omega_0 t - \beta_0 z)] \qquad (9.4) \ .$$

In Eq.(9.4), $\phi(z,T)$ represents the envelope of the pulse which is given by $\phi(z,T) = (1/2\pi)\int d\Omega \Phi_0(\Omega)\exp[i(\Omega T - zF(\Omega))]$. In addition, one can formally show that even under dynamic conditions the average power flow density is still given by $\vec{S} = (1/2)\mathrm{Re}(\vec{E} \times \vec{H}^*)$. This is true because, under typical pulsed conditions, the time-averaged part $(1/2)\mathrm{Re}(\vec{E} \times \vec{H})$ of the Poynting vector is zero as the spectral functions $\Phi_0(\omega - \omega_0)$ and $\Phi_0(-\omega - \omega_0)$ have no overlap. In this case,

$$\vec{S} = \frac{1}{2}\mathrm{Re}\left\{ A^2(\vec{e}_0 \times \vec{h}_0^*) + A^2 \frac{\partial\psi}{\partial T}\left(\vec{e}_1 \times \vec{h}_0^* + \vec{e}_0 \times \vec{h}_1^*\right) + \frac{i}{2}\frac{\partial A^2}{\partial T}\left(\vec{e}_0 \times \vec{h}_1^* - \vec{e}_1 \times \vec{h}_0^*\right) \right\}, \qquad (9.5)$$

where in Eq.(9.5) the envelope was expressed in polar form, e.g. $\phi = A\exp(i\psi)$. Let us now analyze this latter result. The first term in the bracket corresponds to a modulated $\hat{z}$ power flow (CW-like part). The second term in Eq.(9.5) describes an energy redistribution among spectral frequency components (different frequencies see a different HE_{11} distribution). From the fact that $\mathrm{Re}\left\{\vec{e}(\omega_0 + \Omega) \times \vec{h}^*(\omega_0 + \Omega)\right\} \times \hat{z} = 0$, one can then deduce that the energy redistribution associated with the $\mathrm{Re}\left(\vec{e}_1 \times \vec{h}_0^* + \vec{e}_0 \times \vec{h}_1^*\right)$ term occurs again only in the $\hat{z}$ direction. The last term on

the other hand gives the *transverse* Poynting vector and is in fact responsible for establishing the wormhole regions. It is important to note that since $\int dT (A^2)_T = 0$ (for a finite energy pulse), the time-integrated Poynting vector $\int dT \, \vec{S}$ of Eq.(9.5) exhibits only a $\hat{z}$ component, in agreement with Parseval's energy theorem. If we assume that initially the envelope is Gaussian, that is $\phi(z = 0, T) = E_0 \exp(-T^2 / \tau_0^2)$ and by considering only second-order dispersion effects ($F(\Omega) = \beta_0'' \Omega^2 / 2$), then the evolution of the envelope in Eq.(9.5) can be analytically determined. In this latter case, $\vec{S}$ is given by

$$\vec{S} = \frac{|E_0|^2}{2\sqrt{1 + (z/z_d)^2}} \exp\left(-\frac{2 \ \tau^2}{1 + (z/z_d)^2}\right).$$ (9.6)

$$\mathrm{Re}\left\{\left(\vec{e}_0 \times \vec{h}_0^*\right) + \frac{2 \ (\tau/\tau_0) \ (z/z_d)}{1 + (z/z_d)^2}\left(\vec{e}_1 \times \vec{h}_0^* + \vec{e}_0 \times \vec{h}_1^*\right) - \frac{2 \ i \ (\tau/\tau_0)}{1 + (z/z_d)^2}\left(\vec{e}_0 \times \vec{h}_1^* - \vec{e}_1 \times \vec{h}_0^*\right)\right\}$$

where $\tau = T/\tau_0$ is a normalized time coordinate and $z_d = \tau_0^2 / (2\beta_0'')$ is a dispersion length. As an example we consider the propagation of a Gaussian pulse in an $Al_{0.2}Ga_{0.8}As$ nanowire at $\lambda_0 = 1.5 \mu m$, when the core radius is $a = 170 nm$, the nanowire dispersion is $\beta_0'' = 4.48 \, ps^2/m$, and the pulsewidth is $\tau_0 = 500 fs$. Figure 9.4(a) depicts the transverse Poynting vector associated with this case, as obtained from Eq. (9.6), at $T/\tau_0 = -1$ (at the leading edge of the pulse) after a propagation distance of one dispersion length, $L = |z_d|$. As Fig. 9.4(a) clearly indicates, the two negative energy flux wormholes are constantly fed with energy from the sides, from both the core and cladding regions. This energy sinkhole effect is better shown in Fig. 9.4(b), where the

wormhole has been expanded for illustration purposes. On the other hand, at the trailing part of the pulse ($T / \tau_0 > 0$), the situation is reversed, i.e., the wormholes release their energy to the forward S_z components, i.e., they act as sources.
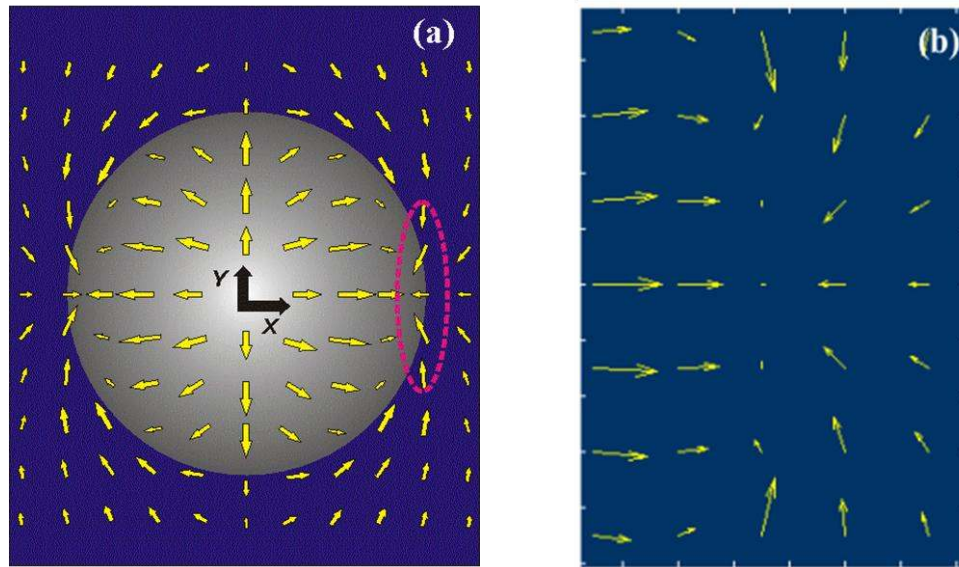
Figure 9.4 (a) Transverse Poynting vector distribution at the leading edge of a pulse (b) An expanded view of the power-flow density around the wormhole area.

Even more importantly, at a certain time-distance (ahead or behind the pulse center) where the power tends to diminish, these wormholes become strongly warped. This warping effect of the power-flow density is schematically illustrated in Fig. 9.5, in the $x - T$ plane.
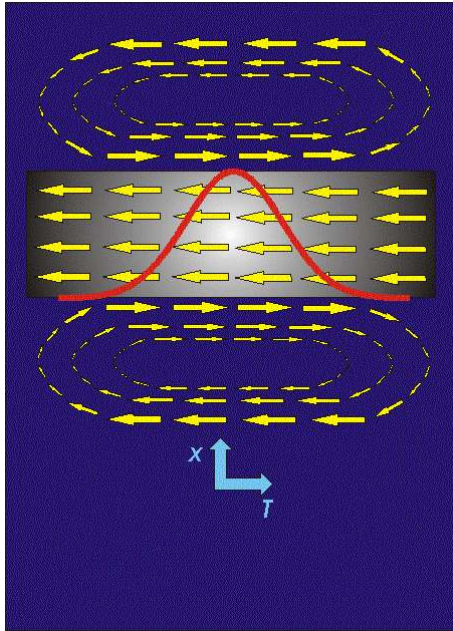
Figure 9.5 Schematic demonstration of the space-time Poynting vector field (in T and x). Power circulation within the pulse (traveling from right to left) is evident.

Our results shed light on how such an energy balance is accomplished around these negative S_z zones. More specifically, at the front of the pulse, these wormholes are fed from the positive S_z regions (from core and cladding) whereas at the back of the pulse this energy is returned. Even under CW conditions, this same reasoning is still applicable if one considers the time history (pulse-fronts) of this field at $T \rightarrow \pm\infty$. It is important to note that the mechanism responsible for setting up the power circulation in these nanowires is fundamentally different from the one involved in similar effects in negative-index (metamaterial) waveguides [83]. As we pointed out before these effects arise because of high-index contrast and geometrical effects.

One possible avenue to detect the presence of these wormholes is to observe the effect of negative S_z on nanoparticles given that these regions primarily exist in the air/vacuum cladding. Since the longitudinal radiation force component is parallel to the S_z vector [8,84,85], then particles located within the wormholes are expected to move towards the source. This is in contrast to what happens in similar configurations using low contrast waveguide structures (particles are repelled away from the source). From the previous discussion the direction of the force is expected to be polarization dependent. Other methods to detect this "negative wind" from dielectric waveguides are also currently considered.

9.4. Conclusion

In conclusion we have shown that that power circulation is possible during pulse propagation in high-contrast optical nanowires. This process is accomplished via negative energy-flux wormholes that are constantly exchanging energy with their surroundings. Our results explain how these zones are formed and provide a detailed account as to their energy balance. The implications of our results on other aspects concerning wave propagation in optical nanowires are currently investigated.

CHAPTER TEN: THEORY OF COUPLED OPTICAL $\mathcal{PT}$ STRUCTURES

10.1. Introduction

Physical systems exhibiting $\mathcal{PT}$ (Parity-Time) symmetry have been the subject of intense investigation in the last few years [86-89]. It has been shown in a series of studies that $\mathcal{PT}$-symmetric Hamiltonians can have a real eigenvalue spectrum-a surprising result given that in general these Hamiltonians are non-Hermitian [86]. Another intriguing aspect associated with this family of pseudo-Hermitian configurations is the possibility of an abrupt phase transition (from a real to a complex spectrum) because of a spontaneous breakdown of $\mathcal{PT}$ symmetry. Following the work of Bender et al [87], an operator $\hat{A}$ is $\mathcal{PT}$ symmetric if it commutes with the $\hat{P}\hat{T}$ operator in which case they share a common set of eigenvectors, i.e. $[\hat{A}, \hat{P}\hat{T}] = 0$. Here the parity operator $\hat{P}$ is defined as $\hat{P}: \hat{x} \rightarrow -\hat{x}, \quad \hat{p} \rightarrow -\hat{p}$ while the time reversal operator leads to $\hat{T}: \hat{p} \rightarrow -\hat{p}, \quad i \rightarrow -i$, where $\hat{p}$ is the momentum operator. From this latter requirement one can show that the potentials associated with these pseudo-Hermitian Schrödinger problems must satisfy the condition $V(x) = V^*(-x)$ [87].

In optics, such complex $\mathcal{PT}$-symmetric structures can be realized within the context of the paraxial theory of diffraction by involving *symmetric index* guiding and an *anti-symmetric gain/loss* profile, that is $n(x) = n^*(-x)$. In other words, the index and gain

guiding [90] in such configurations must be judiciously realized. In these systems, the electric field envelope obeys a normalized complex Schrödinger equation, e.g.:

$$i\frac{\partial \phi(\eta,\xi)}{\partial \xi} + \frac{\partial^2 \phi(\eta,\xi)}{\partial \eta^2} + V(\eta)\,\phi(\eta,\xi) = 0 \qquad (10.1)$$

where $\xi = z/2kx_0^2$ is a scaled propagation distance, $\eta = x/x_0$ is a dimensionless transverse coordinate, and x_0 is an arbitrary spatial scale. Here, $k = 2\pi n_0/\lambda_0$, n_0 is the background refractive index, and $V(\eta) = (2k^2 x_0^2/n_0)n(x/x_0)$ represents the normalized complex index distribution that satisfies the $\mathcal{PT}$ condition. Note that in this physical model, the propagation distance ξ plays the role of time in quantum mechanics. Given the fact that $\mathcal{PT}$ arrangements may provide an additional degree of freedom in synthesizing novel optical structures and materials, of great interest will be to study their optical behavior and characteristics. One fundamental aspect associated with $\mathcal{PT}$ components, never considered before, has to do with their coupled-mode interactions.

In this Letter we formulate a coupled-mode theory appropriate for $\mathcal{PT}$ symmetric optical elements, i.e. when each individual element as well as the entire system respects $\mathcal{PT}$ symmetry. This is done through a Lagrangian treatment of the problem and by employing the particular bra-ket algebra of these systems. As we will see, this new formulation is necessary since the conventional coupled mode theory (CMT) fails in this regime. Pertinent examples are provided to demonstrate the validity of our results.

10.2. Analysis

We begin our analysis by considering the action of the $\hat{P}\hat{T}$ operator on Eq.(10.1), which yields:

$$-i\frac{\partial \phi^*(-\eta,\xi)}{\partial \xi}+\frac{\partial^2 \phi^*(-\eta,\xi)}{\partial \eta^2}+V(\eta)\phi^*(-\eta,\xi)=0 \qquad . \qquad (10.2)$$

Note that in Eq.(10.2) $V(\eta)$ remains invariant as a result of the assumed $\mathcal{PT}$ symmetry. From Eqs. (10.1) and (10.2) one can readily obtain the first conservation law of the system, i.e. $Q=\int_{-\infty}^{\infty}\phi(\eta,\xi)\phi^*(-\eta,\xi)d\eta$ is a constant of motion independent of distance ξ. Note that, in contrast to conventional optical systems, this latter conserved quantity does not represent the actual power. In order to obtain the equations of motion describing the coupling interaction between $\mathcal{PT}$ elements, we employ the Lagrangian density associated with Eq.(10.1) which is given by:

$$L=\frac{i}{2}\left[\phi(\eta)\phi_\xi^*(-\eta)-\phi_\xi(\eta)\phi^*(-\eta)\right]+\phi_\eta(\eta)\phi_\eta^*(-\eta)-V(\eta)\phi(\eta)\phi^*(-\eta) \qquad . \qquad (10.3)$$

Note that variation $\delta L/\delta \phi(\eta,\xi)=\partial_\xi(\partial L/\partial \phi_\xi)+\partial_\eta(\partial L/\partial \phi_\eta)-\partial L/\partial \phi=0$ leads to Eq.(10.2) while $\delta L/\delta \phi^*(-\eta,\xi)=0$ gives Eq.(10.1). In addition, the Hamiltonian invariant of this system is given by $\int_{-\infty}^{\infty}Hd\eta$ where $H=V(\eta)\phi(\eta)\phi^*(-\eta)-\phi_\eta(x)\phi_\eta^*(-\eta)$.

We would like to emphasize that the two conserved quantities Q and the Hamiltonian

H are not related to the optical power (defined as $P = \int\limits_{-\infty}^{\infty} \phi(\eta, \xi) \phi^*(\eta, \xi) d\eta$). In fact even

below phase transition, where the $\mathcal{PT}$ system has a real spectrum, the power P is not

necessarily conserved. Next, let us consider two coupled identical $\mathcal{PT}$ waveguide

elements as shown schematically in Fig. 10.1(a). Note that not only each element is $\mathcal{PT}$,

but also the entire structure respects $\mathcal{PT}$ symmetry with respect to the mirror axis M at

$\eta = 0$.
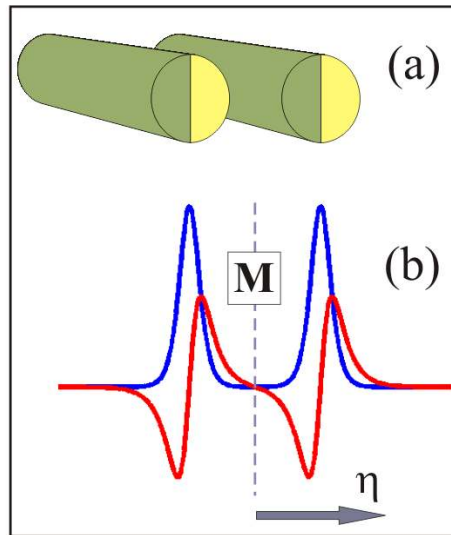
Figure 10.1 $\mathcal{PT}$ –coupled waveguide system: a) waveguide configuration (green

represents gain region while yellow stands for loss region) and b) refractive index (blue)

and gain/loss profile (red). M stands for the mirror symmetry axis.

Here, for simplicity and without any loss of generality, we will consider a 1-D

configuration. In addition we assume that the system is used below the phase transition

point (in the real spectrum domain). We proceed by further assuming that the solution of this coupled $\mathcal{PT}$ arrangement can be expressed as a superposition of the local modes of the individual elements, i.e.:

$$\phi(\eta,\xi) = [a(\xi)u_1(\eta) + b(\xi)u_2(\eta)]\exp(i\mu\xi) \qquad (10.4)$$

where $u_{1,2}(\eta)$ represent the local eigenfunctions of these two waveguides and μ stands for their corresponding propagation eigenvalue. By substituting Eq.(10.4) into the Lagrangian density of Eq. (10.3) and by integrating over η we obtain the reduced Lagrangian of this system $\langle L \rangle = \int_{-\infty}^{\infty} L \, d\eta$ as a function of the modal amplitudes $a(\xi), a^*(\xi), b(\xi), b^*(\xi)$ and their respective derivatives, that is, $\dot{a} = da/d\xi$ etc. The two coupled mode equations can then be obtained by extremizing the reduced Lagrangian with respect to the modal amplitudes. By doing so we find, $i\dot{a}I_{12} + i\dot{b}I_{22} + aJ_{212} + bJ_{122} = 0$ and $i\dot{b}I_{21} + i\dot{a}I_{11} + bJ_{121} + bJ_{211} = 0$. The first equation was obtained from $\delta\langle L \rangle / \delta b^* = 0$ and the second from $\delta\langle L \rangle / \delta a^* = 0$. In these latter equations, $I_{km} = \int_{-\infty}^{\infty} u_m^*(-\eta)u_k(\eta)\, d\eta$ and $J_{jkm} = \int_{-\infty}^{\infty} u_m^*(-\eta)V_j(\eta)u_k(\eta)\, d\eta$. Because of the reflection $-\eta$ used in these inner products (overlap integrals) and the localization of the eigenfunctions u_1 and u_2 around their respective potentials (see Fig. 10.1(b)), one finds that $I_{12} \gg I_{22}$ and $I_{21} \gg I_{11}$. As a result, the coupled mode equations describing this $\mathcal{PT}$ symmetric system are given by:

$$i\frac{da}{d\xi} + \Delta_a a + \kappa\, b = 0 \qquad\qquad \text{(10.5a)}$$

$$i\frac{db}{d\xi} + \Delta_b b + \kappa\, a = 0 \qquad\qquad \text{(10.5b)}$$

where κ is the coupling coefficient ($\kappa = J_{122}/I_{12} = J_{211}/I_{21}$) and $\Delta_{a,b}$ represent shifts in the propagation constants as a result of the coupling interaction.

We next show that the coupling constant in such an arrangement is real. From the assumed $\mathcal{PT}$ symmetry shown in Fig. 10.1(b) it is evident that $u_1(\eta) = u_2^*(-\eta)$. Expressing u_1 in terms of its real and imaginary parts, $u_1 = u_{1R} + iu_{1I}$, we get $I_{12} = \int_{-\infty}^{\infty} u_1^2(\eta)\,d\eta = \int_{-\infty}^{\infty}\left[u_{1R}^2(\eta) - u_{1I}^2(\eta) + 2iu_{1R}(\eta)u_{1I}(\eta)\right]d\eta$. Since for a parity-time symmetric potential $u_{1R}(\eta)$ is an even/odd function while $u_{1I}(\eta)$ is an odd/even function with respect to its local center, it turns out that I_{12} is a real quantity and so is I_{21}. We will next prove that both J_{122} and J_{211} are real. To do so, we consider the evolution equation associated with the first potential in isolation, i.e. Eq.(10.1) with $V(\eta) = V_1(\eta)$. By substituting the stationary solution $\varphi(\eta,\xi) = u_1(\eta)\exp(i\mu\xi)$ in this equation we get $-\mu u_1(\eta) + u_{1\eta\eta}(\eta) + V_1(\eta)u_1(\eta) = 0$. Multiplying this latter expression by $u_2^*(-\eta)$ and by integrating, one can easily show (using integration by parts) that $J_{122} = \int V_1(\eta)u_1(\eta)u_2^*(-\eta)d\eta = \mu\int u_1(\eta)u_2^*(-\eta)d\eta + \int u_{1\eta}(\eta)u_{2\eta}^*(-\eta)d\eta$. The first term in the right hand side, I_{12}, has already been shown to be real and using similar reasoning the second term is also real. The reality of J_{211} is also guaranteed because of symmetry,

e.g. $J_{211} = J_{122}$. Thus the coupling constant $\kappa = J_{122}/I_{12} = J_{211}/I_{21}$ happens to be real. Finally, by considering the $\mathcal{PT}$ symmetry of the coupled structure, it is straight forward to show that J_{212} and J_{121} are complex conjugate of each other and so are the perturbations introduced in the propagation constant of each waveguide, e.g. $\Delta_a = \Delta_b^*$.

In retrospect, we could have arrived at this same formalism by projecting the evolution equations on the $\mathcal{PT}$ symmetric base-functions (bras) $u_{2,1}^*(-\eta)$ as opposed to $u_{1,2}^*(\eta)$ used in conventional coupled-mode theory [71, 91]. We also note that had we used the standard coupled-mode equations it would have erroneously resulted into a complex coupling constant and real propagation constant shifts $\Delta_{a,b}$.

10.3 Numerical verification

We will now illustrate our results using relevant examples. Figure 10.2 (inset) shows the evolution of an input optical beam in a $\mathcal{PT}$ symmetric coupler when each potential in isolation has the form $V(\eta) = A\sec h^2(\eta \pm D/2) + iB\sec h(\eta \pm D/2)\tanh(\eta \pm D/2)$, where $A = \sqrt{2 + B^2/9}$ and D is the separation between the two potentials.

The choice for these particular potentials is motivated by their analytical solutions which in this case are given by: $\sec h(\eta \pm D/2)\exp\left(i(B/3)\tan^{-1}(\sinh(\eta \pm D/2))\right)$. Using the formalism developed above, we have computed the normalized coupling length for various separations D. These results are in excellent agreement with numerical results

obtained from supermode analysis and beam propagation methods as shown in Fig. 10.2. We note that the coupled evolution in this example is affected by the fact that Δ_a and Δ_b are complex conjugate of each other (effectively one arm exhibits gain and the other loss).
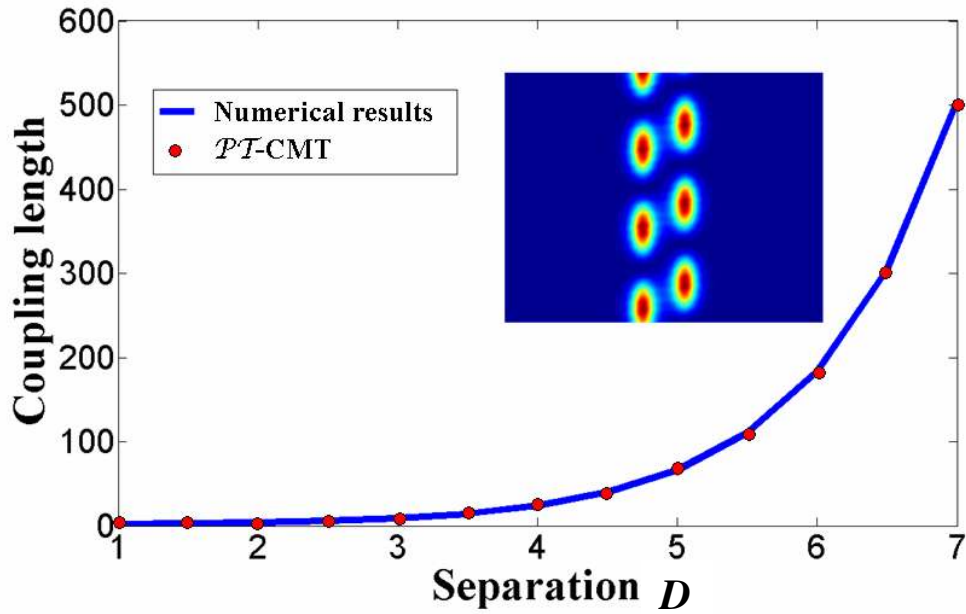
Figure 10.2 Normalized coupling length calculated from supermode analysis (solid curve) compared with that obtained from the PT-coupled mode theory (dots) as a function of waveguide separation D. Inset shows a simulation of beam propagation when the separation between the two waveguides is D=4.

Fig. 10.3 on the other hand depicts the evolution of a single channel excitation in an array made of $\mathcal{PT}$ potentials (below phase transition), used in the previous example. In this configuration, the phase-shift of the diffracted beams at the left and right channels ($\pm m$) is compared and found to be zero, in excellent agreement with the predictions of

the coupled mode theory derived here (suggesting a real coupling constant). Because of this arrangement, in this infinite array both the propagation shifts Δ_n and the coupling constant are now real and hence the modal amplitudes (associated with the bound states of the first band) evolve as if the array was entirely lossless [92], e.g.

$$i(da_n / d\xi) + \kappa(a_{n+1} + a_{m-1}) = 0.$$
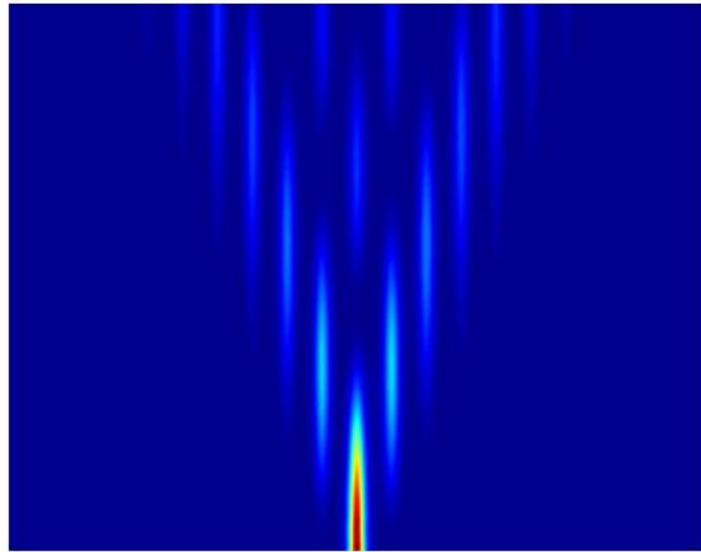
Figure 10.3 Discrete diffraction in a PT-waveguide array resulting from a single channel excitation.

As a result, if the array is excited at the middle, the discrete diffraction pattern follows the familiar Bessel distribution, that is $a_n = (i)^n J_n(2\kappa\xi)$.

We would also like to stress that the Lagrangian formalism can also be used to obtain shifts in the propagation constant due to $\mathcal{PT}$ perturbations (i.e. a perturbations that preserve the parity-time symmetry) below the phase transition. In this case we assume a solution of the form $\phi(\eta,\xi) = a(\xi)u(\eta)\exp(i\mu\xi)$ where $u(\eta)\exp(i\mu\xi)$ is the eigenfunction of the unperturbed system. Following exactly the same procedure as before and by solving the resultant differential equation we find:

$$\Delta\mu = \frac{\displaystyle\int_{-\infty}^{\infty} u^*(-\eta)\Delta V(\eta)u(\eta)d\eta}{\displaystyle\int_{-\infty}^{\infty} u^*(-\eta)u(\eta)d\eta} \qquad . \quad (10.6)$$

where $\Delta\mu$ is the perturbation in the propagation constant due to the $\mathcal{PT}$ perturbation in the optical potential $\Delta V(\eta)$. We note that the result of Eq.(10.6) is again fundamentally different from that known from standard perturbation theory [93]. Excellent agreement was obtained between the numerically found solution and the result of Eq.(10.6).

In conclusion, starting from Lagrangian principles we have developed a formalism suitable for describing coupled optical $\mathcal{PT}$ (Parity-Time) symmetric systems. In addition, we showed that the same technique can be used to derive a perturbation analysis for PT waveguide operating below the phase transition point.

CHAPTER ELEVEN: CONCLUSIONS

In conclusion, this thesis is comprised of two main parts. In the first one we have studied the nonlinear optical response of nano-particle suspensions. Starting from first principles and in the absence of particle-particle interactions, we analyzed the nonlinear response as well as the nonlinear Rayleigh losses associated with nano-particle suspensions. This was done by directly solving the underlying Nernst-Planck and Smoluchowski equations under equilibrium conditions. We have demonstrated that in such systems both the optical nonlinearity and Rayleigh losses vary exponentially with optical intensity. This exponential dependence was shown to be saturable or supercritical depending on the sign of the particle polarizability. The soliton solutions corresponding to these two cases were obtained and their dynamics as well as stability properties were investigated for both 1D and 2D geometries.

The modulational and transverse modulational instabilities of nonlinear beams propagating in transparent colloids were also studied systematically. We have shown that the process of modulational instability (MI) depends on the boundary conditions, i.e. on the overlap between the exciting beam and the colloidal cell with the result that the MI behavior can display either Kerr or non-Kerr characteristics. Transverse modulation instabilities of soliton stripe beams were investigated and a new instability regime was identified as a result of the 1D collapse caused by the exponential nonlinearity.

In order to gain more understanding of the system's behavior, we have expanded our model so as to take into account many-body effects on the nonlinear optical response

of stabilized colloidal systems. Starting from a "non-ideal gas" equation of state and by taking into account the screened Coulomb interactions between suspended nano-particles, we have shown that the nonlinear optical behavior of these colloids can range anywhere from exponential to polynomial depending on their filling density, composition, and chemistry. It was then demonstrated that this in turn has a profound effect on optical beam dynamics. The stability of optical beams in systems with positive polarizabilities was also studied in both 1D and 2D configurations. Experimental data carried out by one of our collaborative groups was also presented. By using semi-analytical variational techniques as well as fully numerical beam propagation methods, we compared the measurements with the different proposed models and we found good agreement with the many-body interaction model.

Conservation laws of the system are typically used to check the validity and accuracy of simulations. In nonlinear optics, among the most commonly used constants of motion are those associated with the power and the Hamiltonian. The advantage of using the Hamiltonian is that, as opposed to the power, its form is unique for each evolution equation. For problems such as that of nonlinear propagation in interacting colloidal suspensions it was thus far impossible to calculate the numerical value of the Hamiltonian. To overcome this obstacle we introduced the concept of the shifted Hamiltonian density. We have shown that for localized initial conditions and for a finite simulation window, the shifted Hamiltonian will be conserved and we described in detail how to obtain its numerical value in both one and two dimensions.

The second part deals with linear and nonlinear properties of optical nano-waveguides. In particular we have demonstrated that optical solitons can exist in dispersion-inverted highly-nonlinear *AlGaAs* nanowires. This is accomplished by strongly reversing the dispersion of these nano-structures to anomalous over a broad frequency range. We have shown that these self-localized waves are possible at very low power levels and can form in millimeter long nanowire structures. The intensity and spectral evolution of solitons propagating in such *AlGaAs* nanowaveguides were also investigated in the presence of loss, multiphoton absorption and higher-order dispersion.

We have also shown that energy circulation within a pulse is possible when it propagates in a high-contrast dielectric nanowire. Our analysis revealed that this process is accomplished through electromagnetic "wormhole" regions, in which the Poynting vector associated with the guided mode is negative with respect to the direction of propagation. For demonstration purposes this mechanism was elucidated in *AlGaAs* and silicon nanowaveguides where the effect of dispersion on the power circulation was also considered.

Finally we have developed a coupled mode theory (CMT) for parity-time ($\mathcal{PT}$) symmetric waveguide couplers. For this type of structures, it was found that the conventional coupled mode theory completely fails and thus it was necessary to develop a new CMT. In this work we have started from the Lagrangian formalism of the problem and we were able to derive a suitable CMT. Our results

were checked using numerical simulations and excellent agreement with theory was demonstrated.

APPENDIX A: OPTICAL GRADIENT FORCE

Here we present a full derivation of the optical gradient force expression. Figure 1 depicts an optical dipole consisting of equal and opposite electric charges q and $-q$. In our frame of reference the position vector of the first charge is assumed to be $\vec{r_1}$ and $\vec{r_2}$ where $\vec{r_1} = (x_1, y_1, z_1)$ and $\vec{r_2} = (x_2, y_2, z_2)$.
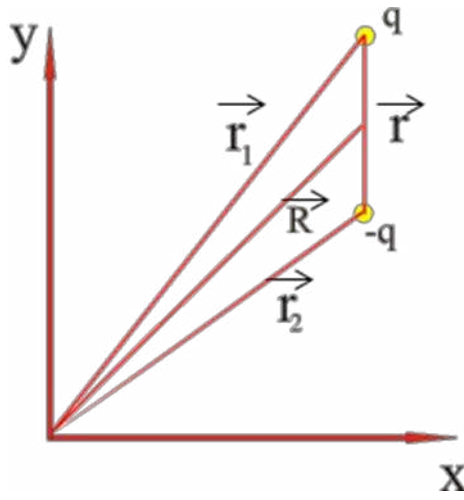
Figure A.1 Electric dipole equivalent to electrically small dielectric sphere

Let $\vec{r} = \vec{r_1} - \vec{r_2} = (\Delta x, \Delta y, \Delta z)$ and $\vec{R} = \dfrac{m_1}{M}\vec{r_1} + \dfrac{m_2}{M}\vec{r_2} = (x_0, y_0, z_0)$

where $\vec{R}$ is the center of mass of the electric dipole. Solving the previous equation, one can easily show that $\vec{r_1} = \vec{R} + \dfrac{m_2}{M}\vec{r}$ and $\vec{r_2} = \vec{R} - \dfrac{m_1}{M}\vec{r}$. Under the action of electromagnetic field, the equations of motion of the positive and negative charges are given by:

$$m_1\ddot{\vec{r_1}} = q\left[\vec{E}(\vec{r_1},t) + \dot{\vec{r_1}} \times \vec{B}(\vec{r_1},t)\right] + \vec{F_b} \qquad (A.1)$$

$$m_2\ddot{\vec{r_2}} = q\left[\vec{E}(\vec{r_2},t) + \dot{\vec{r_2}} \times \vec{B}(\vec{r_2},t)\right] - \vec{F_b} \qquad (A.2)$$

Where $\vec{F}$ is the binding force between the two charges. Next we express both the electric and magnetic fields in terms of the vectors $\vec{r}$, $\vec{R}$ and using Taylor series expansion. For the electric field component, the expansion is given by:

$$\vec{E}\left(\vec{r}_1,t\right) = \vec{E}\left(\vec{R}+\frac{m_2}{M}\vec{r},t\right) = \sum_i E_i\left(x_0+\frac{m_2}{M}\Delta x,\, y_0+\frac{m_2}{M}\Delta y,\, z_0+\frac{m_2}{M}\Delta z\right)\,\vec{e}_i$$

$$= \sum_i\left(E_i\left(x_0,y_0,z_0\right)+\frac{m_2}{M}\Delta x\frac{\partial E_i}{\partial x}\Big|_{x_0}+\frac{m_2}{M}\Delta y\frac{\partial E_i}{\partial y}\Big|_{y_0}+\frac{m_2}{M}\Delta z\frac{\partial E_i}{\partial z}\Big|_{z_0}\right)\,\vec{e}_i$$

$$= \vec{E}\left(\vec{R},t\right)+\frac{m_2}{M}\sum_i\vec{e}_i\left(\Delta x\;\vec{e}_x+\Delta y\;\vec{e}_y+\Delta y\;\vec{e}_y\right)\cdot\left(\frac{\partial E_i}{\partial x}\vec{e}_x+\frac{\partial E_i}{\partial y}+\frac{\partial E_i}{\partial z}\right)\text{Writi}$$

$$= \vec{E}\left(\vec{R},t\right)+\frac{m_2}{M}\sum_i\vec{e}_i\left(\vec{r}\cdot\vec{\nabla}E_i\right)=\vec{E}\left(\vec{R},t\right)+\frac{m_2}{M}\left(\vec{r}\cdot\vec{\nabla}\right)\vec{E}$$

ng a similar expression for the magnetic field, we get:

$$m_1\left(\ddot{\vec{R}}+\frac{m_2}{M}\ddot{\vec{r}}\right) = q\left\{\left[\vec{E}\left(\vec{R},t\right)+\frac{m_2}{M}\left(\vec{r}\cdot\vec{\nabla}\right)\vec{E}\left(\vec{R},t\right)\right]+\left(\dot{\vec{R}}+\frac{m_2}{M}\dot{\vec{r}}\right)\times\left(\vec{B}\left(\vec{R},t\right)+\frac{m_2}{M}\left(\vec{r}\cdot\vec{\nabla}\right)\vec{B}\left(\vec{R},t\right)\right)\right\}+\vec{F}$$

$$(A.3)$$

$$m_2\left(\ddot{\vec{R}}-\frac{m_1}{M}\ddot{\vec{r}}\right) = -q\left\{\left[\vec{E}\left(\vec{R},t\right)-\frac{m_1}{M}\left(\vec{r}\cdot\vec{\nabla}\right)\vec{E}\left(\vec{R},t\right)\right]+\left(\dot{\vec{R}}-\frac{m_1}{M}\dot{\vec{r}}\right)\times\left(\vec{B}\left(\vec{R},t\right)-\frac{m_1}{M}\left(\vec{r}\cdot\vec{\nabla}\right)\vec{B}\left(\vec{R},t\right)\right)\right\}-\vec{F}$$

$$(A.4)$$

Setting $m_1 = m_2$ and adding Eq.(3) and (4), one gets:

$$M\ddot{\vec{R}} = q\left[\left(\vec{r}\cdot\vec{\nabla}\right)\vec{E}\left(\vec{R},t\right)+\dot{\vec{r}}\times\vec{B}\left(\vec{R},t\right)+\dot{\vec{R}}\times\left(\vec{r}\cdot\vec{\nabla}\right)\vec{B}\left(\vec{R},t\right)\right]$$

Since $\vec{R}$ is not a vector field, $\left(\vec{r}\cdot\vec{\nabla}\right)$ does not act on $\vec{R}$ and the last equation can be written as:

$$M\ddot{\vec{R}} = q\left[\left(\vec{r}\cdot\vec{\nabla}\right)\left(\vec{E}\left(\vec{R},t\right)+\dot{\vec{R}}\times\vec{B}\left(\vec{R},t\right)\right)+\dot{\vec{r}}\times\vec{B}\left(\vec{R},t\right)\right]$$

$$= \left(\vec{p}\cdot\vec{\nabla}\right)\left[\vec{E}\left(\vec{R},t\right)+\dot{\vec{R}}\times\vec{B}\left(\vec{R},t\right)\right]+\dot{\vec{p}}\times\vec{B}\left(\vec{R},t\right)$$

(A.5)

The last term in eq.(A.5) can be expressed as:

$$\dot{\vec{p}}\times\vec{B}\left(\vec{R},t\right)=\frac{d}{dt}\left(\vec{p}\times\vec{B}\left(\vec{R},t\right)\right)-\vec{p}\times\frac{d}{dt}B\left(\vec{R},t\right)$$

where

$$\frac{d}{dt}B\left(\vec{R},t\right)=\frac{d}{dt}\vec{B}\left(x_0,y_0,z_0,t\right)=\frac{\partial}{\partial t}\vec{B}\left(\vec{R},t\right)+\frac{\partial}{\partial t}\frac{x_0}{\partial}\frac{\partial\vec{B}}{\partial x_0}+\frac{\partial}{\partial t}\frac{y_0}{\partial}\frac{\partial\vec{B}}{\partial y_0}+\frac{\partial}{\partial t}\frac{z_0}{\partial}\frac{\partial\vec{B}}{\partial z_0}$$

$$=\frac{\partial}{\partial t}\vec{B}\left(\vec{R},t\right)+\left(\frac{\partial x_0}{\partial t}\frac{\partial}{\partial x_0}+\frac{\partial y_0}{\partial t}\frac{\partial}{\partial y_0}+\frac{\partial z_0}{\partial t}\frac{\partial}{\partial z_0}\right)\vec{B}\left(\vec{R},t\right)$$

$$=\frac{\partial}{\partial t}\vec{B}\left(\vec{R},t\right)+\left(\dot{\vec{R}}\cdot\vec{\nabla}\right)\vec{B}\left(\vec{R},t\right)$$

But from Maxwell's equations, we have $\dfrac{\partial}{\partial t}B\left(\vec{R},t\right)=-\vec{\nabla}\times E\left(\vec{R},t\right)$.

$$\therefore\quad \dot{\vec{p}}\times\vec{B}\left(\vec{R},t\right)=\frac{d}{dt}\left(\vec{p}\times\vec{B}\left(\vec{R},t\right)\right)+\vec{p}\times\vec{\nabla}\times E\left(\vec{R},t\right)-\vec{p}\times\left(\dot{\vec{R}}\cdot\vec{\nabla}\right)\vec{B}\left(\vec{R},t\right)$$

Because $\left(\dot{\vec{R}}\cdot\vec{\nabla}\right)$ is a scalar vector that does not act on $\vec{p}$, we get:

$$\dot{\vec{p}}\times\vec{B}\left(\vec{R},t\right)=\frac{d}{dt}\left(\vec{p}\times\vec{B}\left(\vec{R},t\right)\right)+\vec{p}\times\vec{\nabla}\times E\left(\vec{R},t\right)-\left(\dot{\vec{R}}\cdot\vec{\nabla}\right)\left(\vec{p}\times\vec{B}\left(\vec{R},t\right)\right)$$

Substituting in eq.(A.5) gives:

$$M\ddot{\vec{R}}=\left(\vec{p}\cdot\vec{\nabla}\right)\left[\vec{E}\left(\vec{R},t\right)+\dot{\vec{R}}\times\vec{B}\left(\vec{R},t\right)\right]+\frac{d}{dt}\left(\vec{p}\times\vec{B}\left(\vec{R},t\right)\right)+\vec{p}\times\vec{\nabla}\times E\left(\vec{R},t\right)-\left(\dot{\vec{R}}\cdot\vec{\nabla}\right)\left(\vec{p}\times\vec{B}\left(\vec{R},t\right)\right)$$

(A.6)

Using the vector identities $\left(\vec{p}\cdot\vec{\nabla}\right)\left(\dot{\vec{R}}\cdot\vec{B}\right)-\left(\dot{\vec{R}}\cdot\vec{\nabla}\right)\left(\vec{p}\cdot\vec{B}\right)=\left[\vec{\nabla}\left(\dot{\vec{R}}\times\vec{B}\right)\right]\cdot\vec{p}$ and

$\vec{p}\times\vec{\nabla}\times\vec{E}=\left(\vec{\nabla}\vec{E}\right)\cdot\vec{p}-\left(\vec{p}\cdot\vec{\nabla}\right)\vec{E}$, eq.(6) can be written in the following simple form:

$$M\ddot{\vec{R}}=\vec{p}\cdot\left[\vec{\nabla}\left(\vec{E}+\dot{\vec{R}}\times\vec{B}\right)\right]+\frac{d}{dt}\left(\vec{p}\times\vec{B}\right) \tag{A.7}$$

Several comments have to be made at this point. First the ratio between the magnetic field to the electric field is of the order of $\approx 1/c$ where c is the speed of light and thus the second term can be neglected. Second the time average of the third term is zero and hence we have

$$\left\langle M\ddot{\vec{R}}\right\rangle\cong\left\langle\vec{p}\cdot\left(\vec{\nabla}\vec{E}\right)\right\rangle \tag{A.8}$$

Using $\vec{p}=\alpha\ \vec{E}$ we get

$$\text{Optical force}\quad F=\left\langle M\ddot{\vec{R}}\right\rangle\cong\left\langle\vec{p}\cdot\left(\vec{\nabla}\vec{E}\right)\right\rangle=\frac{\alpha}{2}\vec{\nabla}E^2 \tag{A.9}$$

If write the electric field as:

$$E_i\left(x,y,z,t\right)=\frac{1}{2}\left[A_i\left(x,y,z\right)e^{j\omega t}+A_i^*\left(x.y.z\right)e^{-j\omega t}\right]\quad,i=x,y,z$$

$$\therefore E_i^2=\frac{1}{4}\left(A_i^2 e^{2j\omega t}+c.c+2A_iA_i^*\right)$$

$$\therefore\left\langle E_i^2\right\rangle=\frac{1}{2}A_iA_i^*=\frac{1}{2}\left|A_i\right|^2$$

Since the time average operator $\langle\ \rangle$ does not act on the space operators, then we get

$\left\langle\dfrac{\partial E_i^2}{\partial x_i}\right\rangle=\dfrac{\partial}{\partial x_i}\left\langle E_i^2\right\rangle$ which finally gives:

$$F=\left\langle\left(\nabla\vec{E}\right)\cdot\vec{p}\right\rangle=\frac{\alpha}{4}\nabla I \tag{A.10}$$

113

Where $I = \left|A_x\right|^2 + \left|A_y\right|^2 + \left|A_z\right|^2$.

Equation (A.10) is the main result of this section and it expresses the optical gradient force on nano/micro particles in terms of the applied electric field components.

APPENDIX B: CALCULATION OF THE THIRD VIRIAL COEFFICIENT (B₃)

Here we give a brief description of Katsura's Fourier Transform method [94] that was used for the calculations of the third virial coefficient $B_3(T)$. In order to do so, we start from the expression for $B_3(T)$, i.e. $B_3(T) = -1/3 \int f_u(\vec{r}_{12}) f_u(\vec{r}_{13}) f_u(\vec{r}_{12} - \vec{r}_{13}) d\vec{r}_{12} d\vec{r}_{13}$. If the potential energy between any two particles depends only on their relative positions (as it is in our case), and by using the substitution $\vec{\zeta}_i = \vec{r}_i - \vec{r}_1$, we obtain:

$$B_3(T) = -1/3 \int f_u(|\vec{\zeta}_2|) f_u(|\vec{\zeta}_3|) f_u(|\vec{\zeta}_3 - \vec{\zeta}_2|) d\vec{\zeta}_2 \vec{\zeta}_3 \quad . \qquad (B1)$$

The Fourier transform of $f_u(|\vec{\zeta}|)$ can be written as $\tau(\vec{k}_\zeta) = (2\pi)^{-3/2} \int f_u(|\vec{\zeta}|) exp(-i\vec{k}_\zeta \cdot \vec{\zeta}) d\vec{\zeta}$ where $\vec{k}_\zeta$ is a conjugate vector in the Fourier space. If we denote $\zeta = |\vec{\zeta}|$ and $k_\zeta = |\vec{k}_\zeta|$, then one can write the above expression in the spherical coordinate system (ζ, θ, ϕ) as:

$$\tau(k_\zeta) = (2\pi)^{-3/2} \int_0^\infty \int_0^\pi \int_0^{2\pi} f_u(\zeta) exp[-ik_\zeta \zeta \cos(\theta)] \zeta^2 \sin(\theta) d\zeta d\theta d\phi, \qquad (B2)$$

where in the last equation $\vec{k}_\zeta$ were chosen to coincide with the $\vec{z}$ axis of the spherical coordinate system (ζ, θ, ϕ). This choice is allowed since the function $f_u(|\vec{\zeta}|)$ depends only on the magnitude of $\vec{\zeta}$. The last integral can be further simplified to obtain:

$$\tau(\zeta) = \sqrt{\frac{2}{\pi}} \int_0^\infty \zeta f_u(\zeta) \frac{\sin(k_\zeta \zeta)}{k_\zeta} d\zeta \quad . \qquad (B3)$$

Similar expression can also be derived for the inverse transform. Substituting in Eq.(B1), and after some mathematical manipulations, it can be shown that:

$$B_3 = \frac{-(2\pi)^{3/2}}{3} \int_0^\infty 4\pi k_\zeta^2 \tau^3 \left(k_\zeta \right) dk_\zeta \quad . \tag{B4}$$

Eqs. (B3) and (B4) can then be used together to obtain numerical values of the third virial

coefficient B_3. Note that by using this technique, the calculations are reduced to only two

dimensional integral (Eqs. (B3) and (B4)) instead of the six dimensional of Eq.(B1).

APPENDIX C: NEGATIVE POWER FLOW IN HIGH INDEX NANO-FIBERS

Here we present detailed derivation for Eqs.(9.6) of chapter nine. The electric and magnetic fields of a pulse propagating in a nano-fiber within the HE_{11} mode can be written as:

$$\left\{\begin{matrix}\vec{E}\\ \vec{H}\end{matrix}\right\} = \frac{1}{2\pi}\int\limits_{-\infty}^{\infty} d\Omega\,\Phi_0(\Omega)\,e^{i\left[(\omega_0+\Omega)t-\beta(\omega_0+\Omega)z\right]}\left\{\begin{matrix}\vec{e}(\vec{r}_\perp,\omega_0+\Omega)\\ \vec{h}(\vec{r}_\perp,\omega_0+\Omega)\end{matrix}\right\} \quad \text{(C.1)}$$

where ω_0 is the carrier angular frequency of the wavepacket, $\beta(\omega_0+\Omega)$ is the propagation constant of the HE_{11} having a frequency $\omega = \omega_0+\Omega$ and $\vec{r}_\perp$ is a position vector. In the above equation $\vec{e}$ and $\vec{h}$ are the electric and magnetic field components of the HE_{11} mode, respectively and $\Phi_0(\Omega)$ is the pulse envelope frequency spectrum with Ω being a frequency deviation from ω_0. If we define the dispersion function as $F(\Omega) = \beta(\omega_0+\Omega)-\beta_0-\beta_0'\Omega$ where $\beta_0 = \beta(\omega_0)$ and $\beta_0' = \partial\beta/\partial\omega\big|_{\omega=\omega_0} = 1/v_g$, then Eq.(C.1) becomes:

$$\left\{\begin{matrix}\vec{E}\\ \vec{H}\end{matrix}\right\} = \frac{e^{i\left[\omega_0 t-\beta_0 z\right]}}{2\pi}\int\limits_{-\infty}^{\infty} d\Omega\,\Phi_0(\Omega)\,e^{i\left[\Omega t-(\Omega/v_g)z-F(\Omega)z\right]}\left\{\begin{matrix}\vec{e}(\vec{r}_\perp,\omega_0+\Omega)\\ \vec{h}(\vec{r}_\perp,\omega_0+\Omega)\end{matrix}\right\} \quad \text{(C.2)}$$

Next we adopt a moving frame of reference with $T = t - z/v_g$, and we introduce the quantity

$$\phi(z,T) = \frac{1}{2\pi} \int\limits_{-\infty}^{\infty} d\Omega \Phi_0(\Omega) e^{i\Omega T} e^{-iF(\Omega)z} \qquad \text{(C.3)}$$

Assuming slowly varying envelop, one can expand the field vectors according to:

$$\begin{Bmatrix} \vec{e}(\vec{r}_\perp, \omega_0 + \Omega) \\ \vec{h}(\vec{r}_\perp, \omega_0 + \Omega) \end{Bmatrix} = \begin{Bmatrix} \vec{e}_0 + \vec{e}_1\Omega \\ \vec{h}_0 + \vec{h}_1\Omega \end{Bmatrix} \qquad \text{(C.4)}$$

Where $\vec{e}_0 = \vec{e}(\vec{r}_\perp, \omega_0)$ and $\vec{e}_1 = d\vec{e}/d\omega\big|_{\omega_0}$ and similarly for the magnetic field components $\vec{h}$. Subsituting Eqs (C.4) in Eq.(C.2) we obtain:

$$\begin{Bmatrix} \vec{E} \\ \vec{H} \end{Bmatrix} = \frac{e^{i[\omega_0 t - \beta_0 z]}}{2\pi} \int\limits_{-\infty}^{\infty} d\Omega \Phi_0(\Omega) e^{i[\Omega T - F(\Omega)z]} \left[\begin{Bmatrix} \vec{e}_0 \\ \vec{h}_0 \end{Bmatrix} + \begin{Bmatrix} \vec{e}_1 \\ \vec{h}_1 \end{Bmatrix} \Omega \right] \qquad \text{(C.5)}$$

Using the properties of Fourier transform and by taking into account the definition of $\phi(z,T)$ in Eq. (C.3), this last equation reduces to

$$\begin{Bmatrix} \vec{E} \\ \vec{H} \end{Bmatrix} = e^{i[\omega_0 t - \beta_0 z]} \left[\begin{Bmatrix} \vec{e}_0 \\ \vec{h}_0 \end{Bmatrix} \phi(z,T) - i \begin{Bmatrix} \vec{e}_1 \\ \vec{h}_1 \end{Bmatrix} \frac{\partial \phi}{\partial T} \right] \qquad \text{(C.6)}$$

The time average Poynting vector is now obtained from:

$$\vec{\mathcal{P}} = \frac{1}{2}\operatorname{Re}\left\{\vec{E}\times\vec{H}^*\right\} = \frac{1}{2}\operatorname{Re}\left\{\left(\phi\vec{e}_0 - i\frac{\partial \phi}{\partial T}\vec{e}_1\right)\times\left(\phi^*\vec{h}_0^* + i\frac{\partial \phi^*}{\partial T}\vec{h}_1^*\right)\right\} \qquad \text{(C.7)}$$

By neglecting terms that include $\vec{e}_1 \times \vec{h}_1$, we finally arrive at:

$$\vec{\mathcal{P}} = \frac{1}{2}|\phi|^2 \operatorname{Re}\left\{\vec{e}_0\times\vec{h}_0^*\right\} + \frac{1}{2}\operatorname{Re}\left\{i\phi\frac{\partial \phi^*}{\partial T}\vec{e}_0\times\vec{h}_1^* - i\phi^*\frac{\partial \phi}{\partial T}\vec{e}_1\times\vec{h}_0^*\right\} \qquad \text{(C.8)}$$

Note that $\operatorname{Re}\left\{\vec{e}_0\times\vec{h}_0^*\right\}$ is parallel to the direction of propagation, $\hat{z}$ [71]. By writing φ in the polar representation, i.e. $\phi = Ae^{i\psi}$, we get $\phi_T = A_T e^{i\psi} + i\psi_T A e^{i\psi}$. It then immediately follows that $\phi_T\phi^* = AA_T + iA^2\psi_T$ and $\phi_T^*\phi = AA_T - iA^2\psi_T$. Substituting this last result in Eq.(C.8), and by noting that $AA_T = (A^2)_T /2$, we find that the expression of the Poynting vector takes the form:

$$\vec{\mathcal{P}} = \frac{1}{2}A^2 \operatorname{Re}\left\{\vec{e}_0\times\vec{h}_0^*\right\} + \frac{1}{2}A^2\psi_T \operatorname{Re}\left\{\vec{e}_0\times\vec{h}_1^* + \vec{e}_1\times\vec{h}_0^*\right\}$$
$$+ \frac{(A^2)_T}{4}\left\{i\left(\vec{e}_0\times\vec{h}_1^* - \vec{e}_1\times\vec{h}_0^*\right)\right\} \qquad \text{(C.9)}$$

For a finite energy pulse, $\int_{-\infty}^{\infty}(A^2)_T dT = A^2\big|_{-\infty}^{\infty} = 0$. Note also that:

$$\text{Re}\left\{\vec{e}_0 \times \vec{h}_1^* + \vec{e}_1 \times \vec{h}_0^*\right\} = \text{Re}\left\{\vec{e}\left(\omega_0\right) \times \left.\frac{\partial \vec{h}^*}{\partial \omega}\right|_{\omega_0} + \left.\frac{\partial \vec{e}}{\partial \omega}\right|_{\omega_0} \times \vec{h}^*\left(\omega_0\right)\right\}$$

$$= \text{Re}\left\{\left.\frac{\partial}{\partial \omega}\left[\vec{e}\left(\omega\right) \times \vec{h}^*\left(\omega\right)\right]\right|_{\omega=\omega_0}\right\} = \left.\frac{\partial}{\partial \omega}\left[\text{Re}\left\{\vec{e}\left(\omega\right) \times \vec{h}^*\left(\omega\right)\right\}\right]\right|_{\omega=\omega_0}$$

(C.10)

It is worth noting that in the above expression, the interchange of the "real part" operator (Re) with the differentiation operator ($\partial/\partial \omega$) is valid because ω itself is real.

Since $\text{Re}\left\{\vec{e}\left(\omega\right) \times \vec{h}^*\left(\omega\right)\right\} // \hat{z}$ irrespective of the value of ω, it follows that

$\frac{\partial}{\partial \omega}\left[\text{Re}\left\{\vec{e}\left(\omega\right) \times \vec{h}^*\left(\omega\right)\right\}\right] // \hat{z}$. In other words, the term $\text{Re}\left\{\vec{e}_0 \times \vec{h}_1^* + \vec{e}_1 \times \vec{h}_0^*\right\}$ is parallel to

the propagation direction $\hat{z}$ and hence, for pulses conveying finite energy $\int_{-\infty}^{\infty} \vec{\mathcal{P}}dT$ is also

a vector pointing in the propagation direction $\hat{z}$. This result should have been anticipated since we are dealing with pulse propagation in a guiding structure. Assuming an initial Gaussian pulse of the form $\phi(z=0,T) = E_0 \exp(-t^2/\tau_0^2) = E_0 \exp(-T^2/\tau_0^2)$ and by considering only group velocity dispersion, i.e. $F(\Omega) = \beta_0^{"}\Omega^2/2$, it is straight forward to show that $\Phi_0\left(\Omega\right) = E_0\tau_0\sqrt{\pi}\exp\left(-\Omega^2\tau_0^2/4\right)$. At any distance z, we have:

$$\phi\left(z,T\right) = \frac{E_0\tau_0\sqrt{\pi}}{2\pi} \int_{-\infty}^{\infty} d\Omega\, e^{-\Omega^2\tau_0^2/4} e^{i\Omega T} e^{-i\left(\beta''\Omega^2/2\right)z} \quad \text{(C.11)}$$

By writing $z_d = \tau_0^2/\left(2\beta_0^{"}\right)$, and $\tau = T/\tau_0$, the integration in (C.11) yields:

$$\phi(z,T) = \frac{E_0}{\sqrt{1+i(z/z_d)}} \exp\left(\frac{-\tau^2}{1+i(z/z_d)}\right)$$

$$= \frac{E_0}{\left[1+(z/z_d)^2\right]^{1/4} \exp\left[\frac{i}{2}\tan^{-1}(z/z_d)\right]} \exp\left(\frac{-T^2}{\tau_0^2\left[1+(z/z_d)^2\right]}\right) \exp\left(\frac{iT^2(z/z_d)}{\tau_0^2\left[1+(z/z_d)^2\right]}\right)$$

(C.12)

In other words:

$$A = \frac{E_0}{\left[1+(z/z_d)^2\right]^{1/4}} \exp\left(\frac{-T^2}{\tau_0^2\left[1+(z/z_d)^2\right]}\right)$$

(C.13.a)

$$\psi = \frac{T^2(z/z_d)}{\tau_0^2\left[1+(z/z_d)^2\right]} - \frac{i}{2}\tan^{-1}(z/z_d)$$

(C.13.b)

Finally, by differentiation, we find that:

$$\left(A^2\right)_T = \frac{A^2}{\tau_0} \frac{-4T}{\tau_0\left[1+(z/z_d)^2\right]}$$

(C.14.a)

$$A^2\psi_T = \frac{A^2}{\tau_0} \frac{2T(z/z_d)}{\tau_0\left[1+(z/z_d)^2\right]}$$

(C.14.b)

Eq. (C14) together with (C.9) directly lead to Eq.(9.6) of chapter 9.

REFERENCES

1. G. G. Hammes, *Thermodynamics and Kinetics for the Biological Sciences*, (John Wiley and Sons 2000).

2. A. Ashkin, J.M. Dziedzic, J.E. Bjorkholm and S. Chu, "Observation of single-beam gradient force optical trap for dielectric particles," Opt. Lett. **11**, 288-290 (1986).

3. A. Ashkin, "History of optical trapping and manipulation of small-neutral particle, atoms, and molecules" IEEE Journal of Selected Topics in Quantum Electronics, **6**, 841 (2000).

4. Ashkin, J. M. Dziedzic, and P. W. Smith, "Continuous-wave self-focusing and self-trapping of light in artificial Kerr media," Opt. Lett **7**, 276-278 (1982).

5. P. W. Smith, Ashkin, and W. J. Tomlinson,"Four-wave mixing in an artificial Kerr medium," Opt. Lett **6**, 284-286 (1981).

6. P. W. Smith, P. J. Maloney, and A. Ashkin, "Use of a liquid suspension of dielectric spheres as an artificial Kerr medium," Opt. Lett **7,** 347-349 (1982).

7. P. W. Smith, A. Ashkin, J. E. Bjorkholm, and D. J. Eilenberger, "Studies of self-focusing bistable devices using liquid suspensions of dielectric particles," Opt. Lett. **9**, 131 (1984)

8. J.P. Gordon, "Radiation Forces and Momenta in Dielectric Media," Phys. Rev. A **8**, 14-21 (1973).

9. S. Stenholm, "The semiclassical theory of laser cooling," Rev. Mod. Phys. **58**, 699-739 (1986).

10. V. E. Yashin, S. A. Chizhov, R. L. Sabirov, T. V. Starchikova, N. V. Vysotina, N. N. Rozanov, V. E. Semenov, V. A. Smirnov, and S. V. Fedorov, "Formation of soliton-like light beams in an aqueous suspension of polystyrene particles " Opt. Spectrosc. **98**, 466 (2005).

11. P. J. Reece, E. M. Wright, and K. Dholakia, "Experimental observation of modulation instability and optical spatial soliton arrays in soft condensed matter " Physical Review Letters **98**, 203902 (2007).

12. J. Junio, E. Blanton, and H. D. Ou-Yang, "The Kerr effect produced by optical trapping of nanoparticles in aqueous suspension," Optical Trapping and Optical Micromanipulation IV. Edited by Dholakia, Kishan; Spalding, Gabriel C. Proceedings of the SPIE, Volume 6644, pp. 664408 (2007).

13. C. Conti, G. Ruocco, and S. Trillo, "Optical spatial solitons in soft matter," Phys. Rev. Lett. 95, 183902 (2005).

14. R. El-Ganainy, D. N. Christodoulides, C. Rotschild, and M. Segev, "Soliton dynamics and self-induced transparency in nonlinear nanosuspensions," Optics Express 15, 10207 (2007).

15. R. Gordon, J. T. Blakely, and D. Sinton, "Particle-optical self-trapping," Phys. Rev. A 75, 055801 (2007).

16. D. Rogovin and S.O. Sari, "Phase conjugation in liquid suspenstions of microspheres in the diffusive limit," Phys. Rev. A **31**, 2375-2389 (1985).

17. R. El-Ganainy, D. N. Christodoulides, Z. H. Musslimani, C. Rotschild, and M. Segev, "Optical beam instabilities in nonlinear nanosuspensions," Opt. Lett. 32, 3185 (2007).

18. J. E. Mayer and M. G. Mayer, *Statistical Mechanics* (John Wiley and Sons, Inc., New York, 1966).

19. B.J. Berne and R. Pecora, *Dynamic Light Scattering: With Applications to Chemistry, Biology and Physics* (Dover Publication, Inc. New York 2000)

20. J.D. Jackson, *Classical Electrodynamics*, (John Wiley and Sons, New York 1999).

21. J.M.C. Garnett, "Colors in Metal Glasses and in Metallic Films," Philos. Trans. R. Soc. London 203, 385-420 (1904).

22. J.M.C. Garnett, "Colors in Metal Glasses, in Metallic Films and in Metallic solutions," Philos. Trans. R. Soc. London 205, 237- 288 (1906).

23. H.C. van de Hulst, *Light Scattering by Small Particles*, (Dover Publication, Inc. New York 1981).

24. N.G. Vakhitov and A.A. Kolokolov, "Stationary solutions of the wave equation in a medium with nonlinearity saturation," Izv. Vyssh. Uchebn. Zaved Radiofiz. 16 1020 (1973) [Radiophys. Quantum Electron. 16, 783 (1973)].

25. L. Berge, "Wave collapse in physics: principles and applications to light and plasma waves," Phys. Rep. 303, 259 (1998).

26. M. Segev, G.C. Valley, B. Chosignani, P.D Portp and A. Yariv, "steady state spatial screening solitons in photorefractive material with external applied field," Phys. Rev. Lett. **73**, 3211 (1994).

27. D.N. Christodoulides and M.I. Carvalho, "Bright, dark and gray spatial soltion states in photorefractive media," J. Opt. Soc. Am B **12**, 1628 (1995).

28. P.K. Kaw, K. Nishikawa, Y. Yoshida and A. Hasagawa, "Two-Dimetional and Three-Dimentional Envelope Solitons," Phys. Rev. Lett. **35** 88-91 (1975).

29. J.Z. Wilcox and T.J. Wilcox, "Stability of Localized Plasma in Two and Three Dimentions," Phys. Rev. Lett. **34**, 1160-1163 (1975)

30. K. Tai, H. Hasegawa and A. Tomita, "Observation of modulational instability in optical fiber," Phys. Rev. Lett. **65**, 135 (1986).

31. D. Kip, M. Soljacic, M. Segev, E. Eugenieva, and D. N. Christodoulides, "Modulation instability and pattern formation in spatially incoherent light beams", Science **290**, 495 (2000).

32. E. A. Kuznetsov, A. M. Rubenchik, and V. E. Zakharov, "Soliton stability in plasmas and hydrodynamics", Phys. Rep. **142**, 103 (1986).

33. W.B. Russel, D.A. Savillie, and W.R. Schrowalter, *Colloidal Dispersions* (Cambridge University press1989).

34. J.H. Masliyah and S.Bhattacharjee, *Electrokinetic and Colloid Transport Phenomena*, (John Wiley and Sons 2006).

35. J.C. Crocker and D.G. Grier, "Microscopic measurement of the pair interaction potential of charge-stabilized colloid" Phys. Rev. Lett. **73**, 352 (1994).

36. R. El-Ganainy, D. N. Christodoulides, E. M. Wright, W. M. Lee and K. Dholakia, "Nonlinear optical dynamics in non-ideal "gases" of interacting colloidal nano-particles" submitted to Phys. Rev. A.

37. M. Matuszewski, W. Krollkowski, and Y. S. Kivshar, "Spatial solitons and light-induced instabilities in colloidal media," Optics Express 16, 1371 (2008).

38. M. Matuszewski, W. Krollkowski, and Y. S. Kivshar, "Soliton interactions and transformations in colloidal media," Phys. Rev. A 79, 023814 (2009).

39. W.M. Lee, R. El-Ganainy, D.N. Christodoulides, K. Dholakia and E.M. Wright, "Nonlinear optical response of colloidal suspensions", Optics Express 17, 10277 (2009).

40. Critical collapse beyond a self-focusing power occurs for the case sd=4, where s is the order of the nonlinearity, s=2 for a Kerr medium, and d the number of transverse dimensions. Super-critical collapse occurs for sd>4 and tends to be much more abrupt spatially than critical collapse, see, for example, N. E. Kosmatov, V. F. Shvets, and V. E. Zakharov, "Computer simulation of wave collapses in the nonlinear Schrodinger equation," Physica D 52, 16-35 (1991).

41. M. Sheik-Bahae, A. A. Said, and E. W. Van Stryland, "High-sensitivity, single-beam n_2 measurements," Opt. Lett. 14, 955-957 (1989).

42. P. M. Hansen, V. K. Bhatia, N. Harrit, and L. Oddershede, "Expanding the optical trapping range of gold nanoparticles," Nano Lett. 5, 1937-1942 (2005).

43. D. Anderson and M. Bonnedal, Phys. Fluids 22, 105 (1995).

44. E. M. Wright, B. L. Lawrence, W. Torruellas, and G. I. Stegeman, "Stable self-trapping and ring formation in PTS," Opt. Lett. 20,2481-2483 (1995).

45. H. Goldstein, *Classical Mechanics*, (Addison-Wesley 1965).

46. S.H. Strogatz, *Nonlinear Dynamics And Chaos: With Applications to Physics, Biology, Chemistry, And Engineering*, (Wesrview Press 2001).

47. P.G. Drazin and R.S. Johnson, *Solitons: an introduction*, (Cambridge university press 1989).

48. R.L. Liboff, *Introductory Quantum Mechanics*, (Addison-Wesley 1992).

49. C. Sulem and P.L. Sulem, *The Nonlinear Schrödinger Equation: Self-Focusing and Wave Collapse* (Springer 1989).

50. S. Trillo and W. Torruellas, *Spatial Solitons*, (Springer 2001)

51. C.J. Pethick and H. Smith, Bose-Einstein Condensate in Dilute Gases, (Cambridge university press 2008).

52. P. N. Prasad, *Nanophotonics*, (John Wiley and Sons, New York 2004).

53. S. G. Leon-Saval, T. A. Birks, W. J. Wadsworth, P. St. J. Russell, and M. W. Mason, "Supercontinuum generation in submicron fibre waveguides," Opt. Express **12,** 2864-2869 (2004).

54. L. Tong, R. R. Gattass, J. B. Ashcom, S. He, J. Lou, M. Shen, I. Maxwell, and E. Mazur, " Subwavelength-diameter silica wires for low-loss optical wave guiding", Nature **426**, 816-819, (2003).

55. J.C.Knight, J. Arriaga, T.A Briks, A. Ortigosa-Blanch, W.J. Wadsworth and P. St. J. Russell, " Anomalous Dispersion in Photonic Crystal Fiber", IEEE Photonics Technology Letters **12**, 807-809, (2000).

56. M. A. Foster, A. L. Gaeta, Q. Cao, and R. Trebino, "Soliton-effect compression of supercontinuum to few-cycle durations in photonic nanowires," Opt. Express **13,** 6848-6855 (2005).

57. G. Brambilla, F. Koizumi, V. Finazzi, and D. J. Richardson, "Supercontinuum generation in tapered bismuth silicate fibres", Electron. Lett. **41,** 795-797 (2005).

58. H. Ebendorff-Heidepriem, P. Petropoulos, S. Asimakis, V. Finazzi, R. C. Moore, K. Frampton, F. Koizumi, D. J. Richardson, and T. M. Monro, "Bismuth glass holey fibers with high nonlinearity", Opt. Express **12,** 5082-5087 (2004).

59. G. Brambilla, F. Koizumi, X. Feng, and D. J. Richardson, "Compound-glass optical nanowires", Electron. Lett. **41,** 400-402 (2005).

60. H. Fukuda, K. Yamada, T. Shoji, M. Takahashi, T. Tsuchizawa, T. Watanabe, J. Takahashi and S. Itabashi, "Four-wave mixing in silicon wire waveguide", Opt. Express, 13, 4629-4635, (2005).

61. Y. K. Lizé, E. C. Mägi, V. G. Ta'eed, J. A. Bolger, P. Steinvurzel, and B. J. Eggleton, "Microstructured optical fiber photonic wires with subwavelength core diameter", Opt. Express **12,** 3209-3217 (2004).

62. V. Kumar, A. George, J. C. Knight, and P. St. J. Russell, "Tellurite photonic crystal fiber", Opt. Express **11**, 2641-2645 (2003).

63. J. C. Knight, "Photonic Crystal fibers", Nature **424**, 847-851 (2003).

64. G.I. Stegeman, A. Villeneuve, J. Kang, J.S. Aitchison, C.N. Ironside, K. Al-hemyari, C.C. Yang, C-H. Lin, H-H. Lin, G.T. Kennedy, R.S. Grant and W. Sibbett, "AlGaAs Below Half Bandgap: The Silicon of Nonlinear Optical Materials", Int. J. of Nonlinear Optical Physics, **3**, 347-371 (1994).

65. J. E. Heebner, N. N. Lepeshkin, A. Schweinsberg, G. W. Wicks, R. W. Boyd, R. Grover and P.-T. Ho, "Enhanced linear and nonlinear optical phase response of AlGaAs microring resonators", Opt. Lett. **29**, 769-771, (2004).

66. R. Iwanow, G. I. Stegeman, D. N. Christodoulides, R. Morandotti, D. Modotto, A. Locatelli, C. De Angelis, F. Pozzi, C. R. Stanley, and M. Sorel, "Enhanced Third-Order Nonlinear Effects in Optical AlGaAs Nanowires", post-deadline paper PDP7, Nonlinear Guided Waves and Their Applications, OSA Topical Meeting, Dresden, Germany, Sep. 6-9, 2005.

67. U. Peschel , T. Peschel, and F. Lederer, "A compact device for highly efficient dispersion compensation in fiber transmission", Appl. Phys. Lett. **67** , 2111-2113 (1995).

68. C.J. Hamilton, B. Vogele, J.S. Aitchison, G.T. Kennedy, W. Sibbett, W. Biehlig, U. Peschel, T. Peschel, F. Lederer, "Bright Solitary pulses in AlGaAs waveguides at half the band gap", Opt. Lett. **21**, 1226-1228, (1996).

69. S.Gehrsitz, F.K. Reinhart, C. Gourgon, A. Vonlanthen and H. Sigg, "The refractive index of $Al_xGa_{1-x}As$ below the band gap: Accurate determination and empirical modeling" J. Appl. Phys, **87**,7825-7837 (2000).

70. J. U. Kang, A. Villeneuve, M. Sheik-Bahae, George I. Stegeman, K. Al-hemyari, J. S. Aitchison, C. N. Ironside, " Limitation due to three-photon absorption on the useful spectral range for nonlinear optics in AlGaAs below half band gap", Appl. Phys. Lett. **65**, 147-149 (1994).

71. K. Okamoto, *Fundamental of Optical Waveguides*, (Academic Press, San Diego 2000).

72. L. Tong, J. Lou, and E. Mazur, "Single-mode guiding properties of subwavelength-diameter silica and silicon waveguides", Opt. Express **12**,1025-1035 (2004).

73. A.L. Gaeta, "Nonlinear propagation and continuum generation in microstructured optical fibers"Opt. Lett. **27**, 924-926 (2002).

74. S. Kawata, M. Ohtsu and M. Irie, *Nano-Optics*, (Springer Verlag , Berlin 2002).

75. L. Scaccabarozzi, X. Yu, M. L. Povinelli, S. Fan, M. M. Fejer and J. S. Harris, "Highly Efficient Birefringent Second Harmonic Generation in Submicron AlGaAs/Al$_x$O$_y$ Waveguides," CLEO 2005 Techncial Digest, paper CPDA10.

76. R. El-Ganainy, S. Mokhov, K.G. Makris and D. N. Christodoulides, "Solitons in dispersion-inverted *AlGaAs* nanowires," Opt. Express **14,** 2277-2282 (2006).

77. D. Hondros and P. Debye, "Elektromagnetische Wellen an dielektrischen Drähten," Ann. Physik **32**, 465 -476, (1910).

78. S. A. Schelkunoff, *Electromagnetic Waves* (D. Van Nostrand Inc., New York, 1943).

79. E. Snitzer, "Cylindrical Dielectric Waveguide Mode," J. Opt. Soc. Am. **51**, 491-498 (1961).

80. E. F. F. Gillespie, Proc. Inst. Elect. Eng. **107**c, 198-201 (1960).

81. J. D. Jackson, *Classical Electrodynamics* (Wiley, New York, 1975).

82. Y. N. Noskov, "Method for measuring properties of high relative dielectric constant materials in a cutoff waveguide cavity," IEEE Trans. Microwave Theory Tech, **MTT-48**, 329-333, (2000).

83. Ilya V. Shadrivov, Andrey A. Sukhorukov, and Yuri S. Kivshar, "Guided modes in negative-refractive-index waveguides," Physical Review E, **67** , 0576021-0576024 (2003)

84. S. Kawata and T. Tani, "Optically driven Mie particles in an evanescent field along a channeled waveguide," Opt. Lett. **21**, 1768-1770, (1996).

85. A. Ashkin, "Acceleration and trapping of particles by radiation pressure," Phys. Rev. Lett. **24**, 156-159, (1970).

86. C.M. Bender and S. Boettcher," Real Spectra in Non-Hermitian Hamiltonians Having *PT* Symmetry," Phys. Rev. Lett., **80**, 5243-5246 (1998).

87. C.M. Bender, S. Boettcher and P.N. Meisinger,"*PT*-symmetric Quantum Mechanics," J. Math. Phys. **40**, 2201-2229 (1999).

88. C.M. Bender, D.C. Brody, and H.F. Jones, "Complex Extension of Quantum Mechanics," Phys. Rev. Lett., **89**, 270401 (2002).

89. A. Mostafazadeh, "Exact *PT*-symmetry is equivalent to Hermiticity," J. Phys. A: Math. Gen. **36**, 7081-7091 (2003).

90. A. Siegman, "Propagating modes in gain-guided optical fibers**,"** J. Opt. Soc. Am. A. **20**, 1617 (2003).

91. A. Yariv, **"**Coupled-mode theory for guided-wave optics," IEEE J Quantum Electron. **9**, 919-933 (1973).

92. D. N. Christodoulides, F. Lederer and Y. Silberberg, "Discretizing light behaviour in linear and nonlinear waveguide lattices," Nature, **14**, 817-823 (2003).

93. T. Tamir, *Guided-Wave Optoelectronics* (Springer-Verlag 1990).

94. S. Katsura, "Fourth Virial Coefficient for the Square Well Potential" Phys. Rev. **115**, 1417 (1959).